Electronic Supplementary Material (ESI) for Physical Chemistry Chemical Physics.

Supporting Information:

Full elucidation of the transmembrane anion transport mechanism of squaramides using *in silico* investigations

Igor Marques,[a] Pedro M. R. Costa,[a] Margarida Q. Miranda,[a] Nathalie Busschaert,[b,c] Ethan N. W. Howe,[b,d] Harriet J. Clarke,[b] Cally J. E. Haynes,[b,e] Isabelle L. Kirby,[b] Ananda M. Rodilla,[f] Ricardo Pérez-Tomás,[f] Philip A. Gale,*[b,d] and Vítor Félix*[a]

Author affiliations:

[a] Department of Chemistry, CICECO – Aveiro Institute of Materials, University of Aveiro, 3810-193, Aveiro, Portugal.
[b] Chemistry, University of Southampton, Southampton, SO17 1BJ, UK.
[c] Current address: Department of Chemistry, Tulane University, New Orleans, Louisiana 70118, United States.
[d] School of Chemistry, University of Sydney, NSW 2006, Australia
[e] Current Address: Department of Chemistry, University of Cambridge, Lensfield Road, Cambridge, CB2 1EW, UK.
[f] University of Barcelona, Faculty of Medicine, Dept. Pathology and Experimental Therapeutics, CCBRG, Barcelona, Spain.

TABLE OF CONTENTS

S1. OVERVIEW OF COMPOUNDS

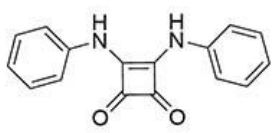

A1

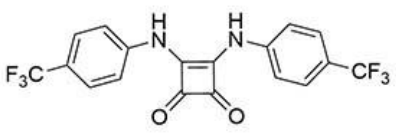

A2

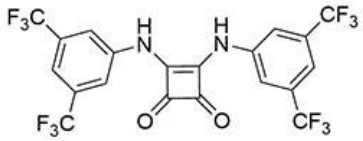

A3

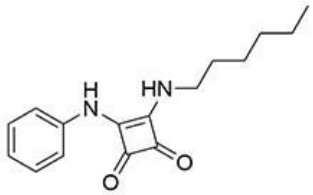

B1

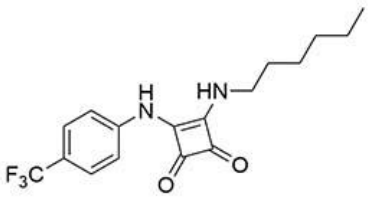

B2

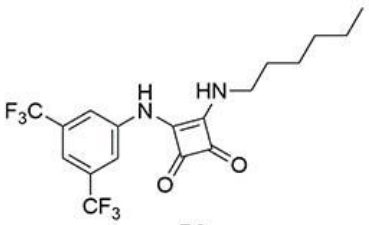

B3

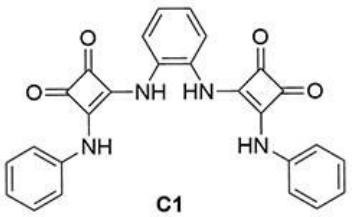

C1

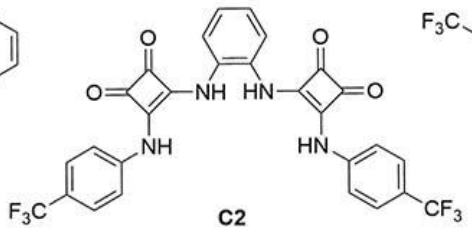

C2

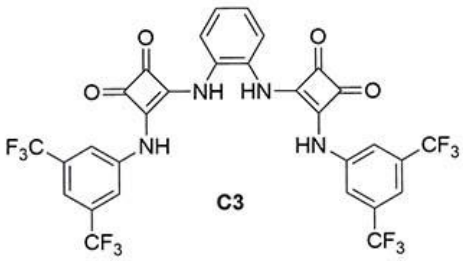

C3

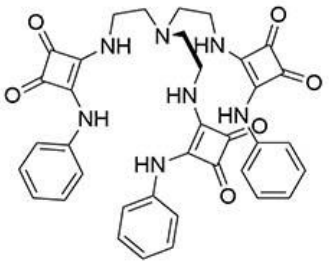

D1

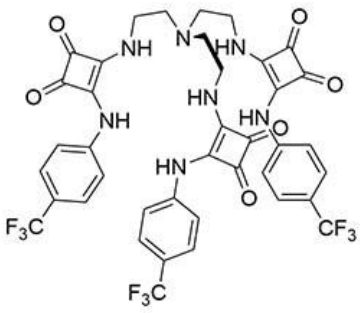

D2

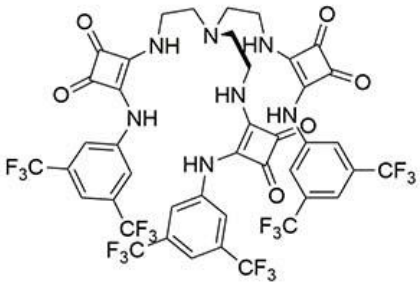

D3

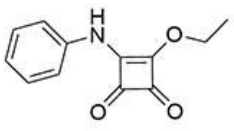

E1

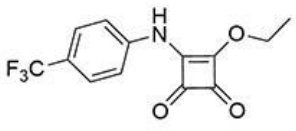

E2

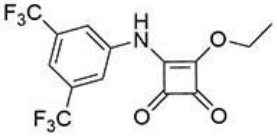

E3

S2. SYNTHESIS & CHARACTERISATION

S2.1. General

^{1}H NMR (300 MHz), ^{19}F NMR (282 MHz) and ^{13}C NMR (75 MHz) spectra were determined on a Bruker AV300 spectrometer. ^{1}H NMR (400 MHz), ^{19}F NMR (376 MHz) and ^{13}C NMR (100 MHz) spectra were determined on a Bruker DPX400 spectrometer. ^{13}C NMR spectra were always collected proton decoupled. Chemical shifts (δ) are reported in parts per million (ppm) and calibrated to the residual protio solvent peak in DMSO-d_6 (δ = 2.50 (^{1}H) and 74.2 ppm (^{13}C)). The following abbreviations are used for spin multiplicity: s = singlet, d = doublet, t = triplet, q = quartet, quin = quintet, m = multiplet, br = broad. Low resolution mass spectra (LRMS) were recorded on a Walters ZMD single quadrupole spectrometer. High resolution electron spray ionisation (ESI) mass spectra were recorded on a Bruker maXis ESI. All mass spectra are reported as *m/z*. Infrared (IR) spectra were recorded on a Matterson Satellite (ATR) and are reported in wavenumbers (cm^{-1}); only a selected number of the most pronounced peaks are reported. Melting points were determined using open capillary tubes on a Barnstead Electrothermal 9100 or Gallenkamp melting point apparatus and were not corrected. Fluorescence spectra were recorded on a Cary Eclipse fluorescence spectrophotometer. Solvents and reagents were used as provided by the supplier unless otherwise stated. Many of the compounds have been reported elsewhere and their synthesis and characterisation will not be discussed here: **A1**-**A2**-**A3**,[1] **B2**,[2] **C2**-**C3**,[2] **D1**-**D2**,[3, 4] **D3**,[2] **E1**,[5] **E2**-**E3.**[2] Only the synthesis of novel compounds **B1**, **B3** and **C1** will be discussed here.

S2.2. Synthetic procedures

3-(hexylamino)-4-(phenylamino)cyclobut-3-ene-1,2-dione (B1).

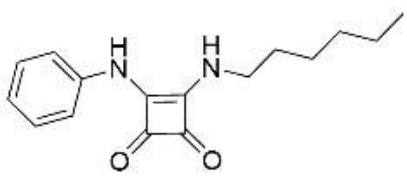

Compound **E1** (200 mg, 0.921 mmol, 1 eq) and zinc triflate (33 mg, 0.091 mmol, 0.1 eq) were dissolved in DMF (200 µL) and toluene (1 mL) at 50° C. Hexylamine (180 µL, 1.362 mmol, 1.5 eq) was added dropwise and the resulting mixture was heated up and refluxed for 4 hours at 80° C under nitrogen atmosphere. The resulting precipitate was filtered off and washed with methanol. After filtration, the precipitate was resuspended in methanol and refluxed for 2 hours. The suspension was then filtered, and washed with methanol. Compound **B1** was obtained as a white solid after drying under high vacuum for 24 hours (0.221 g, 0.811 mmol).

Yield: 88%; Mp: 254-256° C; ^{1}H NMR (400 MHz, DMSO-d_6) δ ppm 9.60 (br. s., 1 H), 7.64 (br. s., 1 H), 7.43 (d, *J* = 7.9 Hz, 2 H), 7.33 (t, *J* = 7.9 Hz, 2 H), 7.02 (t, *J* = 7.3 Hz, 1 H), 3.59 (t, *J* = 6.2 Hz,

2 H), 1.56 (quin, *J* = 6.9 Hz, 2 H), 1.29 (m, 6 H), 0.86 (t, *J* = 6.4 Hz, 3 H); ^{13}C NMR (101 MHz, DMSO-d_6) δ ppm 184.0, 180.1, 169.3, 163.5, 139.1, 129.3, 122.6, 118.0, 43.7, 30.8, 30.6, 25.5, 22.0, 13.9; IR (solid): ν= 3180, 2960, 2930, 1790, 1660, 1550, 1450, 750, 685, 503 cm^{-1}; LRMS (ESI-): *m/z*= 271.2 [M-H]$^-$; HRMS (ES) for $C_{16}H_{21}N_2O_2$ [M+H]$^+$: *m/z*= 273.1598 (calcd), 273.1590 (found), for $C_{16}H_{20}N_2O_2Na$ [M+Na]$^+$: *m/z*= 295.31417 (calcd), 295.1409 (found).

3-((3,5-bis(trifluoromethyl)phenyl)amino)-4-(hexylamino)cyclobut-3-ene-1,2-dione (B3).

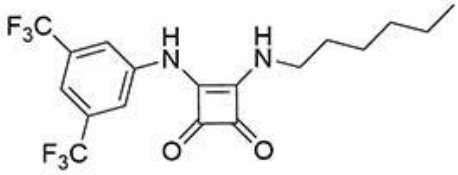

Compound **E3** (300 mg, 0.849 mmol, 1 eq) and zinc triflate (30 mg, 0.082 mmol, 0.1 eq) were dissolved in DMF (200 µL) and toluene (1 mL) at 50° C. Hexylamine (120 µL, 0.908 mmol, 1.1 eq) was added dropwise and the resulting mixture was heated up and refluxed overnight at 80° C under nitrogen atmosphere. Methanol was added to the resulting sticky solid and the mixture was sonicated for 1 hour. The suspension was then filtered and washed with methanol. Compound **B3** was obtained as a pale-yellow solid after drying under high vacuum for 24 hours (0.205 g, 0.502 mmol).

Yield: 59%; Mp: 218-222° C; ^{1}H NMR (400 MHz, DMSO-d_6) δ ppm 10.15 (br. s., 1 H), 8.02 (s, 2 H), 7.75 (br. s., 1 H), 7.63 (s, 1 H), 3.60 (br. t., 2 H), 1.56 (quin, *J* = 6.9 Hz, 2 H), 1.29 (m, 6 H), 0.86 (t, *J* = 6.3 Hz, 3 H); ^{13}C NMR (101 MHz, DMSO-d_6) δ ppm 184.8, 180.4, 169.8, 162.3, 141.2, 131.3 (q, J_{C-F} = 32.3 Hz), 123.2 (q, J_{C-F} = 272.2 Hz), 118.0, 114.6, 43.9, 30.8, 30.5, 25.5, 22.0, 13.9; ^{19}F NMR (376 MHz, DMSO-d_6) δ ppm -62.26 (s, 3 F); IR (solid): ν= 3190, 3090, 2940, 1790, 1660, 1570, 1450, 1380, 1270, 1130, 883, 733, 681 cm^{-1}; LRMS (ESI-): *m/z*= 407.0 [M-H]$^-$; HRMS (ES) for $C_{18}H_{19}F_6N_2O_2$ [M+H]$^+$: *m/z*= 409.1345 (calcd), 409.1354 (found).

4,4'-(1,2-phenylenebis(azanediyl))bis(3-(phenylamino)cyclobut-3-ene-1,2-dione) (C1).

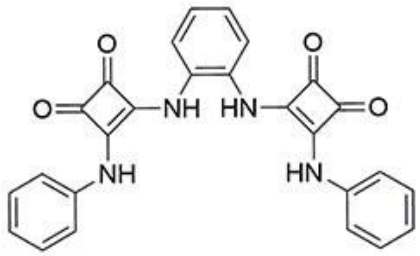

o-Phenylenediamine was recrystallised from DCM-hexane prior to use. *o*-Phenylenediamine (100 mg, 0.925 mmol, 1.0 eq) was suspended in di-isopropylethylamine (1.0 mL) and DMF (0.2 mL) and stirred for 15 minutes at room temperature. This suspension was subsequently added dropwise to a solution of compound **E1** (440 mg, 2.026 mmol, 2.2 eq) and zinc triflate (74 mg, 0.204 mmol, 0.2 eq) in toluene (0.9 mL) and dry DMF (0.1 mL) at 50° C. The resulting mixture was heated up and refluxed overnight at 80° C under nitrogen atmosphere. The resulting precipitate was filtered off and washed with methanol. The filtrate was concentrated until most of the DMF was removed and a second precipitate was obtained after the addition of methanol followed by sonication. The combined solids were subsequently redissolved in DMSO and water was added dropwise until no more precipitation occurred. After

filtration and washing with methanol and diethyl ether, the precipitate was suspended in methanol and refluxed for 18 hours. After filtration and washing with methanol, compound **C1** was obtained as a yellow solid (0.238 g, 0.528 mmol).

Yield: 57%; Mp: decomposition; ^{1}H NMR (300 MHz, DMSO-d_6) δ ppm 9.98 (br. s., 2 H), 9.71 (br. s., 2 H), 7.48 (d, J = 7.5 Hz, 4 H), 7.37 (m, looks like t with J = 7.9 Hz, 6 H), 7.20 (br. s., 2 H), 7.08 (t, J = 7.5 Hz, 2 H); ^{13}C NMR (101 MHz, DMSO-d_6) δ ppm 182.4, 182.0, 166.3, 166.1, 138.5, 129.4, 125.1, 123.3, 118.5 (presumably overlapping ^{13}C signals are present); IR (solid): ν= 3310, 3270, 3220, 3170, 3120, 3040, 2970, 1790, 1680, 1580, 1540, 1480, 1420, 748, 656, 501, 467 cm^{-1}; LRMS (ESI-): *m/z*= 449.2 [M-H]$^{-}$; HRMS (ES) for $C_{26}H_{18}N_4O_4Na$ [M+Na]$^{+}$: *m/z*= 473.1220 (calcd), 473.1220 (found). The structure of compound **C1** was confirmed by X-ray crystallography (see section S2.4.).

S2.3. NMR spectra

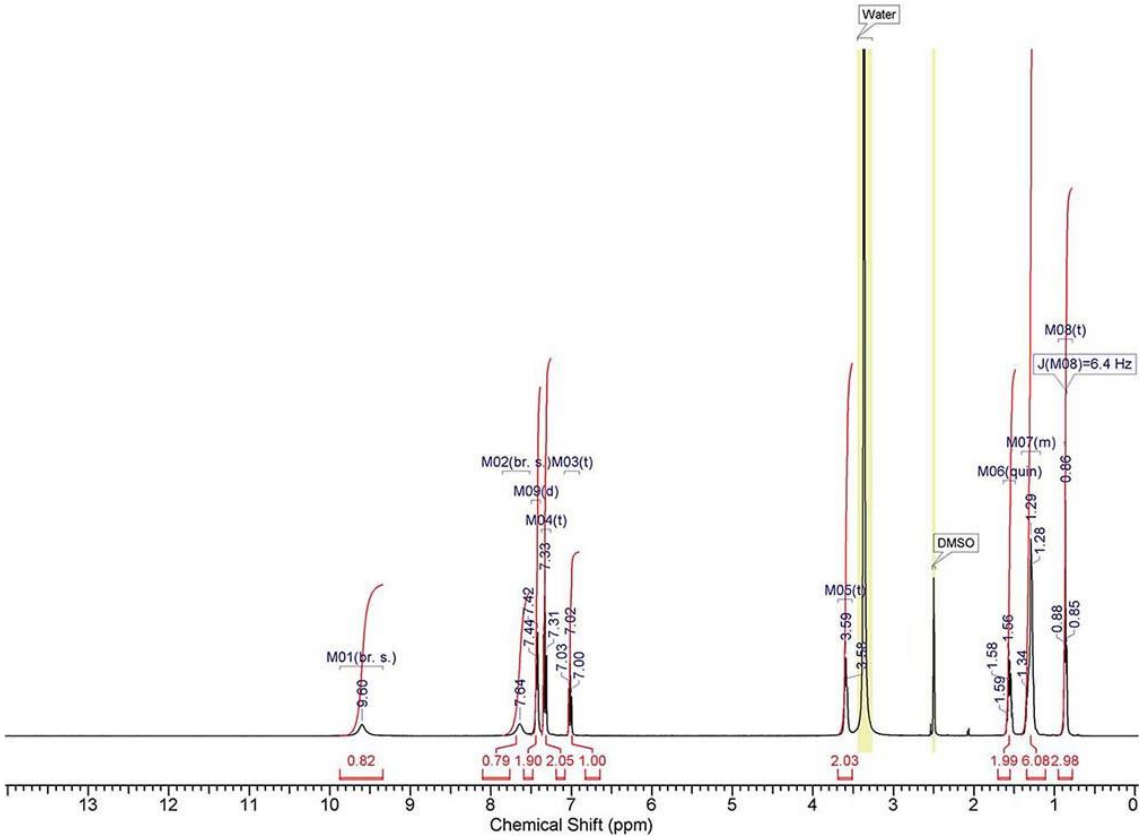

Figure S1. ^{1}H NMR spectrum (400 MHz) of compound **B1** in DMSO-d_6 at 298K.

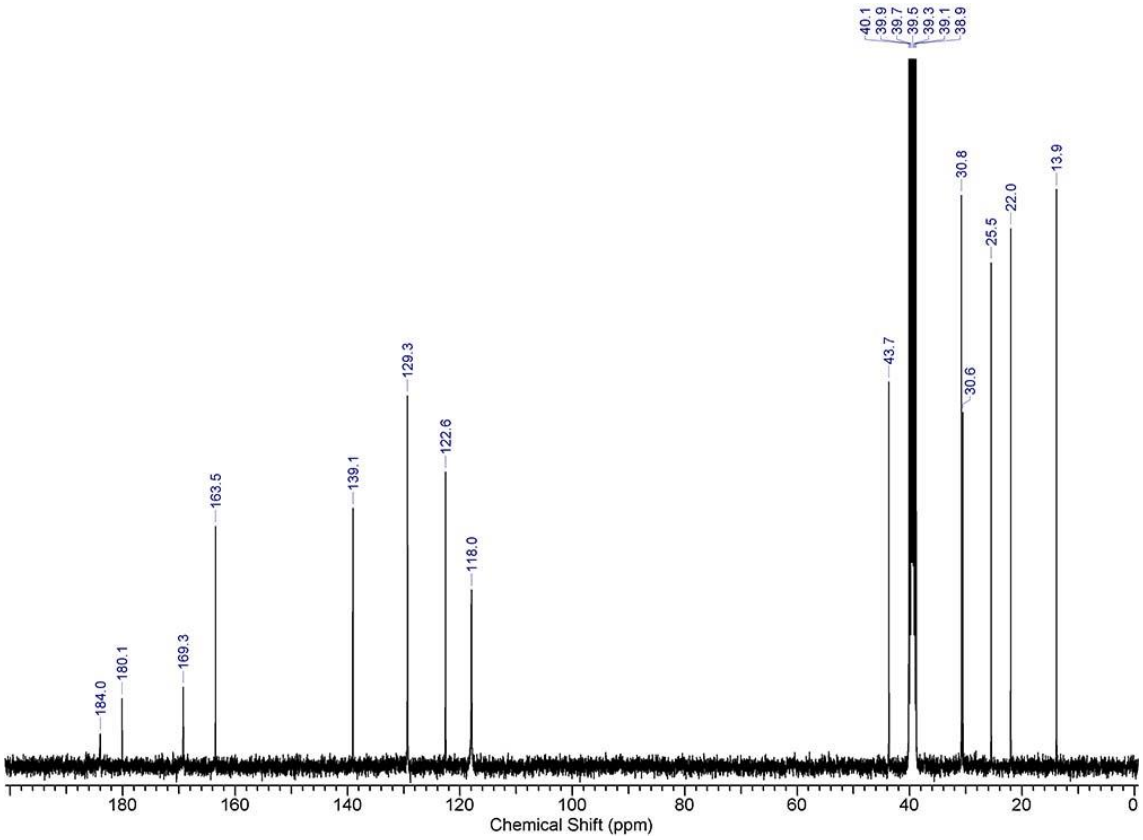

Figure S2. ^{13}C NMR (101 MHz) spectrum of compound **B1** in DMSO-d_6 at 298K.

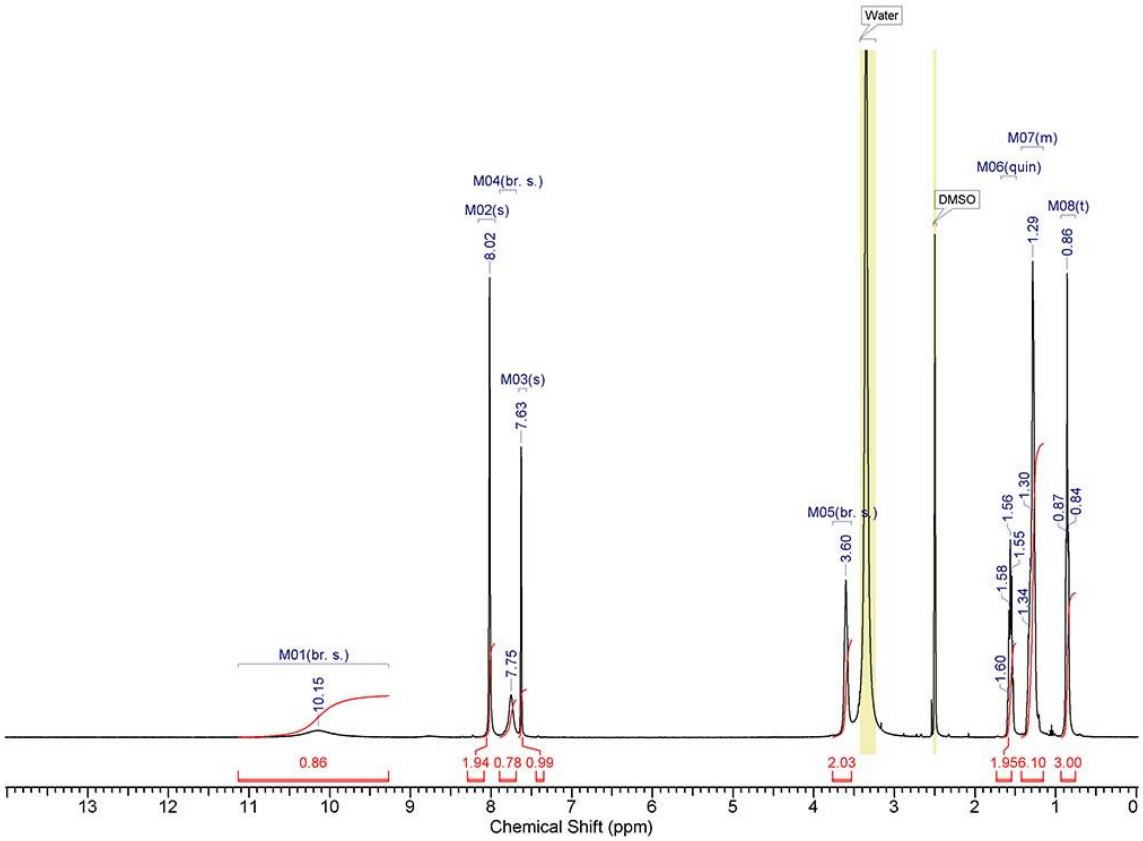

Figure S3. ^{1}H NMR spectrum (400 MHz) of compound **B3** in DMSO-d_6 at 298K.

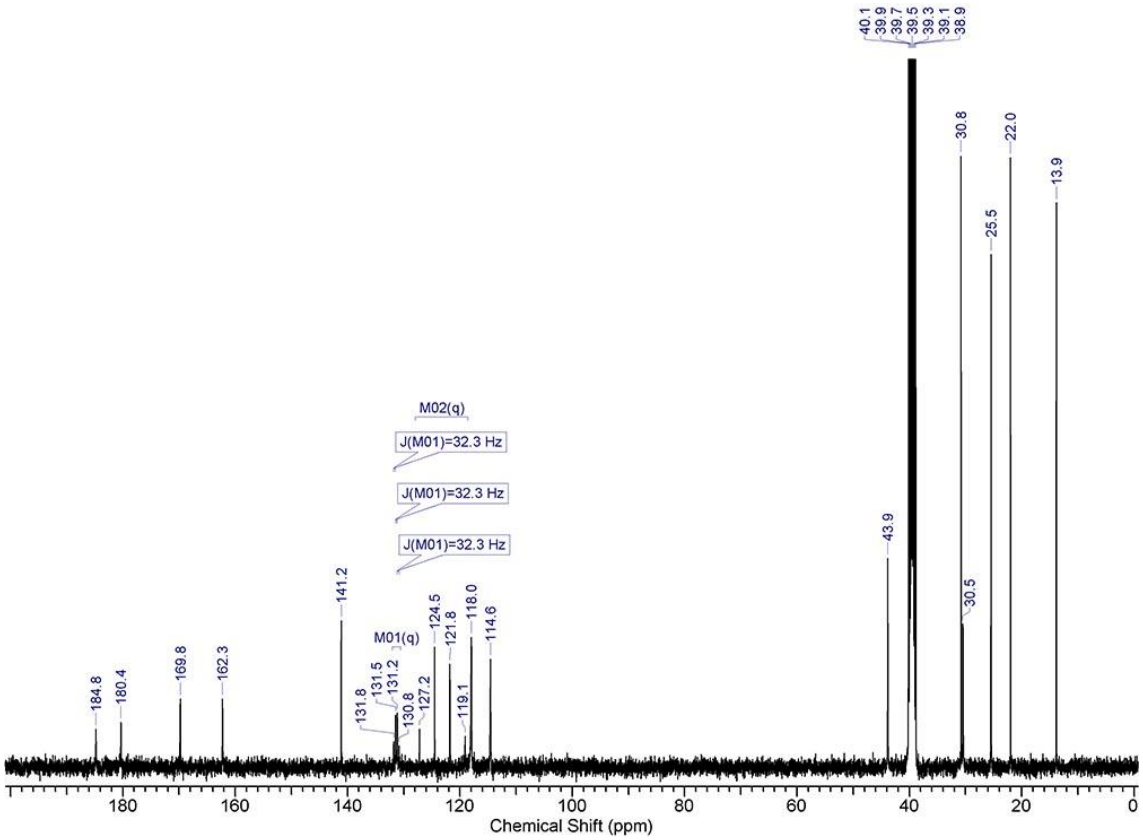

Figure S4. ^{13}C NMR (101 MHz) spectrum of compound **B3** in DMSO-d_6 at 298K.

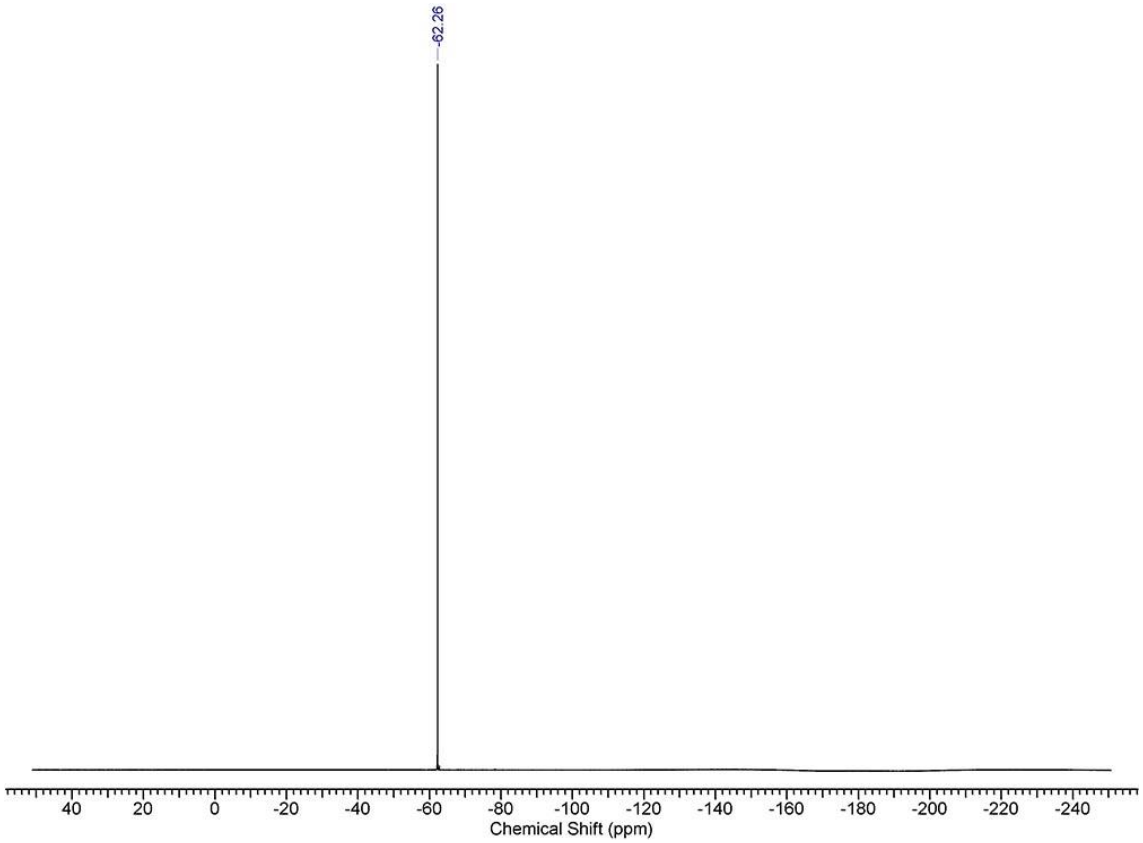

Figure S5. ^{19}F NMR (376 MHz) spectrum of compound **B3** in DMSO-d_6 at 298K.

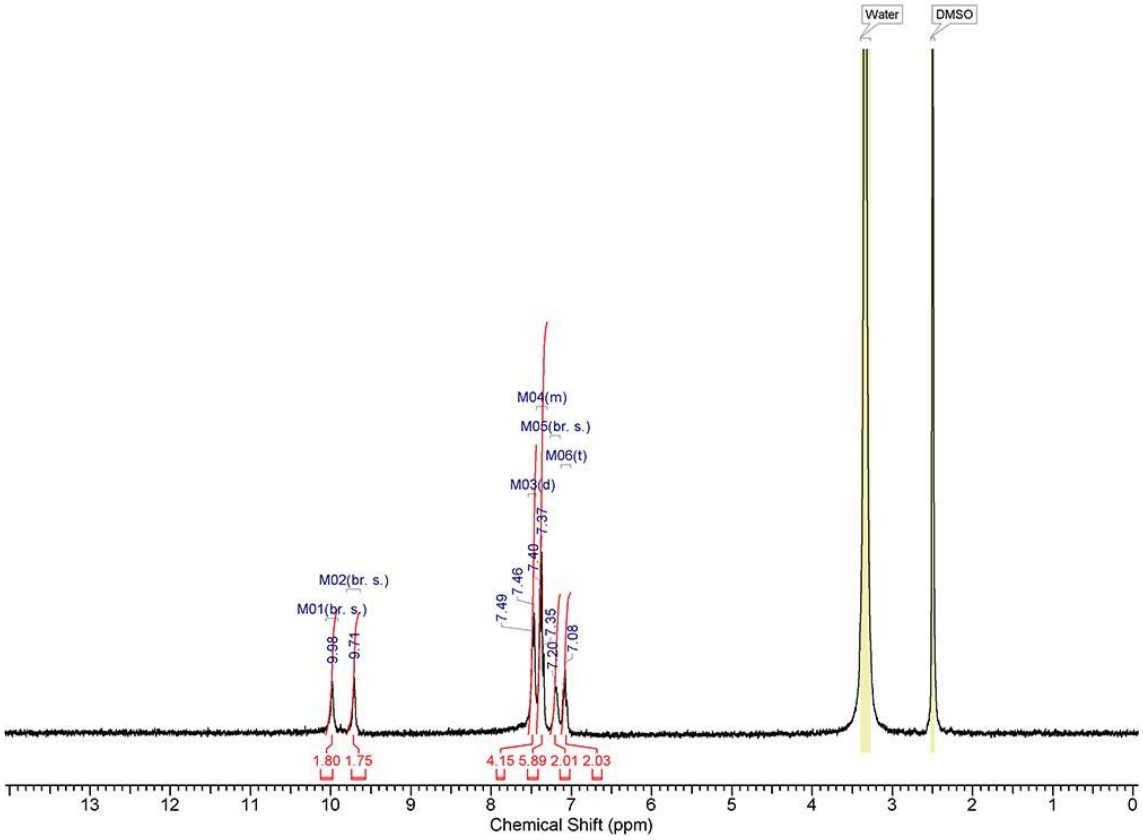

Figure S6. [1]H NMR (300 MHz) spectrum of compound **C1** in DMSO-d_6 at 298K.

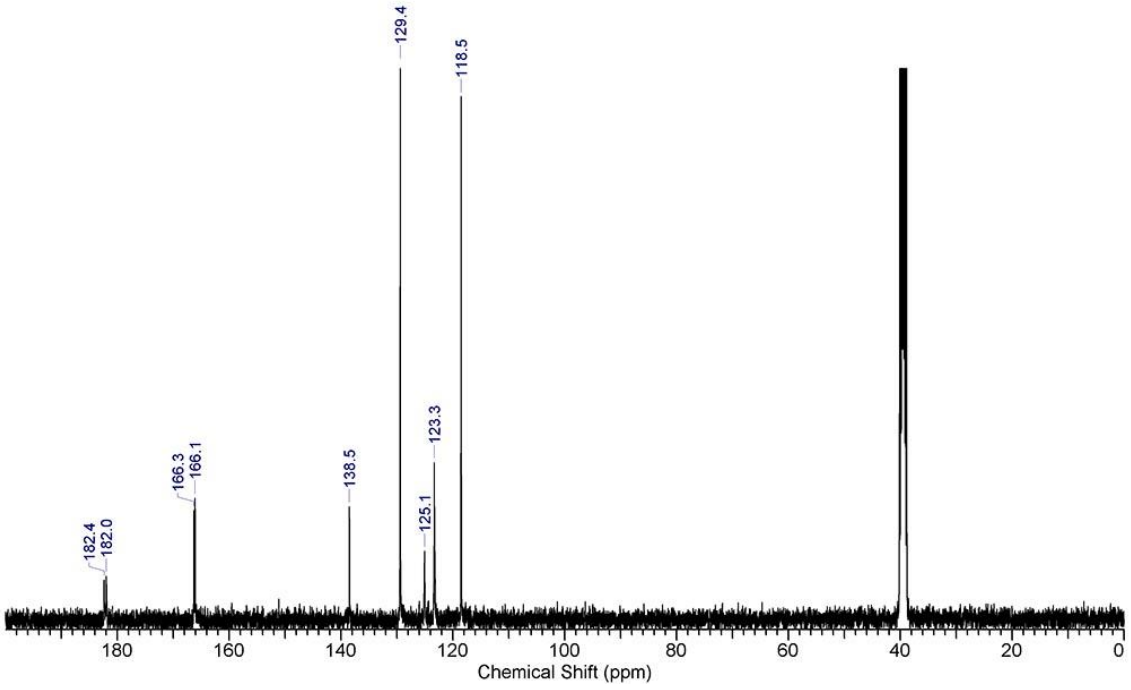

Figure S7. [13]C NMR (101 MHz) spectrum of compound **C1** in DMSO-d_6 at 298K.

S2.4. Single crystal X-ray diffraction

DMSO solvate of **C1**

Single crystals suitable for X-ray diffraction were obtained from the slow evaporation at 50° C of a DMSO solution of **C1**. The crystals were run at the University of Southampton on a *Rigaku AFC12* goniometer equipped with an enhanced sensitivity (HG) *Saturn724+* detector mounted at the window of an *FR-E+ SuperBright* molybdenum rotating anode generator with VHF *Varimax* optics (70µm focus). The crystal was kept at T = 100(2) K during data collection with an Oxford Cryosystems low-temperature apparatus. Cell determination, data collection, data reduction and cell refinement & absorption correction were preformed using *CrystalClear-SM Expert 2.0 r7* (Rigaku, 2011). The structure was solved using SHELXS-97 and refined using SHELXL-2014/7.[6] Graphics were generated using MERCURY 3.0 or ViewerLite and Pov-Ray. The non-hydrogen atoms were refined anisotropically till convergence. Hydrogen atoms were stereochemically fixed at idealised positions and then refined isotropically. Hydrogen bonds are calculated using HTAB command in SHELXL-97. The structure was deposited with the Cambridge Crystallographic Database Centre (CCDC) and assigned the number CCDC 1590597.

Crystal data for **C1·(DMSO)$_2$**: $C_{30}H_{30}N_4O_6S_2$, M_r = 606.70 g/mol, crystal size = 0.03 x 0.03 x 0.02 mm^3, colourless needle, triclinic, space group $P\bar{1}$, a = 9.638(7) Å, b = 10.144(8) Å, c = 15.997(11) Å, α = 102.159(13)°, β = 95.626(10)°, γ = 101.283(7)°, V = 1483.5(19) Å^3, Z = 2, ρ_c = 1.358 g cm^{-3}, μ = 0.229 mm^{-1}, radiation and wavelength = MoKα (0.71075), T = 100(2) K, θ_{max} = 27.48, reflections collected: 12889, independent reflections: 6727 (R_{int} = 0.0952), 379 parameters, R indices (all data): R_1 = 0.1013, wR_2 = 0.1685, final R indices [$I > 2\sigma I$]: R_1 = 0.0640, wR_2 = 0.1591, $GOOF$ = 0.950, largest diff. peak and hole = 0.315 and -0.408 e Å^3.

Table S1. Hydrogen bond properties for **C1·(DMSO)$_2$.**

Donor--H···Acceptor	D-H (Å)	H···A (Å)	D···A (Å)	D-H···A (°)
N1-H1A···O6	0.88	1.92	2.781(4)	165.1
N2-H2A···O6	0.88	2.09	2.947(4)	163.9
N3-H3A···O5	0.88	1.89	2.751(4)	163.9
N4-H4···O5	0.88	1.96	2.816(4)	164.9

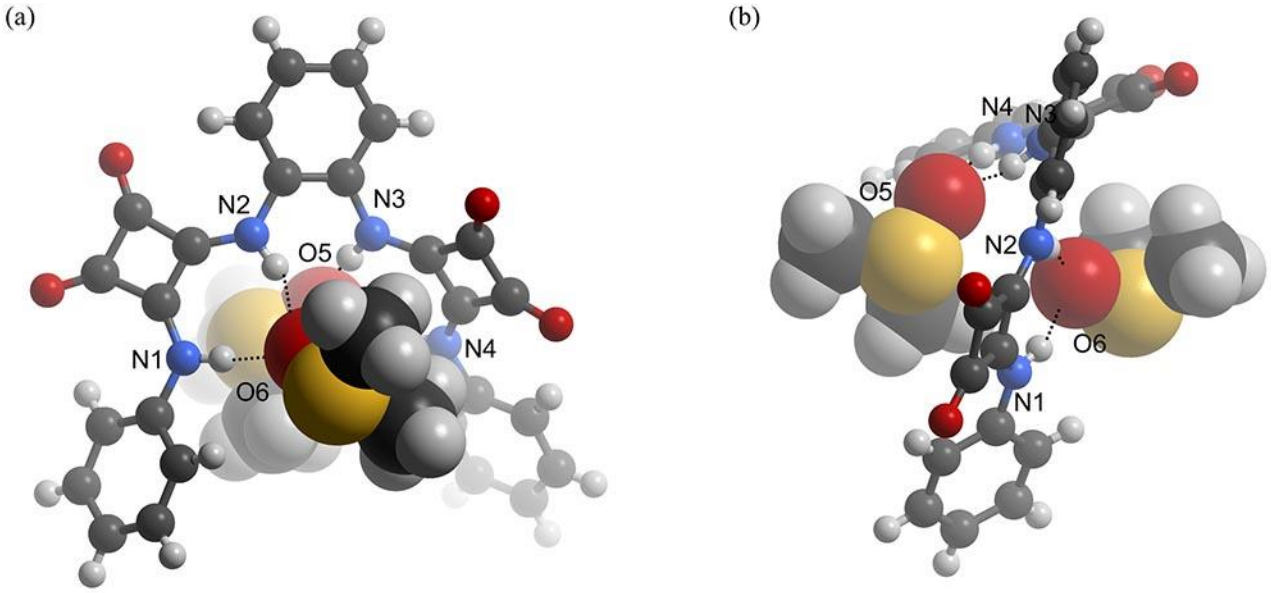

Figure S8. Schematic representation of the intermolecular hydrogen bonds in the crystal of **C2·(DMSO)$_2$**. For clarity, only atoms involved in hydrogen bonding are labelled. Hydrogen bonds are represented by dashed lines. DMSO molecules are shown in space fill (at 2/3 the van der Waals radius) (a) Front view. (b) Side view.

Phosphate complex of **C1**

Single crystals suitable for X-ray diffraction were obtained from the slow evaporation at 50° C of a DMSO solution of **C1** in the presence of excess tetrabutylammonium dihydrogenphosphate ($TBAH_2PO_4$). The crystals were run at the University of Southampton on a *Rigaku AFC11* quarter chi goniometer equipped with an enhanced sensitivity (HG) *Saturn944+* detector mounted at the window of *007 HF* copper rotating anode generator with *Varimax optics*. The crystal was kept at T = 100(2) K during data collection with an Oxford Cryosystems low-temperature apparatus. Cell determination, data collection, data reduction and cell refinement & absorption correction were preformed using *CrystalClear-SM Expert 2.0 r7* (Rigaku, 2011). Using *Olex2* (Dolomanov et al., 2009), the structure was solved with the ShelXT (Sheldrick, 2015) structure solution program, using the Direct Methods solution method. The model was refined with ShelXL (Sheldrick, 2015) using Least Squares minimisation. Graphics were generated using MERCURY 3.0 or ViewerLite and Pov-Ray. The non-hydrogen atoms were refined anisotropically till convergence. Hydrogen atoms were stereochemically fixed at idealised positions and then refined isotropically. The structure contains solvent accessible voids in which the electron density was treated using a solvent mask. The most likely solvent is additional DMSO molecules. Disorder was also present in the tetrabutylammonium counter cations, which were modelled over two positions where necessary and by using various DFIX, DANG, RIGU, ISOR and EADP commands. Hydrogen bonds are calculated using the HTAB command in ShelXL. The structure was deposited with the Cambridge Crystallographic Database Centre (CCDC) and assigned the number CCDC 1460288.

Crystal data for **(C1)$_3$·(TBA$^+$)$_3$·(PO$_4^{3-}$)**: $C_{128}H_{168}N_{15}O_{17}PS$, M_r = 2251.79 g/mol, crystal size = 0.36 x 0.24 x 0.22 mm^3, pale-yellow prism, monoclinic, space group *C2/c*, a = 28.4389(4) Å, b = 15.9129(2) Å, c = 56.0834(9) Å, α = 90°, β = 91.1396(14)°, γ = 90°, V = 25375.3(7) Å^3, Z = 8, ρ_c = 1.179 g cm^{-3}, μ = 0.890 mm^{-1}, radiation and wavelength = CuKα (1.54184), T = 100(2) K, θ_{max} = 66.601, reflections collected: 129166, independent reflections: 22270 (R_{int} = 0.0392), 1485 parameters, 1302 restraints, R indices (all data): R_1 = 0.1164, wR_2 = 0.3924, final R indices [$I > 2\sigma I$]: R_1 = 0.1102, wR_2 = 0.3782, *GOOF* = 1.869, largest diff. peak and hole = 1.366 and -0.988 e Å^3.

Table S2. Hydrogen bond properties for **(C1)$_3$·(TBA$^+$)$_3$·(PO$_4^{3-}$).**

Donor--H···Acceptor	D-H (Å)	H···A (Å)	D···A (Å)	D-H···A (°)
N101-H101···O1	0.88	1.79	2.663(4)	169.3
N102-H102···O1	0.88	1.98	2.813(4)	158.1
N103-H103···O2	0.88	1.92	2.763(4)	159.9
N201-H201···O3	0.88	1.99	2.772(4)	147.8
N202-H202···O1	0.88	2.03	2.767(4)	140.9
N204-H204···O2	0.88	1.79	2.662(4)	170.2
N301-H301···O4	0.88	1.76	2.623(3)	168.0
N302-H302···O4	0.88	2.00	2.843(4)	158.8
N303-H303···O3	0.88	2.03	2.793(3)	145.1
N304-H304···O3	0.88	1.86	2.701(3)	159.2

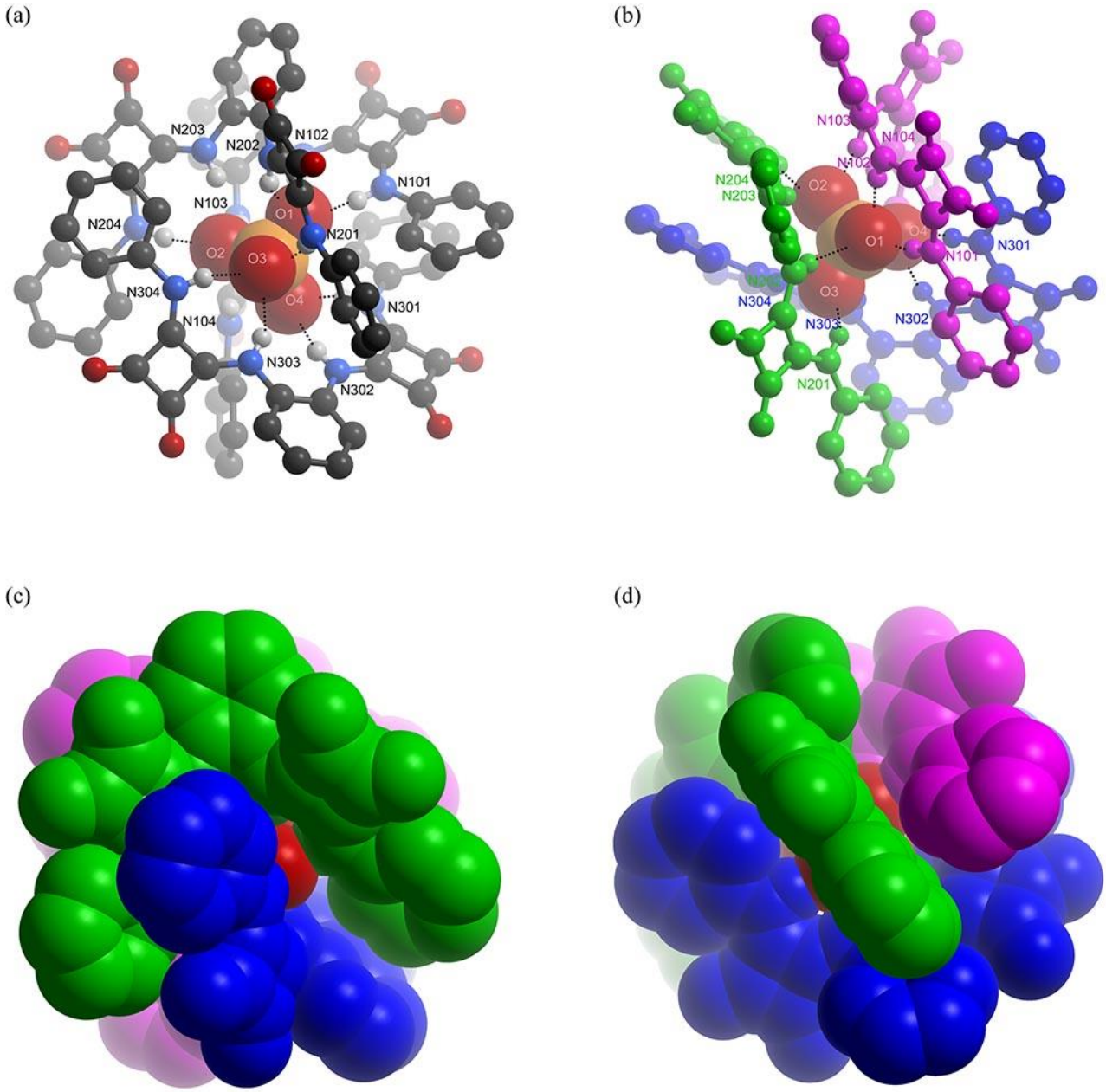

Figure S9. Schematic representations (a)-(d) of the intermolecular hydrogen bonds in the crystal of **$(C1)_3\cdot(TBA^+)_3\cdot(PO_4^{3-})$**. For clarity, only atoms involved in hydrogen bonding are labelled and TBA^+ counterions, DMSO molecules and non-hydrogen bonding hydrogen atoms are omitted. Hydrogen bonds are represented by dashed lines.

S3. ANION TRANSPORT STUDIES IN LIPOSOMES

S3.1. General protocol

This procedure describes a typical membrane transport tests. Internal and external solutions can vary and are detailed in the caption of the figures. Chloride concentrations during transport experiments were determined using an *Accumet* chloride-selective electrode. The electrode was calibrated against sodium chloride solutions of known concentrations prior to each experiment according to the supplier's manual. POPC (1-palmitoyl-2-oleoyl-*sn*-glycero-3-phosphocholine) was supplied by *Genzyme* and was stored at –20° C as a solution in chloroform (1 g POPC in 35 mL chloroform). Cholesterol was supplied by *Sigma-Aldrich*. Octaethylene glycol monododecyl ether was used as detergent and was supplied by *TCI*.

A lipid film of POPC or 7:3 POPC:cholesterol was formed from a chloroform solution under reduced pressure and dried under vacuum for at least 4 hours. The lipid film was rehydrated by vortexing with a metal chloride (MCl) salt solution. The lipid suspension was then subjected to nine freeze-thaw cycles, where the suspension was alternatingly allowed to freeze in a liquid nitrogen bath, followed by thawing in a water bath. The lipid suspension was allowed to age for 30 min at room temperature and was subsequently extruded 25 times through a 200 nm polycarbonate membrane (*Nucleopore*^{TM}) using a LiposoFast-Basic extruder set (*Avestin, Inc*). The resulting unilamellar vesicles were dialysed (*Spectra/Por® 2* Membrane MWCO 12-14 kD) against the external medium to remove unencapsulated MCl salts. Internal and external solutions vary from experiment to experiment, but in all cases an ionic strength of 500 mM was used. The results for compounds **A1-A3**, **B2**, **C2-C3** and **D2-D3** have been reported elsewhere,[1, 2, 7] and are given here for comparison with compounds **B1**, **B3**, **C1** and **D1**.

S3.2. Chloride/nitrate transport assay

Unilamellar POPC vesicles containing 489 mM NaCl buffered to pH 7.2 with 5 mM phosphate salts, prepared as described in Section S3.1., were suspended in the external medium consisting of 489 mM $NaNO_3$ solution buffered to pH 7.2 with 5 mM phosphate salts. The lipid concentration per sample was 1 mM. A DMSO solution of the carrier molecule was added at a concentration of 1 mol% carrier with respect to lipid to start the experiment, and the chloride efflux was monitored using a chloride sensitive electrode. At 5 min, the vesicles were lysed with 50 μL of octaethylene glycol monododecyl ether (0.232 mM in 7:1 water:DMSO v/v) and a final chloride reading was taken at 7

min. The electrode readings were converted to chloride concentrations using a standard calibration and the initial value was subsequently set at 0% chloride efflux and the final chloride reading (at 7 minutes) was set as 100% chloride efflux. All other data points were converted to percentages using these points. For very active compounds, the initial rate of chloride release (k_{ini}) can be calculated by fitting the obtained chloride efflux with the asymptotic function $y = a - b \cdot c^x$ using Origin 9.1, where y is the chloride efflux (%), x is time (s) and k_{ini} is then given by $k_{ini} = -b \cdot ln(c)$ (obtained in % s^{-1}). For compounds with a low activity, the initial rate of chloride release (k_{ini}) can be calculated by fitting the initial linear range of the obtained chloride efflux to $y = a + b \cdot x$, where y is the chloride efflux (%), x is time (s) and k_{ini} is given by the slope b. In case of a sigmoidal time dependence, the first two or three datapoints were omitted from the fit.

As illustrated in Figure S10, the **D**-series is not active in all conditions, while the **A**, **B** and **C** compounds have various degrees of chloride transport ability, depending on the degree of fluorination (**C** > **A** > **B** for unfluorinated compounds, **A** > **C** > **B** for *para*-CF_3 compounds and **A** > **B** > **C** for *meta*-CF_3 compounds).

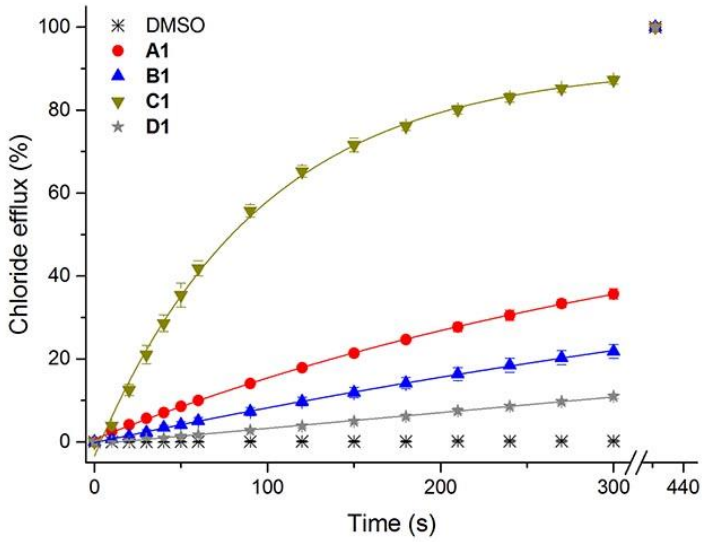

Model	Asymptotic1		
Equation	y = a-b*c^x		
Reduced C	0.05153	0.02174	2.20568
Adj. R-Squ	0.99964	0.99962	0.99774
		Value	Standard Error
A1	a	65.15513	2.44305
	b	64.53244	2.36553
	c	0.9974	1.40026E-4
B1	a	68.51595	6.20069
	b	68.69336	6.14881
	c	0.9987	1.40833E-4
C1	a	90.90067	1.3142
	b	94.28475	1.28693
	c	0.98952	4.46164E-4

Model	Line		
Equation	y = A + B*x		
Reduced Ch	0.0188		
Adj. R-Squa	0.99866		
		Value	Standard Er
D1	A	-0.50357	0.06085
--	B	0.03782	3.84235E-4

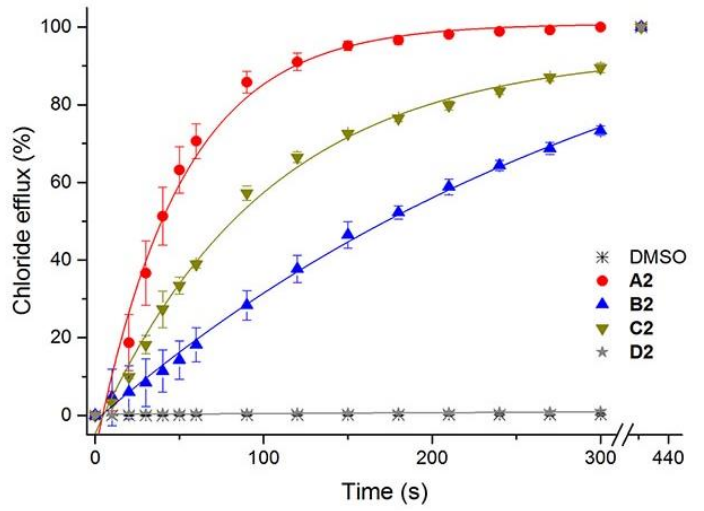

Model	Asymptotic1		
Equation	y = a-b*c^x		
Reduced C	20.52346	1.91153	5.63255
Adj. R-Squ	0.98467	0.99716	0.99463
		Value	Standard Error
A2	a	100.86427	2.15015
--	b	109.84567	3.75466
--	c	0.98066	0.00157
B2	a	127.64295	11.74882
--	b	129.00842	11.28225
--	c	0.99706	3.96835E-4
C2	a	93.68213	2.27257
--	b	98.35665	2.14626
--	c	0.99008	6.75003E-4

Model	Line		
Equation	y = A + B*x		
Reduced Ch	0.00721		
Adj. R-Squa	0.85819		
		Value	Standard Err
D2	A	0.26712	0.0377
--	B	0.00212	2.3804E-4

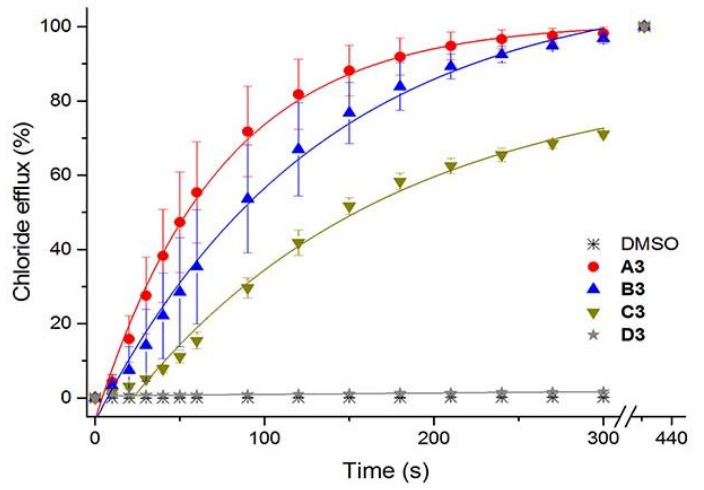

Model	Asymptotic1		
Equation	y = a-b*c^x		
Reduced C	6.53164	9.23738	6.65133
Adj. R-Squ	0.99497	0.99317	0.9906
		Value	Standard Error
A3	a	101.09596	1.64774
--	b	106.94892	2.03311
--	c	0.9865	7.39653E-4
B3	a	111.62249	4.46552
--	b	117.83447	3.88255
--	c	0.99243	7.0338E-4
C3	a	87.08104	5.91899
--	b	100.56411	4.46813
--	c	0.99354	9.16207E-4

Model	Line		
Equation	y = A + B*x		
Reduced C	0.00147		
Adj. R-Squa	0.98975		
		Value	Standard Er
D3	A	0.57626	0.01701
--	B	0.00381	1.07394E-4

Figure S10. Chloride/nitrate transport mediated by the unfluorinated compounds **A1**, **B1**, **C1**, **D1** (top), *para*-CF_3 compounds **A2**, **B2**, **C2**, **D2** (middle), and *meta*-CF_3 compounds **A3**, **B3**, **C3**, **D3** (bottom), at 1 mol% with respect to lipid. Unilamellar POPC vesicles were loaded with a 489 mM NaCl solution buffered to pH 7.2 with 5 mM phosphate, and were suspended in a 489 mM $NaNO_3$ solution buffered to pH 7.2 with 5 mM phosphate salts. At the end of the experiment (300 s), detergent was added to lyse the vesicles and calibrate the ISE to 100% chloride efflux. Each point represents the average of a minimum of 3 repeats. DMSO was used as a control. Lines represent asymptotic or linear fits to calculate k_{ini}. For the the unfluorinated compounds, activity follows **C** > **A** > **B** > **D**; while for the *para*-CF_3 compounds it is **A** > **C** > **B** > **D**; and for the *meta*-CF_3 compounds it is **A** > **B** > **C** > **D**.

S3.3. Chloride/bicarbonate transport assay

Unilamellar POPC vesicles containing 450 mM NaCl buffered to pH 7.2 with 20 mM phosphate salts, prepared as described in Section S3.1., were suspended in the external medium consisting of 162 mM Na_2SO_4 solution buffered to pH 7.2 with 20 mM phosphate salts. The lipid concentration per sample was 1 mM. A DMSO solution of the carrier molecule was added at a concentration of 1 mol% carrier with respect to lipid to start the experiment, and the chloride efflux was monitored using a chloride sensitive electrode. After 2 min, a small amount of a $NaHCO_3$ solution was added to achieve a total $NaHCO_3$ concentration of 40 mM. At 7 min, the vesicles were lysed with 50 μL of octaethylene glycol monododecyl ether (0.232 mM in 7:1 water:DMSO v/v) and a final chloride reading was taken at 9 min. The electrode readings were converted to chloride concentrations using a standard calibration and the initial value was subsequently set at 0% chloride efflux and the final chloride reading (at 9 minutes) was set as 100% chloride efflux. All other data points were converted to percentages using these points. For very active compounds, the initial rate of chloride release (k_{ini}) can be calculated by fitting the obtained chloride efflux after the addition of $NaHCO_3$ with the asymptotic function $y = a - b \cdot c^x$ using Origin 9.1, where y is the chloride efflux (%), x is time (s) and k_{ini} is then given by $k_{ini} = -b \cdot ln(c) \cdot c^{120}$ (derivative at t = 120s, obtained in % s^{-1}). For compounds with a low activity, the initial rate of chloride release (k_{ini}) can be calculated by fitting the initial linear range of the obtained chloride efflux after the addition of $NaHCO_3$ to $y = a + b \cdot x$, where y is the chloride efflux (%), x is time (s) and k_{ini} is given by the slope b.

None of the compounds in the **D**-series were capable of mediating Cl^-/HCO_3^- transport. **A**, **B** and **C** compounds have various degrees of chloride transport ability, depending on the nature of fluorination (**C** > **A** > **B** for unfluorinated compounds, **A** ≈ **C** > **B** for *para*-CF_3 compounds and **A** > **B** > **C** for *meta*-CF_3 compounds). The relative transport abilities for the tested compounds was similar for Cl^-/NO_3^- transport (Section S3.2.) and Cl^-/HCO_3^- transport (Section S3.3.).

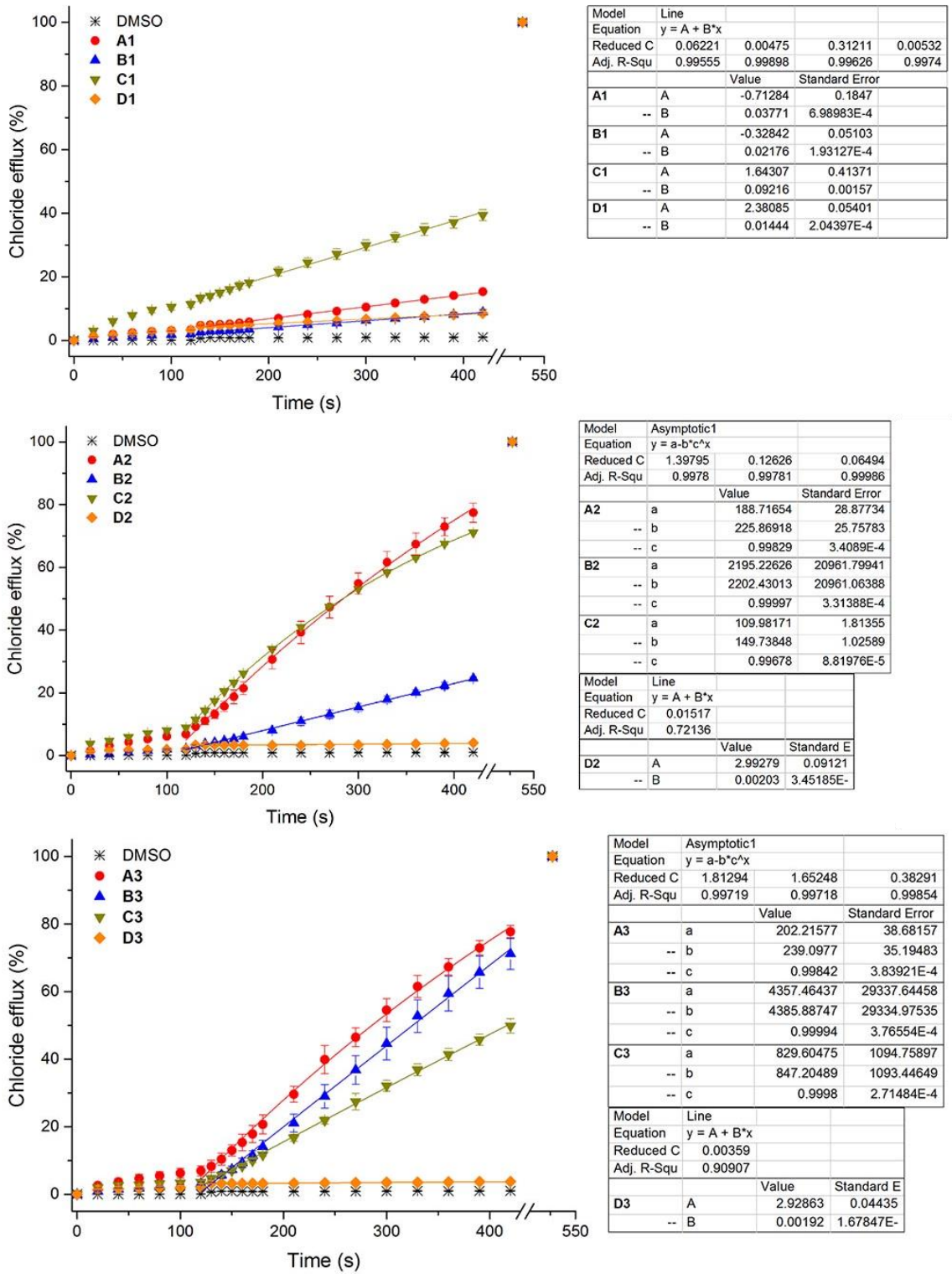

Model	Line			
Equation	y = A + B*x			
Reduced C	0.06221	0.00475	0.31211	0.00532
Adj. R-Squ	0.99555	0.99898	0.99626	0.9974
		Value	Standard Error	
A1	A	-0.71284	0.1847	
--	B	0.03771	6.98983E-4	
B1	A	-0.32842	0.05103	
--	B	0.02176	1.93127E-4	
C1	A	1.64307	0.41371	
--	B	0.09216	0.00157	
D1	A	2.38085	0.05401	
--	B	0.01444	2.04397E-4	

Model	Asymptotic1		
Equation	y = a-b*c^x		
Reduced C	1.39795	0.12626	0.06494
Adj. R-Squ	0.9978	0.99781	0.99986
		Value	Standard Error
A2	a	188.71654	28.87734
--	b	225.86918	25.75783
--	c	0.99829	3.4089E-4
B2	a	2195.22626	20961.79941
--	b	2202.43013	20961.06388
--	c	0.99997	3.31388E-4
C2	a	109.98171	1.81355
--	b	149.73848	1.02589
--	c	0.99678	8.81976E-5

Model	Line	
Equation	y = A + B*x	
Reduced C	0.01517	
Adj. R-Squ	0.72136	
	Value	Standard E
D2 A	2.99279	0.09121
-- B	0.00203	3.45185E-

Model	Asymptotic1		
Equation	y = a-b*c^x		
Reduced C	1.81294	1.65248	0.38291
Adj. R-Squ	0.99719	0.99718	0.99854
		Value	Standard Error
A3	a	202.21577	38.68157
--	b	239.0977	35.19483
--	c	0.99842	3.83921E-4
B3	a	4357.46437	29337.64458
--	b	4385.88747	29334.97535
--	c	0.99994	3.76554E-4
C3	a	829.60475	1094.75897
--	b	847.20489	1093.44649
--	c	0.9998	2.71484E-4

Model	Line	
Equation	y = A + B*x	
Reduced C	0.00359	
Adj. R-Squ	0.90907	
	Value	Standard E
D3 A	2.92863	0.04435
-- B	0.00192	1.67847E-

Figure S11. Chloride/bicarbonate transport mediated by the unfluorinated compounds **A1**, **B1**, **C1**, **D1** (top), *para*-CF_3 compounds **A2**, **B2**, **C2**, **D2** (middle), and *meta*-CF_3 compounds **A3**, **B3**, **C3**, **D3** (bottom), at 1 mol% with respect to lipid. Unilamellar POPC vesicles were loaded with 450 mM NaCl buffered to pH 7.2 with 20 mM sodium phosphate salts. The vesicles were dispersed in 162 mM Na_2SO_4 buffered to pH 7.2 with 20 mM sodium phosphate salts. At t = 120s, a solution of $NaHCO_3$ was added to give a 40 mM external concentration. At the end of the experiment, detergent was added to lyse the vesicles and calibrate the ISE to 100 % chloride efflux. Each point represents the average of a minimum of 3 repeats. DMSO was used as a control. Lines represent asymptotic or linear fits to calculate k_{ini}. For the the unfluorinated compounds, activity follows **C** > **A** > **B** ≈ **D**; while for the *para*-CF_3 compounds it is **A** ≈ **C** > **B** > **D**; and for the *meta*-CF_3 compounds it is **A** > **B** > **C** > **D**.

S3.4. Hill plots

Hill plots corresponding to the chloride/nitrate or chloride/bicarbonate transport assays were constructed as described above (Sections S3.2. and S3.3.) for various concentrations of carrier. The chloride efflux (%) 270 s after the addition of carrier is plotted as a function of the carrier concentration. Data points can then be fitted to the Hill equation using Origin 9.1: $y = V_{\max} \frac{x^n}{k + x^n}$, where *y* is the chloride efflux at 270 s (%) and *x* is the carrier concentration (mol% carrier to lipid). V_{max}, *k* and *n* are the parameters to be fitted. V_{max} is the maximum efflux possible, *n* is the Hill coefficient and *k* is the carrier concentration needed to reach $V_{max}/2$. From the Hill plot it is therefore possible to obtain $EC_{50,270s}$ values, defined as the carrier concentration (mol% carrier to lipid) needed to obtain 50% chloride efflux after 270 s. In the case of the chloride/bicarbonate assays, the Hill equation was adapted to the 120 s time delay before the addition of bicarbonate: $y = V_{\min} + (V_{\max} - V_{\min}) \frac{x^n}{k^n + x^n}$. An overview of the obtained $EC_{50,270s}$ values can be found in Table S3 and Table S4. The Hill plots of **A1-A3**, **B2**, **C2-C3**, **D2-D3** and **E1-E3** have been previously published,[1, 2, 7] while **D1** was not active enough to allow Hill plots to be constructed.

Table S3. Overview of Cl^-/NO_3^- assays of compounds **A1-D3**. Errors are between brackets.

	k_{ini} [a] (% s^{-1})	V_{max} [b] (%)	k [b] (mol%)	n [b]	$EC_{50,270s}$ [b] (mol%)
A1	0.168 [c]	118 (9) [d]	1.6 (0.2) [d]	1.7 (0.2) [d]	1.379 [d]
A2	2.145 [c]	103 (2) [d]	0.065 (0.002) [d]	1.22 (0.09) [d]	0.062 [d]
A3	1.454 [c]	98 (2) [d]	0.010 (0.001) [d]	1.10 (0.05) [d]	0.010 [d]
B1	0.089	- [e]	- [e]	- [e]	- [e]
B2	0.380 [f]	71 (3) [f]	0.13 (0.01) [f]	2.0 (0.3) [f]	0.209 [f]
B3	0.895	97 (2)	0.115 (0.008)	1.4 (0.1)	0.120
C1	0.993	102 (2)	0.36 (0.01)	1.6 (0.1)	0.357
C2	0.980 [f]	90 (1) [f]	0.072 (0.002) [f]	1.22 (0.05) [f]	0.085 [f]
C3	0.652 [f]	92 (11) [f]	0.13 (0.06) [f]	0.7 (0.2) [f]	0.164 [f]
D1	0.038	- [e]	- [e]	- [e]	- [e]
D2	0.0021 [f]	- [e],[f]	- [e],[f]	- [e],[f]	- [e],[f]
D3	0.0038 [f]	- [e],[f]	- [e],[f]	- [e],[f]	- [e],[f]

[a] Initial rate of chloride efflux for 1 mol% carrier to lipid, calculated as described in S3.2. [b] Parameters from Hill plot. [c] Recalculated from reference 1. [d] Values taken from reference 1. [e] Accurate Hill analysis could not be performed due to low activity. [f] Values taken from reference 2. [g] Recalculated from reference 4. [h] Values taken from reference 4.

Table S4. Overview of Cl^-/HCO_3^- assays of compounds **A1-D3**. Errors are between brackets.

	k_{ini} [a] (% s^{-1})	V_{min} [b] (%)	V_{max} [b] (%)	k [b] (mol%)	n [b]	$EC_{50,270s}$ [b] (mol%)
A1	0.038 [c]	5 (1) [d]	100 [d]	4.2 (0.2) [d]	1.6 (0.1) [d]	3.90 [d]
A2	0.315 [c]	6 (3) [d]	108 (4) [d]	0.56 (0.04) [d]	1.3 (0.2) [d]	0.446 [d]
A3	0.313 [c]	13 (5) [d]	100 [d]	0.42 (0.09) [d]	1.2 (0.2) [d]	0.33 [d]
B1	0.022	- [e]	- [e]	- [e]	- [e]	- [e]
B2	0.066 [f]	- [e],[f]	- [e],[f]	- [e],[f]	- [e],[f]	- [e],[f]
B3	0.261	7 (9)	100 (14)	0.6 (0.1)	2.0 (0.8)	0.57
C1	0.092	0	100	1.36 (0.09)	1.3 (0.1)	1.36
C2	0.328 [f]	-6 (6) [f]	87 (5) [f]	0.19 (0.03) [f]	0.79 (0.14) [f]	0.319 [f]
C3	0.165 [f]	-20 (13) [f]	92 (23) [f]	0.6 (0.3) [f]	0.39 (0.14) [f]	2.172 [f]
D1	0.014	- [e]	- [e]	- [e]	- [e]	- [e]
D2	0.0020 [f]	- [e],[f]	- [e],[f]	- [e],[f]	- [e],[f]	- [e],[f]
D3	0.0019 [f]	- [e],[f]	- [e],[f]	- [e],[f]	- [e],[f]	- [e],[f]

[a] Initial rate of chloride efflux for 1 mol% carrier to lipid, calculated as described in S3.3. [b] Parameters from Hill plot. [c] Recalculated from reference 1. [d] Values taken from reference 1. [e] Accurate Hill analysis could not be performed due to low activity. [f] Values taken from reference 2.

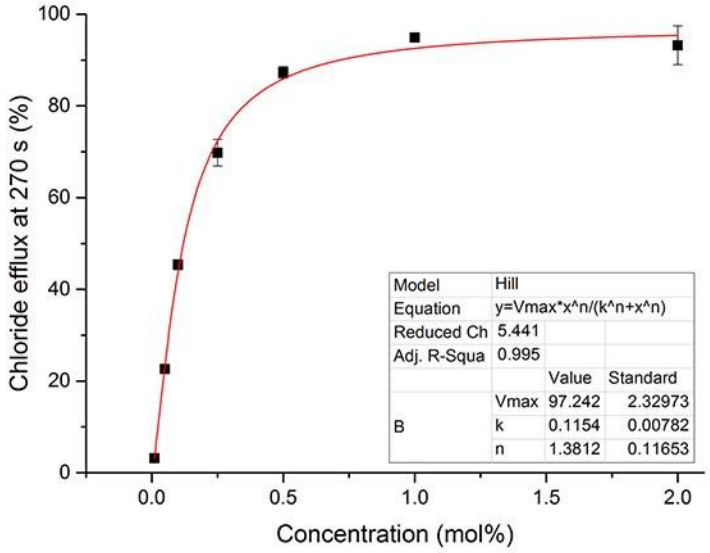

Figure S12. **Hill plot for chloride/nitrate transport mediated by receptor B3.** Unilamellar POPC vesicles were loaded with 489 mM NaCl buffered to pH 7.2 with 5 mM sodium phosphate salts. The vesicles were dispersed in 489 mM $NaNO_3$ buffered to pH 7.2 with 5 mM sodium phosphate salts. Chloride efflux was measured at 270 s. Each point represents the average of a minimum of three repeats and error bars represent standard deviations. Concentrations used: 0.01 mol%, 0.05 mol%, 0.1 mol%, 0.25 mol%, 0.5 mol%, 1 mol%, 2 mol% with respect to lipid.

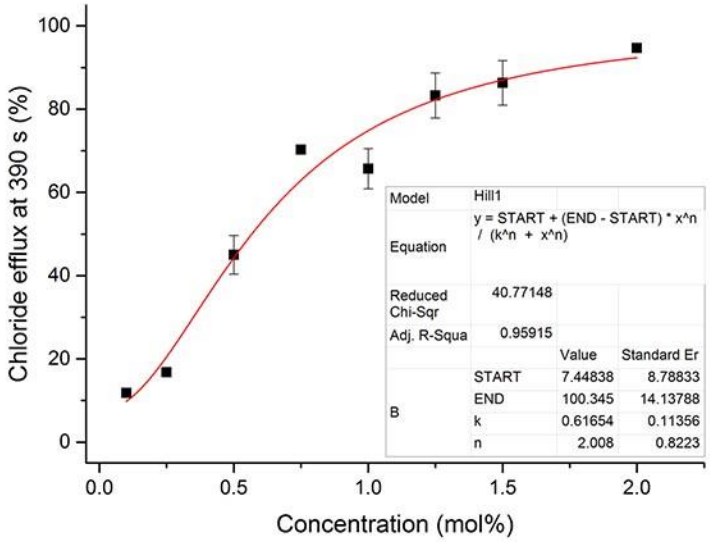

Figure S13. **Hill plot for chloride/bicarbonate transport mediated by receptor B3.** Unilamellar POPC vesicles were loaded with 450 mM NaCl buffered to pH 7.2 with 20 mM sodium phosphate salts. The vesicles were dispersed in 162 mM Na_2SO_4 buffered to pH 7.2 with 20 mM sodium phosphate salts. At t = 120 s, a solution of $NaHCO_3$ was added to give a 40 mM external concentration. Chloride efflux was measured 270 s after the addition of $NaHCO_3$. Each point represents the average of a minimum of three repeats and error bars represent standard deviations. Concentrations used: 0.1 mol%, 0.25 mol%, 0.5 mol%, 0.75 mol%, 1 mol%, 1.25 mol%, 1.5 mol%, 2 mol% with respect to lipid.

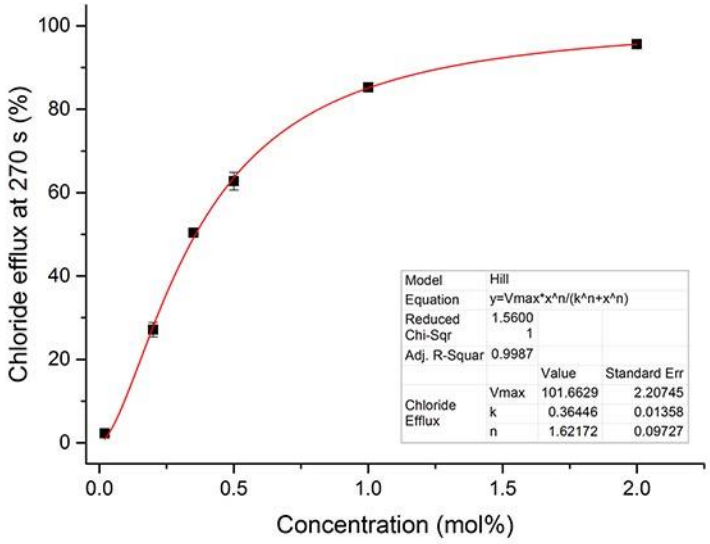

Figure S14. **Hill plot for chloride/nitrate transport mediated by receptor C1.** Unilamellar POPC vesicles were loaded with 489 mM NaCl buffered to pH 7.2 with 5 mM sodium phosphate salts. The vesicles were dispersed in 489 mM $NaNO_3$ buffered to pH 7.2 with 5 mM sodium phosphate salts. Chloride efflux was measured at 270 s. Each point represents the average of a minimum of three repeats and error bars represent standard deviations. Concentrations used: 0.02 mol%, 0.2 mol%, 0.35 mol%, 0.5 mol%, 1 mol%, 2 mol% with respect to lipid.

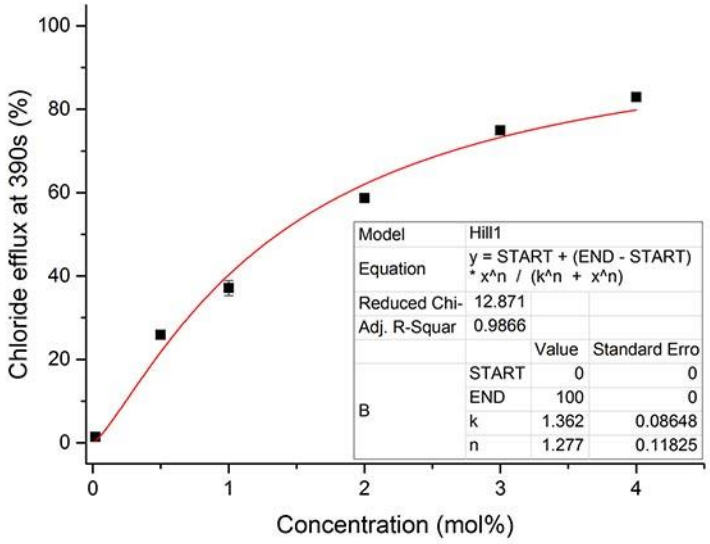

Figure S15. **Hill plot for chloride/bicarbonate transport mediated by receptor C1.** Unilamellar POPC vesicles were loaded with 450 mM NaCl buffered to pH 7.2 with 20 mM sodium phosphate salts. The vesicles were dispersed in 162 mM Na_2SO_4 buffered to pH 7.2 with 20 mM sodium phosphate salts. At t = 120 s, a solution of $NaHCO_3$ was added to give a 40 mM external concentration. Chloride efflux was measured 270 s after the addition of $NaHCO_3$. Each point represents the average of a minimum of three repeats and error bars represent standard deviations. Concentrations used: 0.02 mol%, 0.5 mol%, 1 mol%, 2 mol%, 3 mol%, 4 mol% with respect to lipid.

S3.5. Metal chloride symport assays

Unilamellar POPC vesicles containing a 450 mM MCl (M = Na, K, Cs) solution buffered to pH 7.2 with 20 mM phosphate salts, prepared as described in Section S3.1, were suspended in the external medium consisting of a 162 mM Na_2SO_4 solution buffered to pH 7.2 with 20 mM phosphate salts. The lipid concentration per sample was 1 mM. A DMSO solution of the carrier molecule was added at a concentration of 4 mol% carrier with respect to lipid to start the experiment, and the chloride efflux was monitored using a chloride sensitive electrode (a high concentration of transporter was used in order to be able to see any chloride efflux). At 5 min, the vesicles were lysed with 50 μL of octaethylene glycol monododecyl ether (0.232 mM in 7:1 water:DMSO v/v) and a final chloride reading was taken at 7 min. The electrode readings were converted to chloride concentrations using a standard calibration and the initial value was subsequently set at 0% chloride efflux and the final chloride reading (at 7 minutes) was set as 100% chloride efflux. All other data points were converted to percentages using these points.

The results for **A2**, **B2**, **C2-C3** and **D2-D3** have been previously published,[1, 2, 7] and they all showed no significant difference in chloride transport rates between Na^+, K^+ and Cs^+, indicating that metal chloride symport is not mediated by squaramides. Also ^{23}Na NMR experiments have previously confirmed that the squaramides are unable to transport metal ions across phospholipid bilayers.[2] Squaramides **A1**, **A3**, **B1**, **B3**, **C1** and **D1** also showed little to no ability of metal chloride transport (Figure S16). Compounds **B3** and **C1** do show significant chloride release under these conditions, but the differences between Na^+, K^+ and Cs^+ are within the experimental error (the errors are quite large). Additional evidence that **B3** and **C1** are not able to facilitate metal chloride symport, came from ^{23}Na NMR assays (Section S3.6.). The observed chloride efflux in Figure S16 is therefore more likely the result of Cl^-/SO_4^{2-} antiport (see also Section S3.7.), as was previously shown for squaramides **A2** and **C2**.[2]

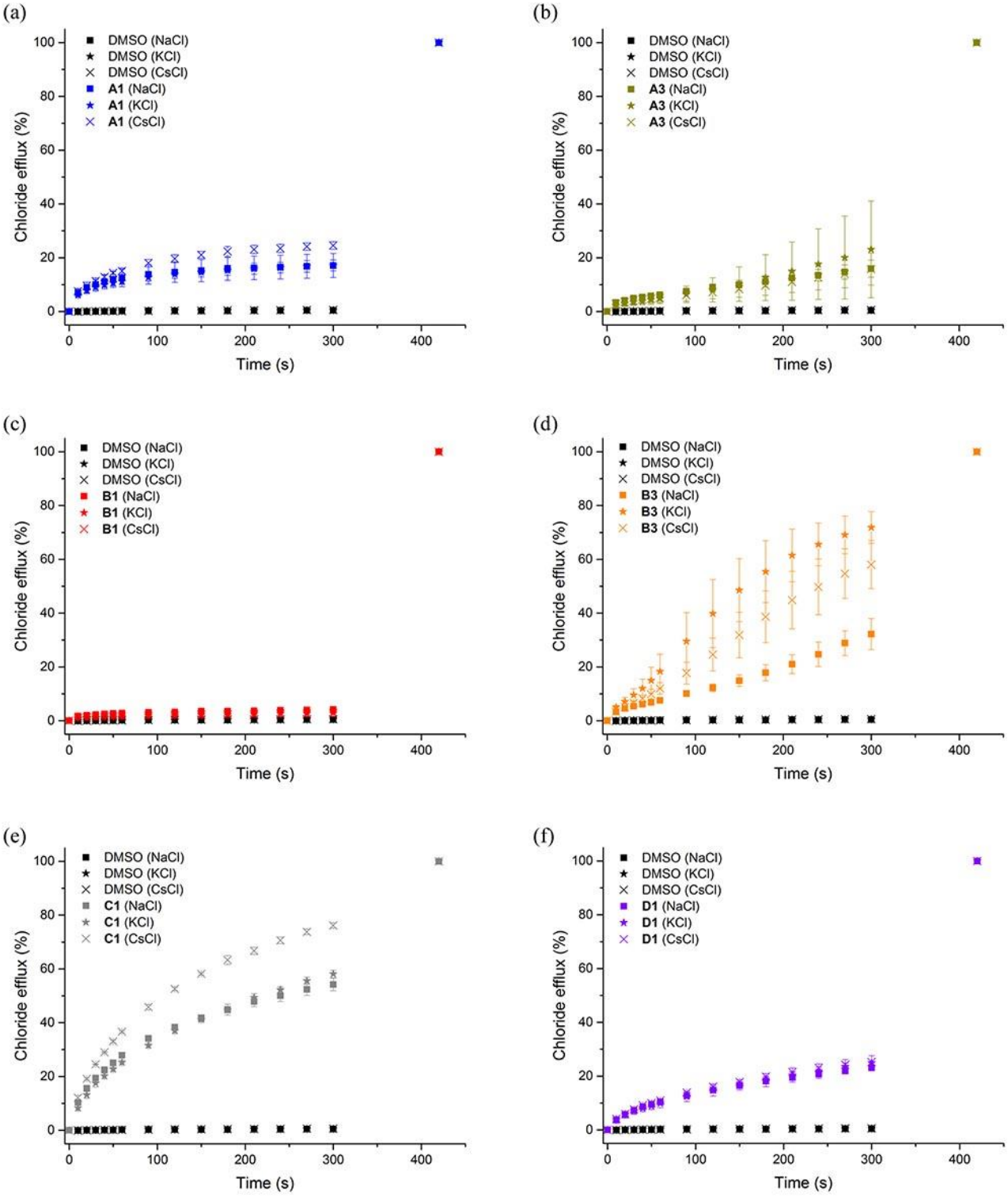

Figure S16. Inability of M^+/Cl^- symport mediated by compounds A1, A3, B1, B3, C1 and D1 (4 mol% with respect to lipid). Unilamellar POPC vesicles were loaded with 450 mM MCl (M = Na, K or Cs) buffered to pH 7.2 with 20 mM sodium phosphate salts. The vesicles were dispersed in 162 mM Na_2SO_4 buffered to pH 7.2 with 20 mM sodium phosphate salts. At the end of the experiment, detergent was added to lyse the vesicles and calibrate the ISE to 100% chloride efflux. Each point represents the average of a minimum of 3 repeats. DMSO was used as a control. (a) compound **A1**, (b) compound **A3**, (c) compound **B1**, (d) compound **B3**, (e) compound **C1**, (f) compound **D1**.

S3.6. Sodium transport NMR assay

In order to investigate whether the chloride transport observed for **B3** and **C1** in Figure S16 is due to NaCl transport, a series of ^{23}Na NMR spectroscopic experiments were carried out in order to directly detect Na^+ transport.[8] Vesicles loaded with a 450 mM NaCl solution buffered to pH 7.2 with 20 mM potassium phosphate salts, prepared as described in Section S3.1, were dispersed in an external 162 mM K_2SO_4 solution buffered to pH 7.2 with 20 mM potassium phosphate salts. An aliquot of membrane impermeable shift reagent $Dy(PPPi)_2^{7-}$ (5 mM), prepared by mixing $DyCl_3 \cdot 6H_2O$ (*Sigma Aldrich*) and sodium tripolyphosphate (*Acros*), was added to the extravesicular solution to move the extravesicular ^{23}Na resonance upfield. The vesicle suspension was transferred into the inner part of a double-walled NMR tube, of which the outer part contained D_2O to lock the magnetic field. The lipid concentration per sample was 10 mM. A DMSO solution of the carrier molecule was added at a concentration of 2 mol% carrier with respect to lipid to start the experiment, and ^{23}Na NMR measurements were carried out at 25° C at various time intervals. No sodium transport was observed upon the addition of squaramides **B3** or **C1**. Monensin, a known sodium transporter,[9] was used as a positive control and showed fast transmembrane sodium transport.

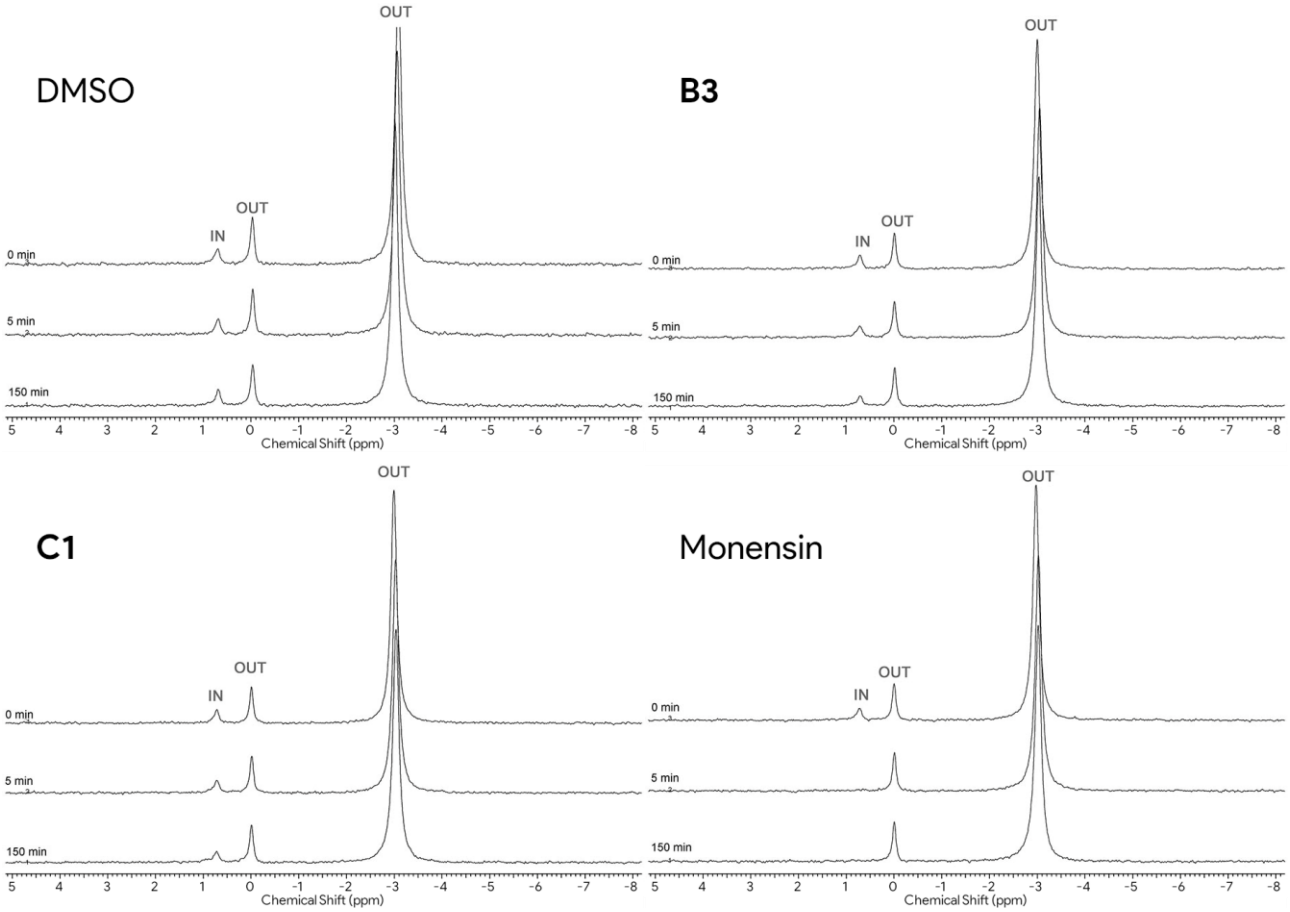

Figure S17. **Potential Na^+ transport by DMSO, B3, C1 and monensin.** ^{23}Na NMR spectrum before the addition and 5 minutes and 150 minutes after the addition of DMSO, **B3**, **C1** or monensin (2 mol% with respect to lipid) to vesicles containing 450 mM NaCl, dispersed in 162 mM K_2SO_4 solution containing $Dy(PPPi)_2^{7-}$, buffered to pH 7.2 with 20 mM potassium phosphate salts.

S3.7. Sulfate transport lucigenin assay

We have previously reported a fluorescent-based method to investigate the possibility of sulfate transport.[10] The validity of this method was later verified by the more direct investigation of sulfate transport by ^{33}S NMR spectroscopic techniques.[11] However, this last method involves the use of expensive ^{33}S labelled sulfate and the original fluorescence-based method was therefore chosen to investigate potential sulfate transport by squaramides **A1-D3**.

A lipid film of POPC was formed from a chloroform solution under reduced pressure and dried under vacuum for at least 6 hours. The lipid film was rehydrated by vortexing with a NaCl solution (2 mM lucigenin, 100 mM NaCl, 20 mM phosphate buffer at pH 7.2). The lipid suspension was then subjected to nine freeze-thaw cycles and allowed to age for 30 min at room temperature before extruding 25 times through a 200 nm polycarbonate membrane. The unincorporated lucigenin was removed by size exclusion chromatography on a Sephadex G-25 column using a sodium chloride solution as eluent (100 mM NaCl, 20 mM phosphate buffer at pH 7.2). The obtained unilamellar

POPC vesicles were subsequently suspended in a NaCl solution buffered to pH 7.2 with sodium phosphate salts. The lipid concentration per sample was 0.5 mM. The internal chloride concentration could be monitored by the fluorescence of intravesicular lucigenin after excitation at 372 nm and recording the emission at 503 nm using a *Cary Eclipse Fluorescence Spectrophotometer*. At t = 30 s, a stock salt solution was added so that the outer concentration contained 40 mM of the new salt (stock solutions: 1 M $NaNO_3$, 1 M NaCl or 0.5 M Na_2SO_4). After 80 s, a DMF solution of the carrier molecule was added to start ion transport. After 380 s, the vesicles were lysed with 30 μL of polyoxyethylene(8)lauryl ether (0.232 mM in 7:1 water:MeOH v/v).

In this experiment, there is no chloride gradient or pH gradient and HCl co-transport becomes very unlikely. The only reasonable transport mechanism that can be conceived is antiport of chloride with the anion that was spiked into the external solution at t = 30 s. The observed increase in fluorescence intensity reflects the fact that lucigenin is no longer quenched by chloride and hence that chloride is transported out of the vesicle. However, it must be noted that significant interference of the lucigenin fluorescence occurs in the presence of these squaramides (Figure S19, apparent quenching of lucigenin fluorescence). This results in the fact that the absolute changes in fluorescence are quite small. However, inactive compound **D1**, which also show interference, does not act to transport anions under these test conditions (see Figure S19). Furthermore, the addition of nitrate produces faster and more significant changes in lucigenin fluorescence than the addition of sulfate or chloride, as would be expected these changes were due to nitrate transport and not due to interference from the squaramide absorbance. These tests can therefore not be used as absolute proof of sulfate transport; however, they can give an indication of sulfate transport by the squaramides. The results of **A2**, **B2**, **C2-C3** and **D2-D3** have been previously reported and confirmed that **A2** might be able to facilitate sulfate transport.[2] The results for **A1**, **A3**, **B1**, **B3**, **C1** and **D1** are given in Figure S18 and indicate sulfate transport by **A3** and, in a small amount, by **C1**, but not by **A1**, **B1**, **B3** or **D1**. These results are different to the metal chloride symport assays (Section S3.5.), which indicated sulfate transport mediated by **B3** and **C1**. The variations are probably due to differences in the assays. Most likely, the chloride transport discussed in Section S3.5. is due to a mixture of transport mechanisms (Cl^-/SO_4^{2-}, Cl^-/OH^- (Cl^-/H^+) and a small amount of M^+/Cl^-), rather than one dominant transport mechanism.

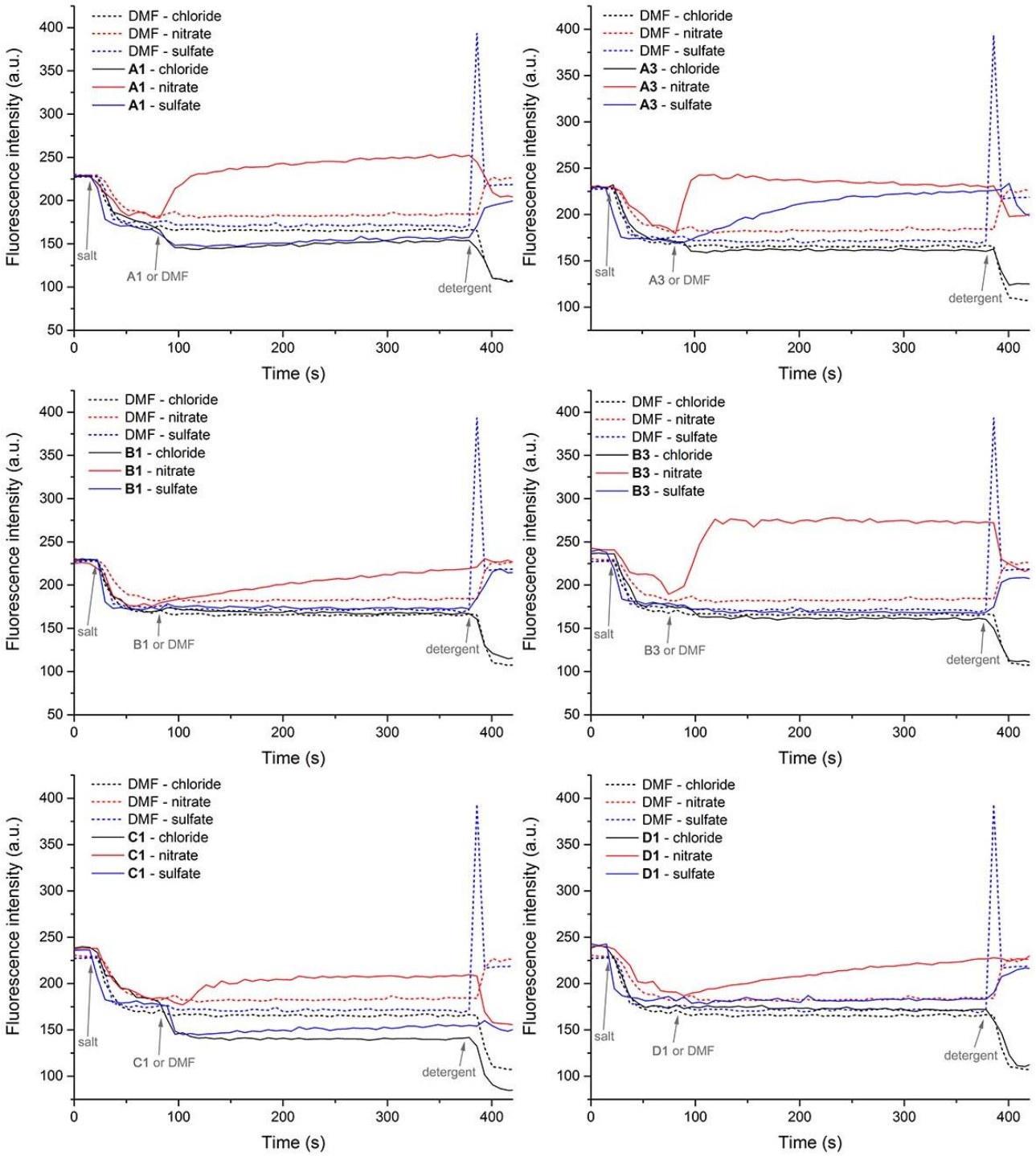

Figure S18. **Potential SO_4^{2-} transport by A1, A3, B1, B3, C1 and D1.** Unilamellar POPC vesicles were loaded with 100 mM NaCl and 2 mM lucigenin buffered to pH 7.2 with 20 mM sodium phosphate salts and dispersed in a 100 mM NaCl solution (buffered to pH 7.2). At t = 30 s, a solution of the appropriate anion was added (final concentration of 40 mM $NaNO_3$, 40 mM Na_2SO_4 or 40 mM NaCl). At t = 80 s, a DMF solution of the studied compound (4 mol% with respect to lipid) was added. At the end of the experiment (380 s), detergent was added to lyse the vesicles. Each point represents the average of three trials. DMF was used a control.

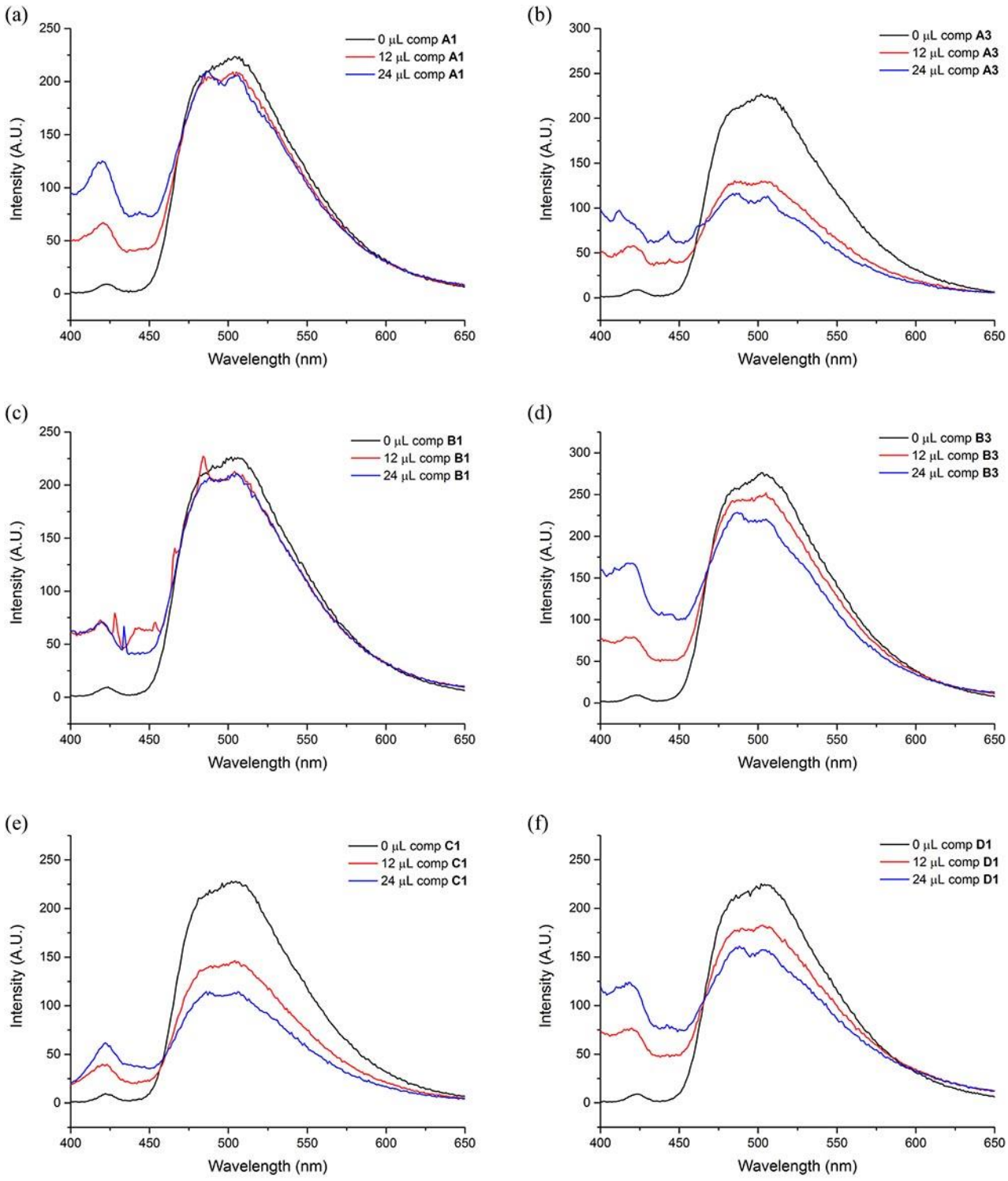

Figure S19. **Squaramide lucigenin interference.** Emission spectra of lucigenin (2 mM) in 100 mM NaCl buffered to pH 7.2 with 20 mM sodium phosphate salts, after excitation at 372 nm, in the presence of 0, 12 or 24 µL of a 5 mM DMF solution of compounds **A1-D3**. Most compounds show interference with the fluorescence of lucigenin. (a) Compound **A1**, (b) compound **A3**, (c) compound **B1**, (d) compound **B3**, (e) compound **C1**, (f) compound **D1**.

S3.8. Dissipation of transmembrane pH gradients

A lipid film of POPC was formed from a chloroform solution under reduced pressure and dried under vacuum for at least 6 hours. The lipid film was rehydrated by vortexing with a NaCl solution (1 mM HPTS (8-hydroxypyrene-1,3,6-trisulfonic acid), 489 mM NaCl, 5 mM phosphate buffer at pH 7.2 or 5 mM citrate buffer at pH 6.0). The lipid suspension was then subjected to nine freeze-thaw cycles and allowed to age for 30 min at room temperature before extruding 25 times through a 200 nm polycarbonate membrane. The unincorporated HPTS was removed by size exclusion chromatography on a Sephadex G-25 column using a sodium sulfate solution as eluent (162 mM Na_2SO_4, 5 mM phosphate buffer at pH 7.2 or 5 mM citrate buffer at pH 6.0). The thus obtained unilamellar POPC vesicles were suspended in a Na_2SO_4 solution buffered to pH 7.2 with sodium phosphate salts or to pH 6.0 with citrate buffer. The lipid concentration per sample was 1 mM. A DMSO solution of the carrier molecule was added to start the experiment (when a pH gradient was applied a small amount of the appropriate acid or base was added to the external solution just before the start of the experiment in order to achieve a pH gradient of one pH unit). The fluorescence of intravesicular HPTS was monitored by excitation at both 403 nm and 460 nm and recording the emission at 510 nm using a *Cary Eclipse Fluorescence Spectrophotometer*. At the end of the experiment, the vesicles were lysed with 30 μL of octaethylene glycol monododecyl ether (0.232 mM in 7:1 water:DMSO v/v). The internal pH was obtained by fitting the data to the following equation[7]:

$$pH = 6.94 + 0.86 \cdot \ln\left(\frac{I_{460}}{I_{403}} + 0.24\right)$$

The results for **A1-A3**, **B2**, **C2-C3** and **D2-D3** have been previously reported[2, 7] and the results for the new compounds **B1**, **B3**, **C1** and **D1** (Figure S20-Figure S23) are similar. In general, an increase in the internal pH is observed upon addition of the squaramides. Such findings support the contention that these compounds can alter the pH through H^+/Cl^- symport (or OH^-/Cl^- antiport). Bis-squaramide **C1** (and to a lesser extend **B3**) forms an exception and the initially increase in the internal pH is quickly followed by a significant decrease in the intravesicular pH (Figure S21-Figure S23). This suggests that the initial transport of HCl is later compensated by the back-transport of (sulfuric) acid, indicating formal chloride-sulfate exchange. This finding agrees with the apparent Cl^-/SO_4^{2-} transport observed for compounds **C1** and **B3** during the ion selective electrode assays (see Section S3.5, Figure S16) and leads us to suggest that some of the squaramides are capable of transporting sulfate species.

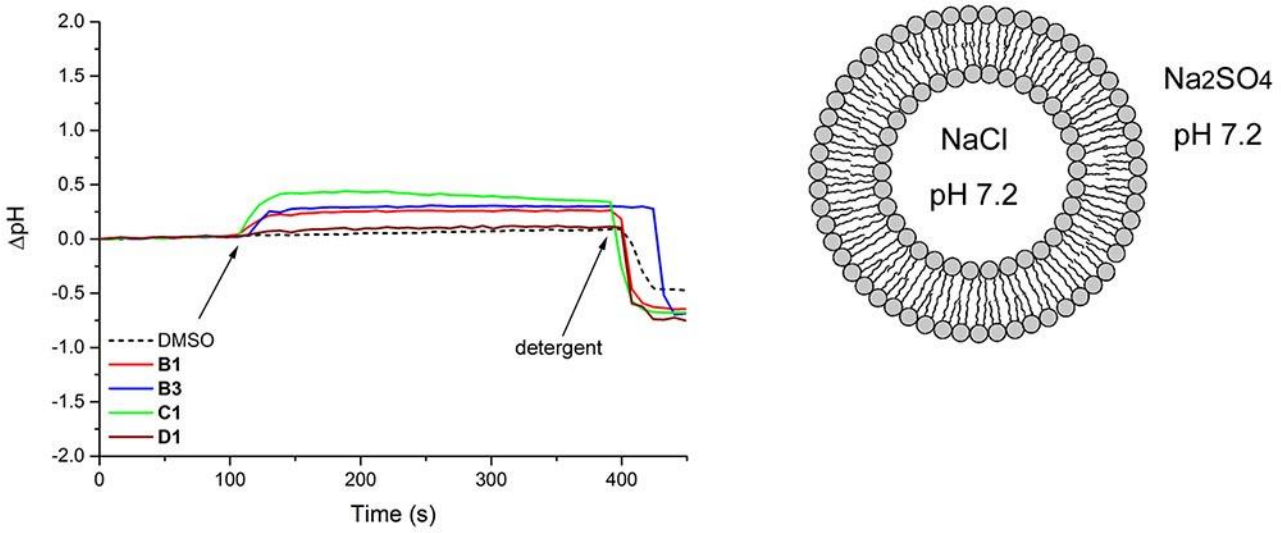

Figure S20. Investigation of HCl transport facilitated by B1, B3, C1 and D1 (4 mol%) using the fluorescent dye HPTS to estimate the change in intravesicular pH. POPC vesicles were loaded with 489 mM NaCl, 1 mM HPTS, buffered to pH 7.2 with phosphate buffer and suspended in a solution of 162 mM Na_2SO_4 buffered to pH 7.2 with phosphate buffer. At time t = 100 s, a DMSO solution of the transporter was added (4 mol% with respect to lipid) and at time t = 400 s, detergent was added. DMSO was used as a control.

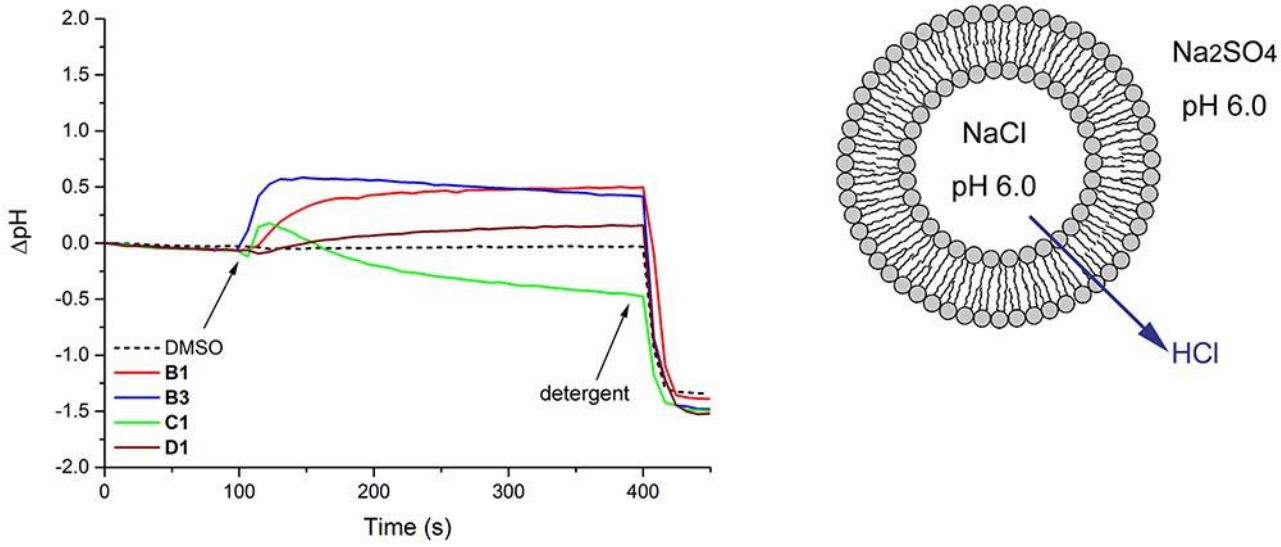

Figure S21. Investigation of HCl transport facilitated by B1, B3, C1 and D1 (4 mol%) using the fluorescent dye HPTS to estimate the change in intravesicular pH. POPC vesicles were loaded with 489 mM NaCl, 1 mM HPTS, buffered to pH 6.0 with citrate buffer and suspended in a solution of 162 mM Na_2SO_4 buffered to pH 6.0 with citrate buffer. At time t = 100 s, a DMSO solution of the transporter was added (4 mol% with respect to lipid) and at time t = 400 s, detergent was added. DMSO was used as a control.

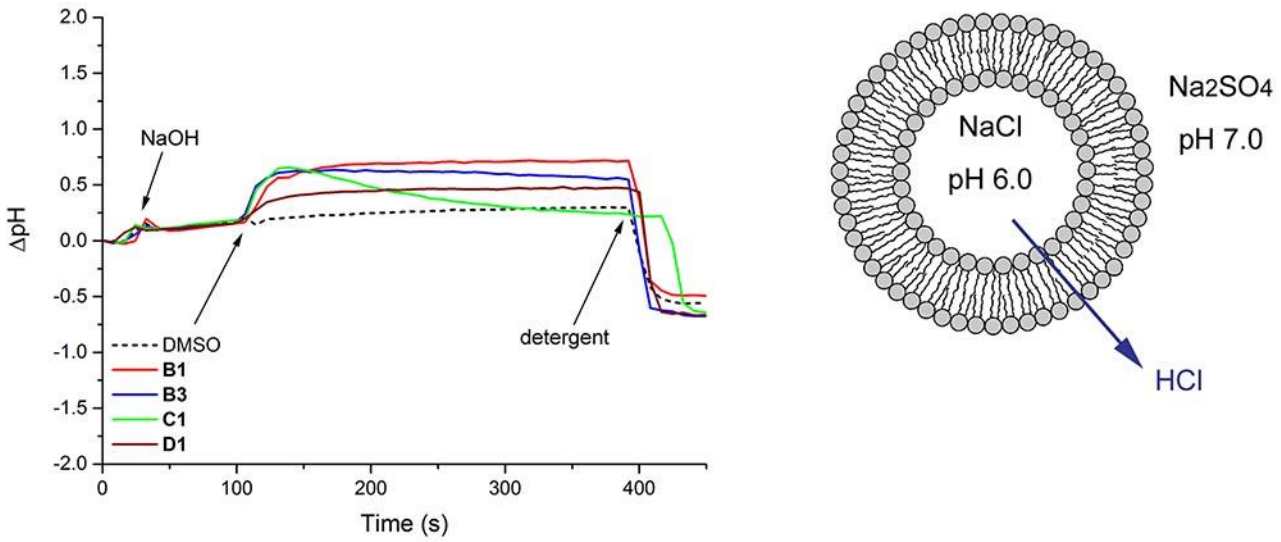

Figure S22. Investigation of HCl transport facilitated by B1, B3, C1 and D1 (4 mol%) using the fluorescent dye HPTS to estimate the change in intravesicular pH. POPC vesicles were loaded with 489 mM NaCl, 1 mM HPTS, buffered to pH 6.0 with citrate buffer, and suspended in a solution of 162 mM Na_2SO_4 buffered to pH 6.0 with citrate buffer. At time t = 20 s, a NaOH solution was added to achieve an external pH of 7.0. At time t = 100 s, a DMSO solution of the transporter was added (4 mol% with respect to lipid) and at time t = 400 s, detergent was added. DMSO was used as a control.

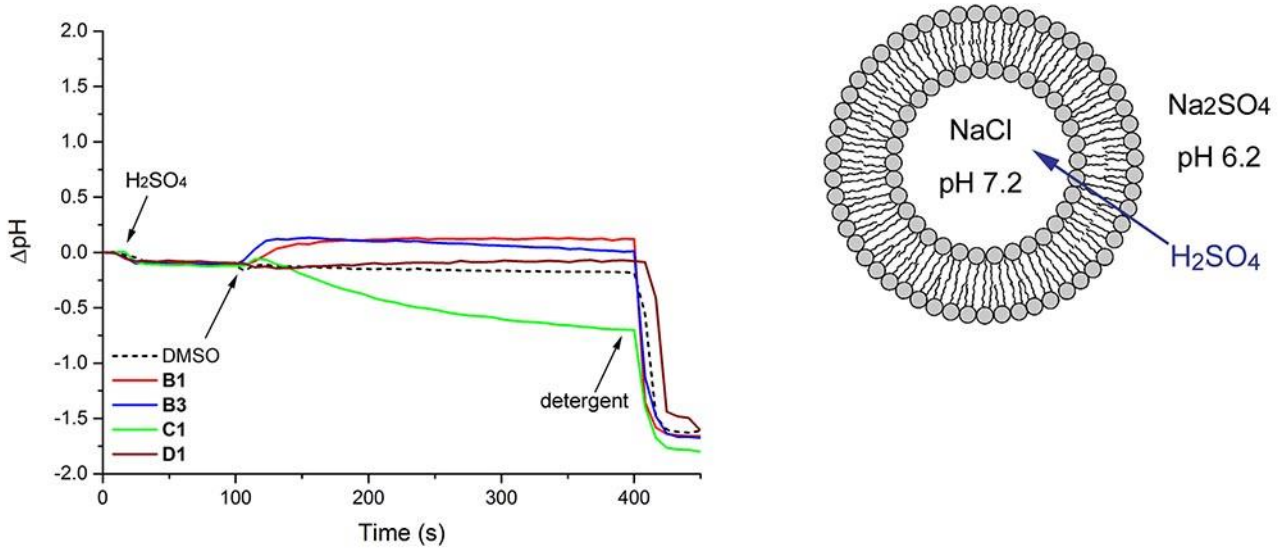

Figure S23. Investigation of HSO_4^- transport facilitated by B1, B3, C1 and D1 (4 mol%) using the fluorescent dye HPTS to estimate the change in intravesicular pH. POPC vesicles were loaded with 489 mM NaCl, 1 mM HPTS, buffered to pH 7.2 with phosphate buffer, and suspended in a solution of 162 mM Na_2SO_4 buffered to pH 7.2 with phosphate buffer. At time t = 20 s, a H_2SO_4 solution was added to achieve an external pH of 6.2. At time t = 100 s, a DMSO solution of the transporter was added (4 mol% with respect to lipid) and at time t = 400 s, detergent was added. DMSO was used as a control.

S3.9. Electrogenic vs electroneutral Cl^- transport

The assays discussed so far (Sections S3.2-S3.10) provide evidence consistent with the notion that the squaramides are able to transport Cl^-, NO_3^-, HCO_3^- and probably SO_4^{2-}, as well as dissipate transmembrane pH gradients. These tests cannot, however, discriminate between electrogenic transport (i.e., uniport of chloride where the membrane potential that is created must be compensated by a separate uniport event) or electroneutral transport (i.e., pure symport of an ion pair (often H^+/Cl^-) where the transport of the anion and cation cannot be separated and there is no movement of net charge). We have previously shown that by studying the anion transport activity of an anionophore in the presence of valinomycin (an electrogenic K^+ transporter) or monensin (an electroneutral M^+/H^+ symporter), the mechanism of anion transport can be elucidated.[12]

Unilamellar POPC vesicles containing 300 mM KCl buffered to pH 7.2 with 5 mM phosphate buffer, prepared as described in Section S3.1, were suspended in the external medium consisting of a 300 mM potassium gluconate solution buffered to pH 7.2 with 5 mM phosphate buffer. The lipid concentration per sample was 1 mM. A DMSO solution of the carrier molecule was added to start the experiment, and the chloride efflux was monitored using a chloride sensitive electrode. At 5 min, the vesicles were lysed with 50 μL of octaethylene glycol monododecyl ether (0.232 mM in 7:1 water:DMSO v/v) and a final chloride reading was taken at 7 min. The electrode readings were converted to chloride concentrations using a standard calibration and subsequently converted to percentages. The results for **A2**, **B2**, **C2**, **C3**, **D2** and **D3** have been previously reported.[2] The results for **A1**, **A3**, **B1**, **B3**, **C1** and **D1** are given in Figure S24. Table S5 also provides an overview for the initial rate of Cl^- transport (k_{ini}) observed under each condition. These k_{ini} values were calculated by fitting the obtained chloride efflux with the asymptotic function $y = a - b \cdot c^x$ using Origin 9.1, where y is the chloride efflux (%), x is time (s) and k_{ini} is then given by $k_{ini} = -b \cdot ln(c)$ (obtained in % s^{-1}), or by fitting the initial linear range of the obtained chloride efflux to $y = a + b \cdot x$, where y is the chloride efflux (%), x is time (s) and k_{ini} is given by the slope b. In case of a sigmoidal time dependence, the first two or three datapoints were omitted from the fit. In order to obtain standard deviations on the initial rate of transport, the fits were performed for each individual repeat and subsequently averaged.

The large and relatively polar gluconate anion should be hard to transport across a lipid bilayer. It is thus assumed that no transport will occur in the presence of the squaramides under these conditions, because a membrane potential will build up in the case of an electrogenic Cl^- carrier or a pH gradient in the case of a H^+/Cl^- symporter or a Cl^-/OH^- antiporter. However, the addition of valinomycin can dissipate the membrane potential created by electrogenic Cl^- transport through electrogenic K^+ transport, while the addition of monensin can dissipate the pH gradient accumulated by Cl^-/OH^- antiport (or H^+/Cl^- symport) through K^+/H^+ antiport. Figure S24 and Table S5 show that

the **A**-series and **B**-series are capable of both electrogenic Cl^- transport (Cl^- efflux observed in the presence of valinomycin) and electroneutral H^+/Cl^- transport (Cl^- efflux observed in the presence of monensin), with the monosquaramide **A**-series being the best transporters. As expected, the **D**-series were not able to transport Cl^- under any conditions. Interestingly, the **C**-series only showed evidence for electroneutral H^+/Cl^- transport (Cl^- efflux observed in the presence of monensin), but not for electrogenic Cl^- transport (no Cl^- efflux observed in the presence of valinomycin). It is possible that the bis-squaramides of the **C**-series are binding strongly to the lipid head group (see also phosphate binding Section S4.4 and modelling sections). This implies that they cannot diffuse through the membrane in their neutral state. This makes anion transport seemingly electroneutral (i.e., they can only perform an anion exchange reaction at the lipid-water interface to mediate transport), because electrogenic chloride transport would result in binding to the head group.

Table S5. Overview of the initial rate of Cl^- transport (k_{ini}) observed during Cl^-/NO_3^- exchange experiments, electrogenic Cl^- transport and electroneutral H^+/Cl^- transport. Errors are between brackets. Numbers highlighted in green represent significant transport rates (k_{ini} > 0.1 % s^{-1}).

k_{ini}	*Cl^-/NO_3^-* [a] (% s^{-1})	*Cl^-/gluconate* [b] (% s^{-1})	*Electrogenic Cl^-* [c] (% s^{-1})	*Electroneutral H^+/Cl^-* [d] (% s^{-1})
Blank[e]	0.005 (±0.003)	0.0013 (±0.0002)	0.0031 (±0.0002)	0.0054 (±0.0008)
A1	**0.17 (±0.01)**	0.007 (±0.004)	**0.19 (±0.01)**	**0.11 (±0.03)**
A2	**2.17 (±0.28)**	0.043 (±0.003)	**0.37 (±0.03)**	**0.71 (±0.03)**
A3	**1.54 (±0.57)**	0.0127 (±0.0008)	**0.49 (±0.05)**	**0.85 (±0.09)**
B1	0.09 (±0.01)	0.006 (±0.001)	0.057 (±0.003)	0.052 (±0.003)
B2	**0.37 (±0.05)**	0.0087 (±0.0009)	**0.22 (±0.01)**	**0.10 (±0.01)**
B3	**0.95 (±0.36)**	0.0185 (±0.0004)	**0.40 (0.05)**	**0.58 (±0.020)**
C1	**0.99 (±0.05)**	0.016 (±0.002)	0.040 (±0.006)	**0.12 (±0.02)**
C2	**0.98 (±0.04)**	0.022 (±0.002)	0.034 (±0.003)	**0.96 (±0.05)**
C3	**0.65 (±0.07)**	0.0119 (±0.0001)	0.043 (±0.008)	**0.64 (±0.07)**
D1	0.044 (±0.009)	0.0071 (±0.001)	0.033 (±0.003)	0.029 (±0.001)
D2	0.0021 (±0.0008)	0.0025	0.0067 (±0.0001)	0.0083 (±0.0001)
D3	0.004 (±0.001)	0.0027	0.007 (±0.001)	0.0082 (±0.0004)

[a] Initial rate of chloride efflux for 1 mol% squaramide to lipid, for Cl^-/NO_3^- exchange experiments described in S3.2. [b] Initial rate of chloride efflux for 1 mol% squaramide to lipid, for potential Cl^-/gluconate exchange calculated as described in S3.9 (no addition of valinomycin or monensin). [c] Initial rate of chloride efflux for 1 mol% squaramide to lipid, for electrogenic Cl^- transport calculated as described in S3.9. (in presence of 0.1 mol% valinomycin). [d] Initial rate of chloride efflux for 1 mol% squaramide to lipid, for electroneutral H^+/Cl^- transport calculated as described in S3.9. (in presence of 0.1 mol% monensin). [e] DMSO only, 0.1 mol% valinomycin only, or 0.1 mol% monensin only.

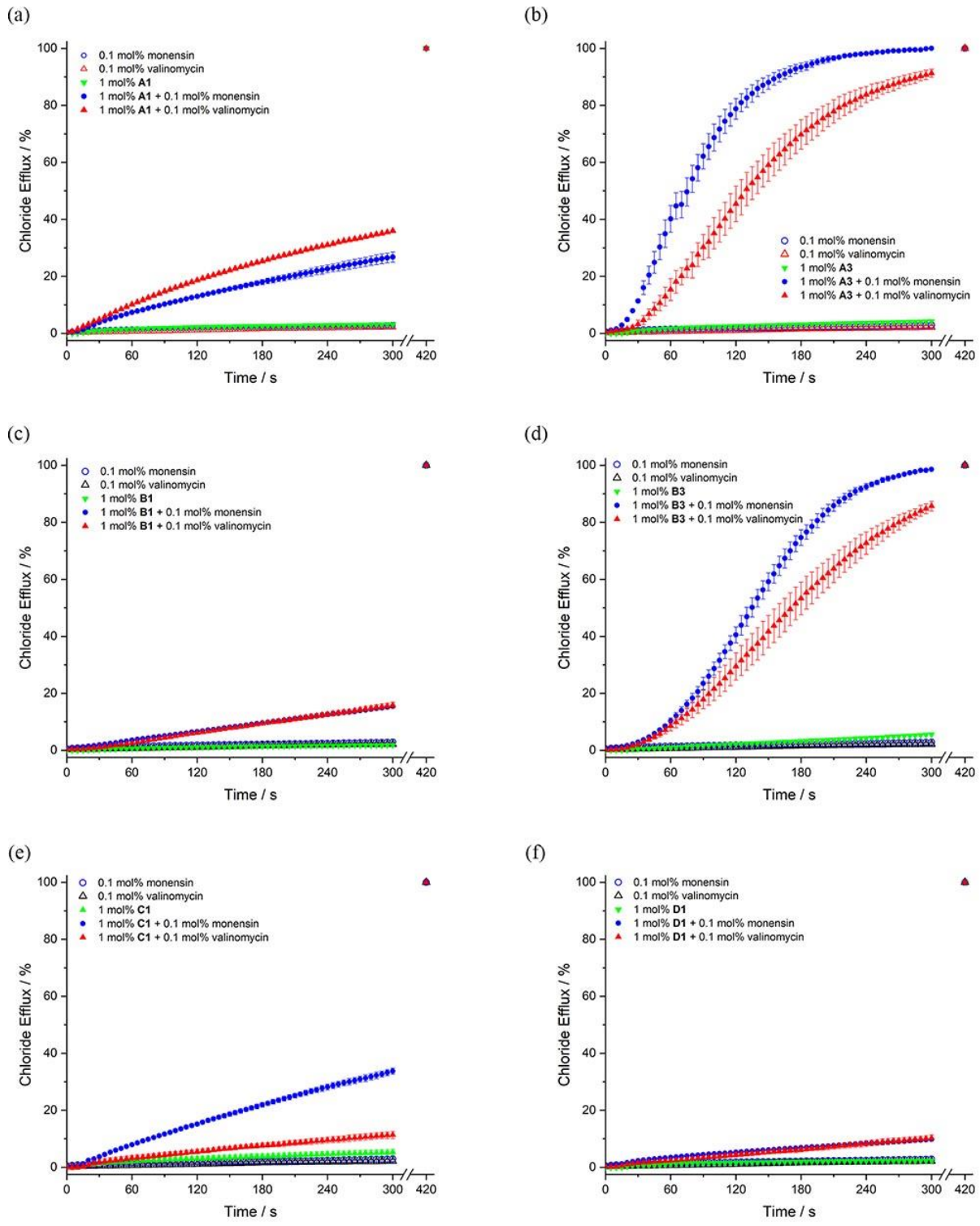

Figure S24. Electrogenic or electroneutral transport mediated by compounds A1-D3 (1 mol% with respect to lipid) in the presence of monensin or valinomycin (0.1 mol% with respect to lipid). Unilamellar POPC vesicles were loaded with 300 mM KCl buffered to pH 7.2 with 5 mM sodium phosphate salts and dispersed in 300 mM potassium gluconate buffered to pH 7.2 with 5 mM sodium phosphate salts. Valinomycin or monensin were added 30 s prior to the start of the experiment, and the squaramides were added at time t = 0 s. At the end of the experiment, detergent was added to lyse the vesicles and calibrate the ISE to 100% chloride efflux. Each point represents the average of a minimum of 3 repeats. DMSO was used as a control. (a) Chloride transport by **A1**. (b) Chloride transport by **A3**. (c) Chloride transport by **B1**. (d) Chloride transport by **B3**. (e) Chloride transport by **C1**. (f) Chloride transport by **D1**.

S3.10. Carrier vs ion channel mechanism

Ion transport can occur either *via* a carrier mechanism (based on diffusion of the ion-transporter complex) or *via* an ion channel mechanism (based on the formation of membrane spanning pores). Compounds **A1-A3**, **B2**, **C2-C3** and **D2-D3** have previously been shown to function as an ion carrier rather than an ion channel.[1, 2, 7] To verify if the same is true for **B1**, **B3**, **C1** and **D1**, calcein assays, U-tubes and cholesterol tests were performed.

Calcein assays

A lipid film of POPC was formed from a chloroform solution under reduced pressure and dried under vacuum for at least 6 hours. The lipid film was rehydrated by vortexing with a NaCl solution (100 mM calcein, 489 mM NaCl, 5 mM phosphate buffer at pH 7.2). The lipid suspension was then subjected to nine freeze-thaw cycles and allowed to age for 30 min at room temperature before extruding 25 times through a 200 nm polycarbonate membrane. The unincorporated calcein was removed by size exclusion chromatography on a Sephadex G-25 column using a sodium sulfate solution as eluent (162 mM Na_2SO_4, 5 mM phosphate buffer at pH 7.2). The thus obtained unilamellar POPC vesicles were suspended in a Na_2SO_4 solution buffered to pH 7.2 with sodium phosphate salts. The lipid concentration per sample was 1 mM. The fluorescence emission of the encapsulated calcein at 520 nm after excitation at 490 nm was recorded using a *Cary Eclipse Fluorescence Spectrophotometer*. At t = 10 s, a solution of the carrier molecule in DMSO was added to start ion transport. At the end of the experiment the vesicles were lysed with 30 µl of octaethylene glycol monododecyl ether (0.232 mM in 7:1 water:DMSO v/v). Calcein is a self-quenching fluorophore[13] and the fractional calcein release (FR) can thus be calculated as follows (with I_t = fluorescence intensity at time t, I_0 = fluorescence intensity at time 0 and I_{max} = fluorescence intensity after addition of detergent):

$$FR = \frac{I_t - I_0}{I_{\max} - I_0}$$

The results depicted in Figure S25 show no sign of calcein release from the vesicles, suggesting that compounds **B1**, **B3**, **C1** and **D1** do not cause the formation of large channels in the POPC membranes through which calcein could diffuse and most likely function as mobile carriers for chloride ions.

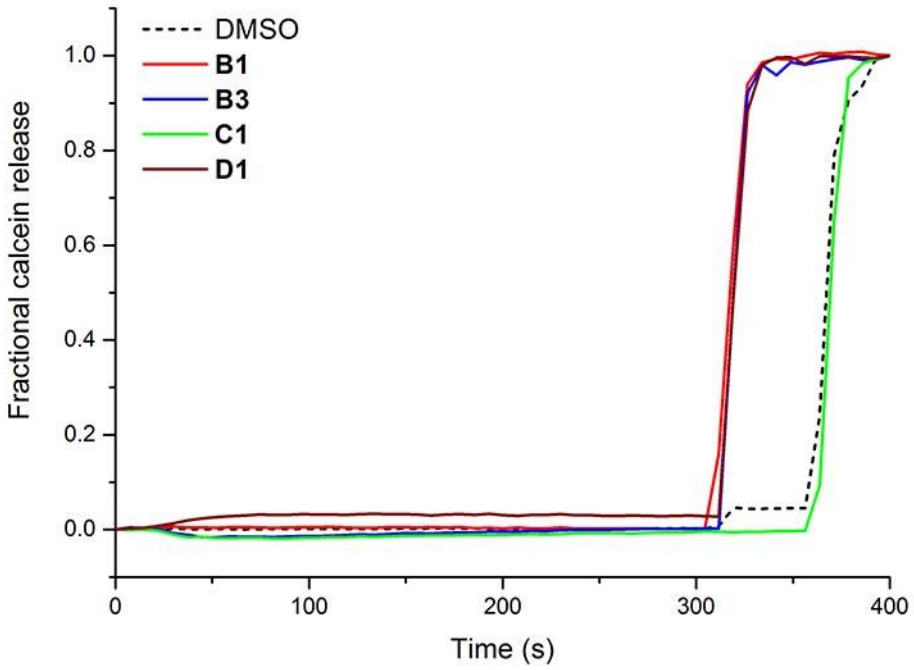

Figure S25. **Calcein leakage by B1, B3, C1 and D1 (4 mol% carrier-to-lipid)**. Unilamellar POPC vesicles were loaded with 100 mM calcein and 489 mM NaCl, buffered to pH 7.2 with 5 mM sodium phosphate salts. The vesicles were dispersed in 162 mM Na_2SO_4 buffered to pH 7.2 with 5 mM sodium phosphate salts. At t = 10 s, a DMSO solution of the transporter was added to start the experiment. At the end of the experiment, detergent was added to lyse the vesicles. The results are shown as the fraction of calcein leaked from the vesicles.

U-tube experiment

In a U-tube experiment the lipid bilayer is substituted with a bulk organic phase separating a donating and receiving aqueous phase in U-shaped glassware. In these conditions ion channel formation is virtually impossible. The organic phase consisted of 15 mL nitrobenzene (for solubility reasons) and contained 1 mM of carrier and 2 mM of $TBA^+PF_6^-$ to provide for counterions during transport. A control experiment was executed with neat nitrobenzene (no carrier) containing 2 mM of $TBA^+PF_6^-$. The same aqueous phases were used as for the vesicle experiments. The donating phase contained 489 mM NaCl and was buffered to pH 7.2 with 5 mM phosphate salts (10 mL). The receiving phase contained 489 mM $NaNO_3$ and was buffered to pH 7.2 with 5 mM phosphate salts (10 mL). The change in chloride concentration of the receiving phase was monitored with a chloride-selective electrode and the electrode was calibrated to convert the potential readings (mV) to chloride concentrations (mM). The experiments were conducted at room temperature and the results are shown in Figure S26. Figure S26 shows that the ability to transport chloride through a bulk organic phase in a U-tube experiment can be correlated to the ability to transport chloride through a lipid bilayer (represented by the initial rate of chloride transport k_{ini} – Table S3). Roughly the same trend in activity was observed in both U-tube and vesicle experiments. Some of the squaramides (partly) precipitated

out of the nitrobenzene solution during the course of the experiment, which can explain some of the low transport rates seen during the U-tube experiments.

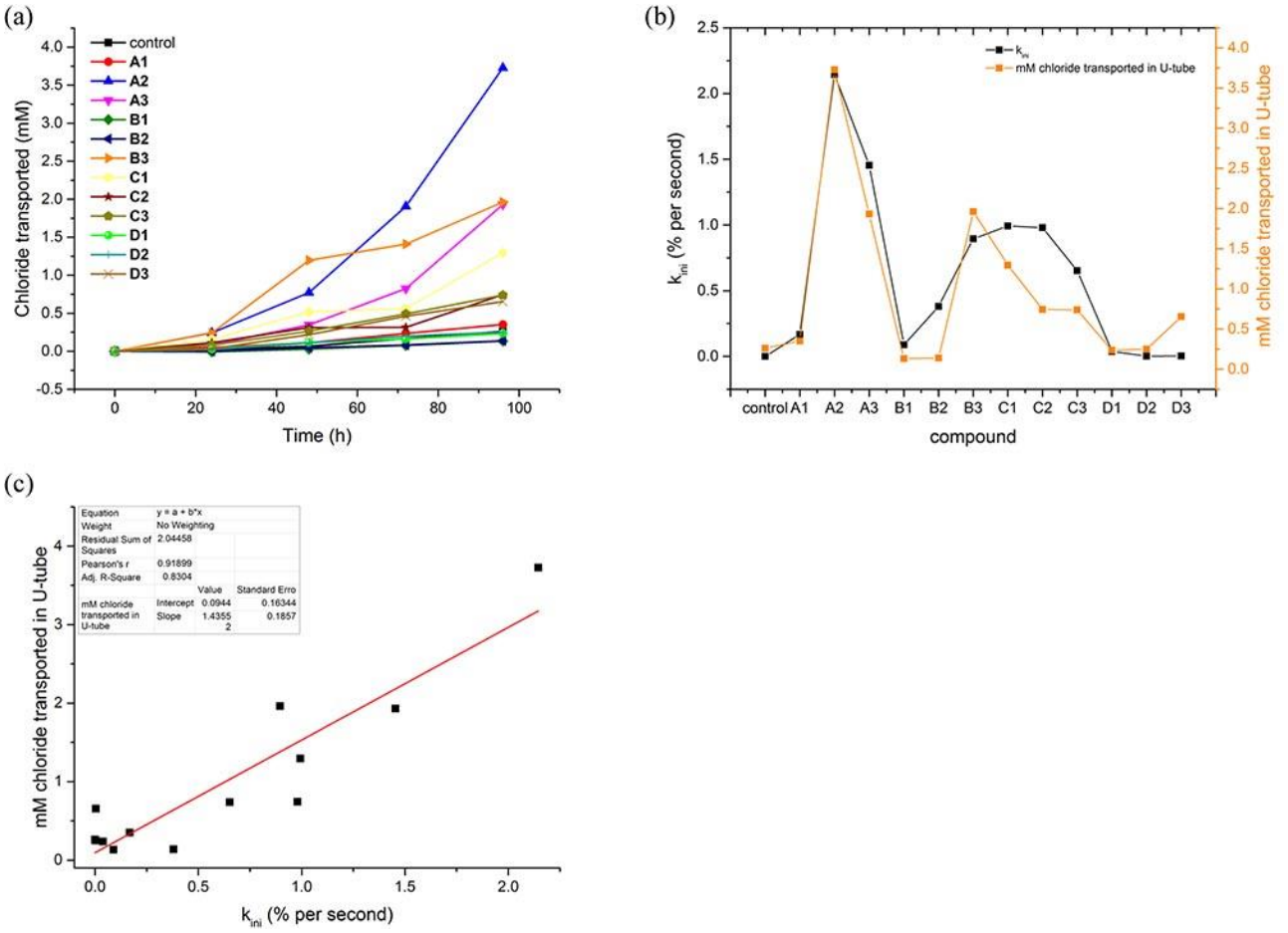

Figure S26. **U-tube experiment in nitrobenzene.** (a) Change in chloride concentration in the receiving phase over time for all squaramides **A1-D3** and a control experiment. (b) Graph showing the change in the chloride concentration of the receiving aqueous phase after 4 days (orange line) and the k_{ini} values for the chloride/nitrate vesicle studies (black line) for all squaramides **A1-D3** and a control experiment. (c) Correlation between the amount of chloride transport during U-tube experiments and the kini values. The red line represents a linear fit ($R^2 = 0.83$).

Cholesterol test

Vesicles were prepared in the same way as described above (see section S3.1-S3.2), but the lipid consisted of a 7:3 molar mixture of POPC and cholesterol. Cholesterol is believed to increase the viscosity of the membrane, hence slowing down diffusion in the lipid bilayer, although it also has a number of other effects on the membrane.[14, 15] This slowing down should be more pronounced in the case of a mobile carrier mechanism, while no change in anion transport rate is expected for an ion channel. The results for compounds **A1-A3** and **B2**, **C2**, **C3**, **D2**, **D3** have been previously reported and were inconsistent.[2, 16] For novel compounds **B1**, **B3**, **C1** and **D1** (Figure S27) a decrease in anion transport is observed in cholesterol containing vesicles, consistent with a mobile carrier mechanism.

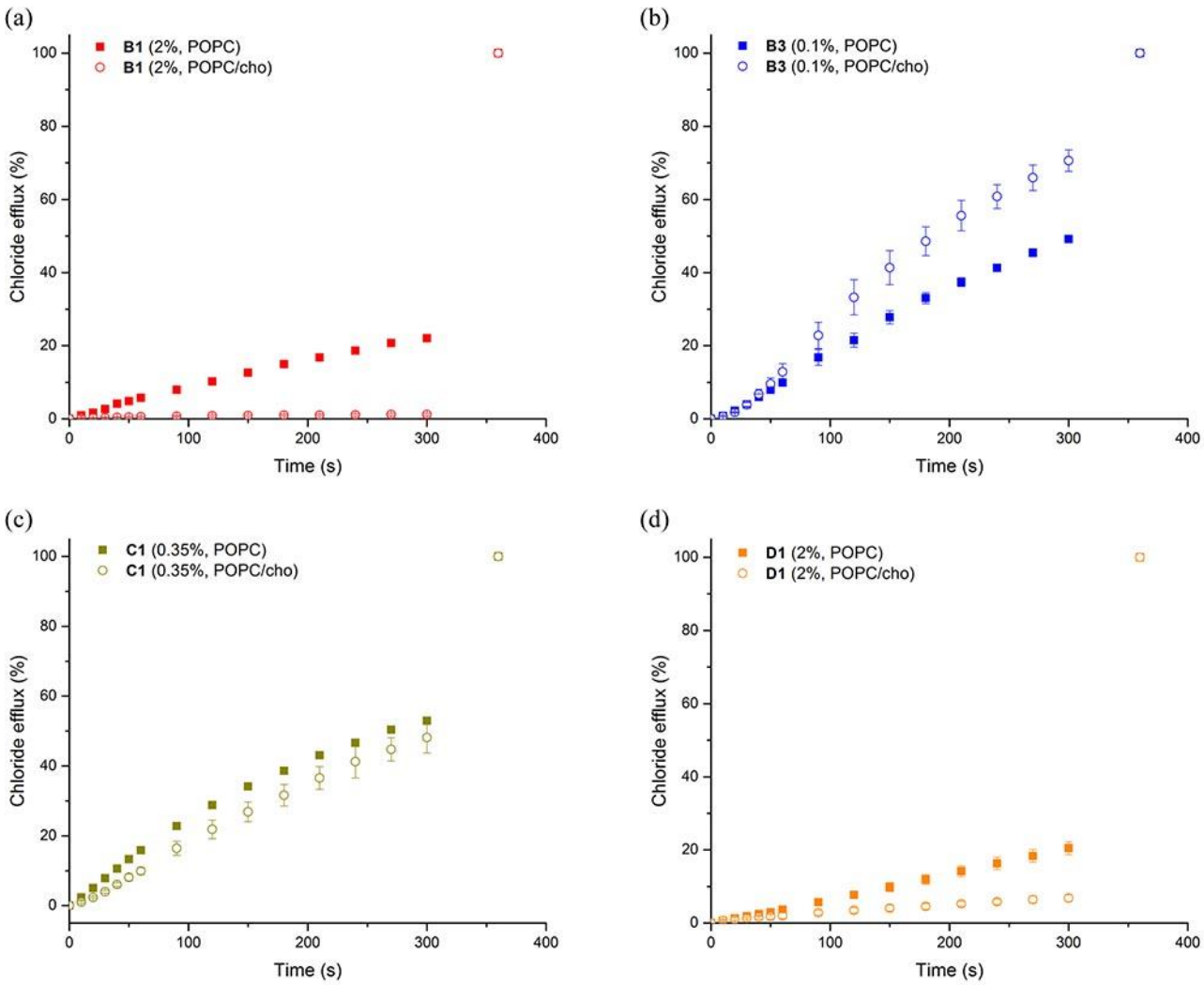

Figure S27. **Cholesterol test for mobile carrier mechanism.** Chloride efflux promoted by compounds **B1, B3, C1** and **D1** from unilamellar POPC vesicles (filled symbols) or unilamellar 7:3 POPC:cholesterol vesicles (empty symbols) loaded with 489 mM NaCl buffered to pH 7.2 with 5 mM sodium phosphate salts. The vesicles were dispersed in 489 mM $NaNO_3$ buffered to pH 7.2 with 5 mM sodium phosphate salts. At the end of the experiment, detergent was added to lyse the vesicles and calibrate the ISE to 100% chloride efflux. Each point represents the average of three trials. (a) 2 mol% of compound **B1**. (b) 0.1 mol% of compound **B3**. (c) 0.35 mol% of compound **C1**. (d) 2 mol% of compound **D1**.

S4. NMR SPECTROSCOPIC BINDING STUDIES

NMR spectroscopic titrations were performed by additions of aliquots of the anionic guest as the tetrabutylammonium (TBA) or tetraethylammonium (TEA) salt (0.15 M), in a solution of the receptor (0.01 M) in DMSO-d_6/0.5% H_2O, to a 0.01 M solution of the receptor in DMSO-d_6/0.5% H_2O. In total 20 data points were collected, corresponding to a maximum of approximately 6-7 equivalents of guest. Both salt and receptor were dried under high vacuum prior to use. ^{1}H NMR spectra were recorded on a Bruker AV300 or AV400 spectrometer and calibrated to the residual protio solvent peak in DMSO-d_6 (δ = 2.50 ppm). Stack plots were made using ACD Labs 1D NMR Processor. Where possible, the global-analysis online tool BindFit[17] was used to simultaneously curve-fit the data of all protons shifting more than 0.1 ppm over the course of the titration and to obtain association constants K_a. Usually a 1:1 model was used first, but in the case where the residual plots indicated a different stoichiometry, 1:2 or 2:1 host:guest models were used for curve-fitting (flavour: none, method: Nelder-Mead). While mono-squaramides **A1-A3** and **B1** display 1:1 host:guest stoichiometry, **B2** and **B3** display 2:1 host:guest stoichiometry with little cooperativity (α = 1.1-1.5). The multitopic bis- and tris-squaramides **C1-C3** and **D1-D3** display 1:2 (and possibly 1:3) host:guest stoichiometries with little or negative cooperativity (α < 1); therefore, the host:guest complex speciation (1:1 *vs* 1:2) in solution will compose a higher fraction of 1:1 complex. In general, similar changes are observed upon the addition of $TEAHCO_3$ and TBAOH to the DMSO solution of the squaramides, suggesting that the squaramides are deprotonated by HCO_3^-.

The association constants for **A2**, **B2**, **C2**, **C3**, **D2** and **D3** with TBA chloride, TBA nitrate, TEA bicarbonate, TBA dihydrogen-phosphate and TBA sulfate have been published elsewhere.[2] The binding constants for compounds **A1** and **A3** with TBA chloride, TBA nitrate and TEA bicarbonate have also been previously reported,[16] but were recalculated using the new global-analysis online tool BindFit. An overview of the new and previously published association constants is given in Table S6. Figure S28 to Figure S48 show the stack plots and fit plots of the previously unpublished anion binding studies of **A1**, **A3**, **B1**, **B3**, **C1** and **D1**. For the stack plots and fitplots of anion binding studies regarding **B2**, **C2**, **C3**, **D2** and **D3** the reader is referred to our previous publications.[2, 7, 16]

Table S6. Overview of association constants (M^{-1}) of TBA salts to compounds **A1-D3** in DMSO-d_6 containing 0.5 % water at 298 K.

	Cl^-	NO_3^-	HCO_3^-[a]	$H_2PO_4^-$	SO_4^{2-}
A1	K_{11} = 240	-[b]	Deprotonation[c]	-[d]	K_{11} = 4593
A2[e]	K_{11} = 433	-[b]	Deprotonation[c]	-[d]	-[d]
A3	K_{11} = 602	-[b]	Deprotonation[c]	-[d]	-[d]
B1	K_{11} = 119	-[b]	K_{11} = 1355	K_{11} = 3968	-[d]
B2[e]	K_{11} = 729 K_{21} = 203 (α = 1.11)[f]	-[b]	Deprotonation[c]	K_{11} = 5464 K_{21} = 25.4 (α = 0.019)[f]	K_{11} = 5823
B3	K_{11} = 776 K_{21} = 275 (α = 1.42)[f]	-[b]	Deprotonation[c]	-[d]	-[d]
C1	K_{11} = 871 K_{21} = 331 (α = 1.52)[f]	-[b]	Deprotonation[c]	$K_{11} > 10^4$ K_{12} = 43.9 (α < 0.005)[f]	$K_{11} > 10^4$ K_{21} = 1270 (α < 0.005)[f]
C2[e]	K_{11} = 4742 K_{12} = 29.1 (α = 0.0025)[f]	-[b]	Deprotonation[c]	K_{11} = 430 K_{12} = 86.5 (α = 0.80)[f]	-[d]
C3[e]	K_{11} = 2259 K_{12} = 61.8 (α = 0.11)[f]	-[b]	Deprotonation[c]	$K_{11} > 10^4$ K_{12} = 317 (α < 0.13)[f]	-[d]
D1	K_{11} = 821 K_{12} = 26.4 (α = 0.13)[f]	-[b]	Deprotonation[c]	(K_{11} = 13.2)[g] (K_{12} = 307)[g]	-[d]
D2[e]	K_{11} = 8021 K_{12} = 19.6 (α = 0.0049)[f]	-[b]	Deprotonation[c]	(K_{11} = 40.7)[g] (K_{12} = 2788)[g]	-[d]
D3[e]	K_{11} = 1627 K_{12} = 67.0 (α = 0.16)[e]	-[b]	Deprotonation[c]	(K_{11} < 10)[g] ($K_{12} > 10^4$)[g]	-[d]

[a] Added as TEA salt. [b] No change in chemical shift of any proton, presumable very weak (or no) binding. [c] Comparison with titration with TBA hydroxide suggests that the ligand is deprotonated by bicarbonate. [d] Data could not be fitted. [e] Values taken from reference 2. [f] The interaction parameter $\alpha = 4K_{12}/K_{11}$ (or $= 4K_{21}/K_{11}$) with $\alpha > 1$ indicating positive cooperativity, $\alpha < 1$ negative cooperativity, and $\alpha \approx 1$ no cooperativity. [g] Presumably deprotonation of bound H_2PO_4 competes with binding.

S4.1. NMR spectroscopic titrations with TBA chloride

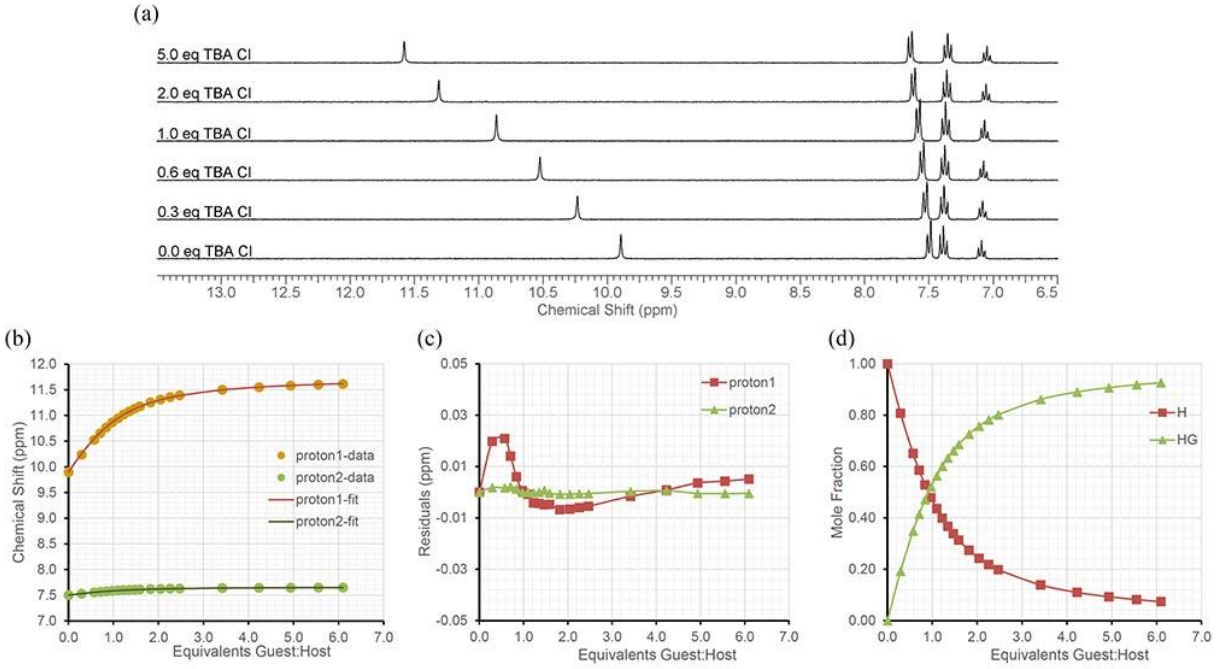

Figure S28. ^{1}H NMR spectroscopic titration of compound A1 with TBACl in DMSO-*d*$_6$ with 0.5% water at 298 K. (a) Stack plot. (b) Fitplot for NH proton at δ = 9.90 ppm (proton1) and CH proton at δ = 7.50 ppm (proton2) using global analysis with 1:1 host:guest stoichiometry. K_a = 240 M^{-1} (error 1%). (c) Plot of the residuals for δ = 9.90 ppm (proton1) and δ = 7.50 ppm (proton2) using global analysis. (d) Calculated mole fractions. The change in chemical shift for δ = 7.39 (|Δδ| < 0.04 ppm) ppm and δ = 7.09 ppm (|Δδ|< 0.05 ppm) was too small to be included in the analysis.

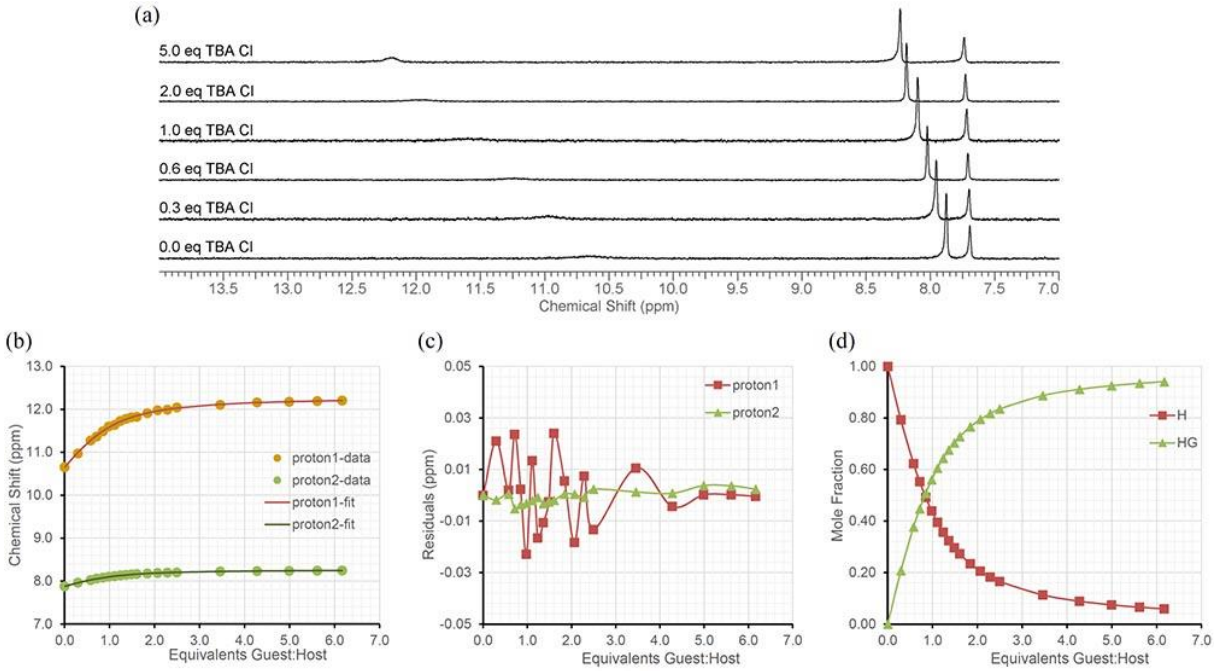

Figure S29. ^{1}H NMR spectroscopic titration of compound A3 with TBACl in DMSO-*d*$_6$ with 0.5% water at 298 K. (a) Stack plot. (b) Fitplot for NH proton at δ = 10.65 ppm (proton1) and CH proton at δ = 7.88 ppm (proton2) using global analysis with 1:1 host:guest stoichiometry. K_a = 602 M^{-1} (error 2%). (c) Plot of the residuals for δ = 10.65 ppm (proton1) and δ = 7.88 ppm (proton2) using global analysis. (d) Calculated mole fractions. The change in chemical shift for CH proton at δ = 7.69 ppm (|Δδ|< 0.05 ppm) was too small to be included in the analysis.

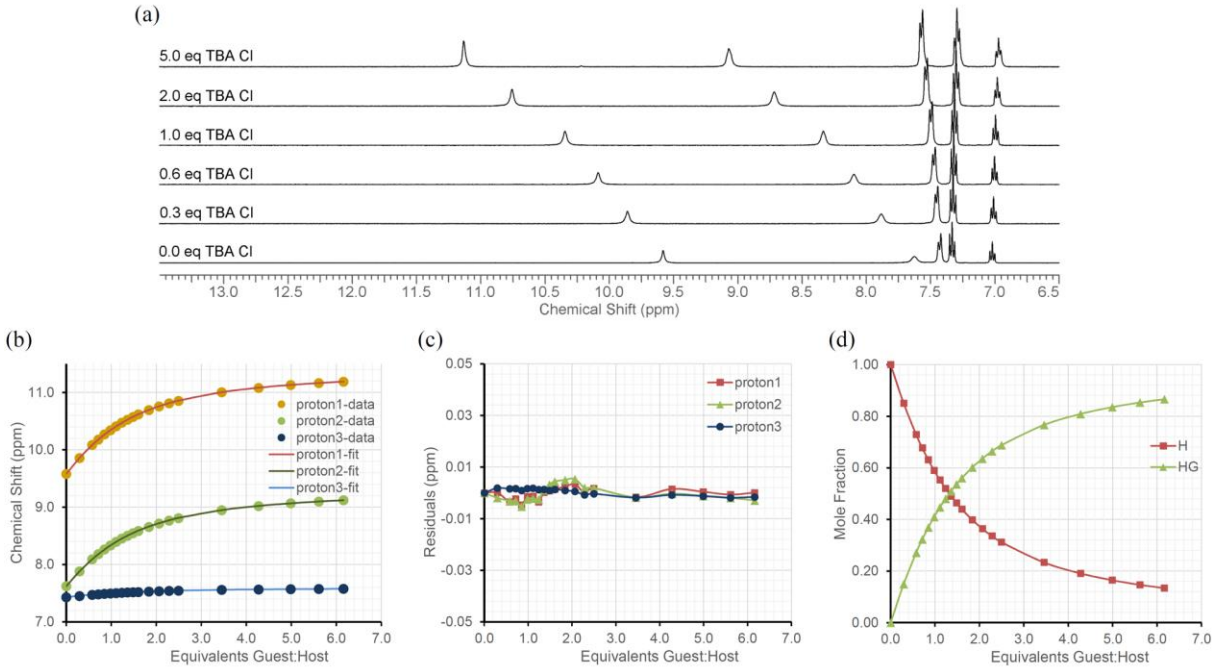

Figure S30. ^{1}H NMR spectroscopic titration of compound B1 with TBACl in DMSO-d_6 with 0.5% water at 298 K. (a) Stack plot. (b) Fitplot for NH proton at δ = 9.58 ppm (proton1), NH proton at δ = 7.62 ppm (proton2) and CH proton at δ = 7.43 ppm (proton3) using global analysis with 1:1 host:guest stoichiometry. K_a = 119 M^{-1} (error 0.25%). (c) Plot of the residuals for δ = 9.58 ppm (proton1), δ = 7.62 ppm (proton2) and δ = 7.43 ppm (proton3) using global analysis. (d) Calculated mole fractions. The change in chemical shift for CH protons at δ = 7.33 ppm (|Δδ|< 0.04 ppm) and at δ = 7.02 ppm (|Δδ|< 0.05 ppm) was too small to be included in the analysis

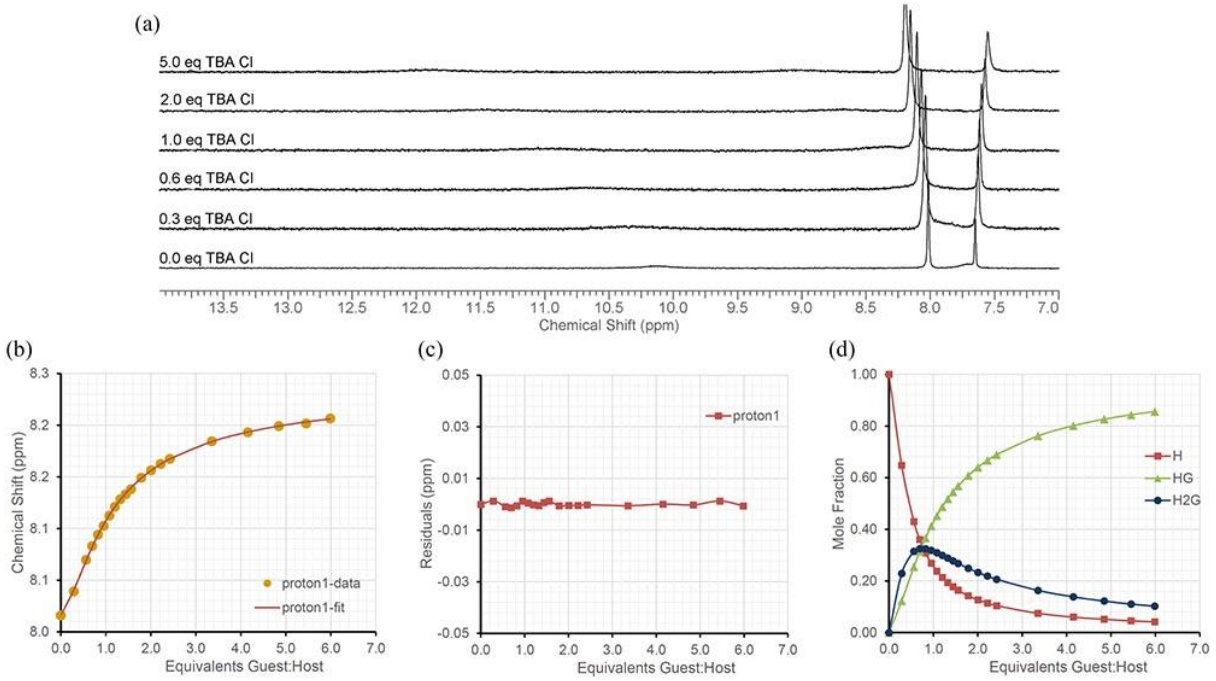

Figure S31. ^{1}H NMR spectroscopic titration of compound B3 with TBACl in DMSO-d_6 with 0.5% water at 298 K. (a) Stack plot. (b) Fitplot for CH proton at δ = 8.01 ppm (proton1) using global analysis with 2:1 host:guest stoichiometry. K_{11} = 776 M^{-1} (error 11%), K_{21} = 275 M^{-1} (error 15%). (c) Plot of the residuals for δ = 8.01 ppm (proton1) using global analysis. (d) Calculated mole fractions. The change in chemical shift for CH proton at δ = 7.65 ppm (|Δδ|= 0.1 ppm) was too small to be included in the analysis, while the NH protons at δ = 10.11 ppm and δ = 7.72 ppm broadened too much to allow accurate analysis.

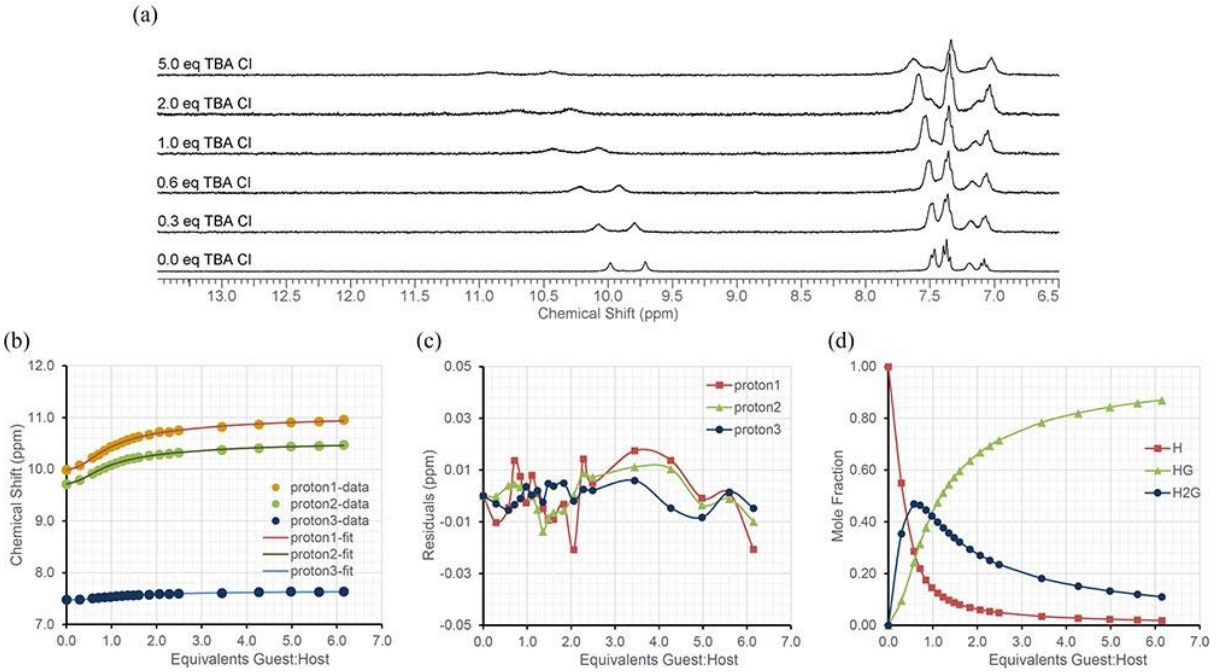

Figure S32. ^{1}H NMR spectroscopic titration of compound C1 with TBACl in DMSO-d_6 with 0.5% water at 298 K. (a) Stack plot. (b) Fitplot for NH protons at δ = 9.98 ppm (proton1) and at δ = 9.71 ppm (proton2), and CH proton at δ = 7.48 ppm (proton3) using global analysis with 2:1 host:guest stoichiometry. K_{11} = 871 M^{-1} (error 13%), K_{21} = 331 M^{-1} (error 15%). (c) Plot of the residuals for δ = 9.98 ppm (proton1), δ = 9.71 ppm (proton2) and δ = 7.48 ppm (proton3) using global analysis. (d) Calculated mole fractions. The change in chemical shift for the remaining CH protons displayed too much overlap to allow accurate analysis.

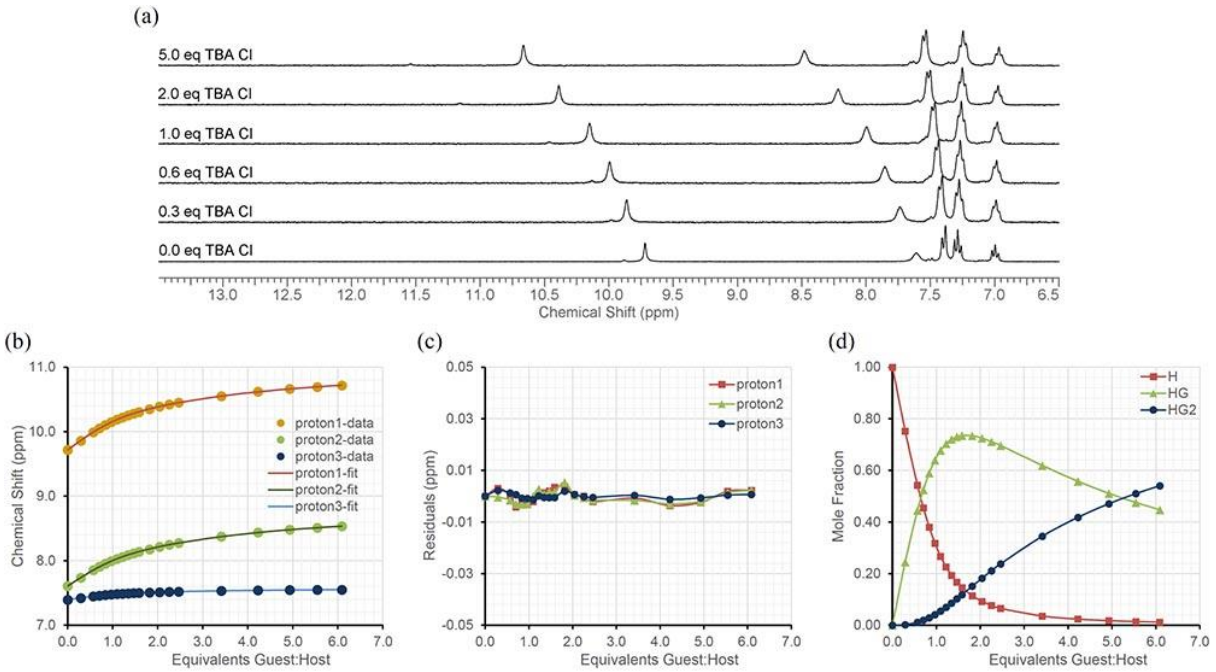

Figure S33. ^{1}H NMR spectroscopic titration of compound D1 with TBACl in DMSO-d_6 with 0.5% water at 298 K. (a) Stack plot. (b) Fitplot for NH protons at δ = 9.72 ppm (proton1) and at δ = 7.61 ppm (proton2), and CH proton at δ = 7.39 ppm (proton3) using global analysis with 1:2 host:guest stoichiometry. K_{11} = 821 M^{-1} (error 2%), K_{12} = 26.4 M^{-1} (error 0.76%). (c) Plot of the residuals for δ = 9.72 ppm (proton1), δ = 7.61 ppm (proton2) and δ = 7.39 ppm (proton3) using global analysis. (d) Calculated mole fractions. The change in chemical shift for CH protons at δ = 7.29 ppm (|Δδ| < 0.04 ppm) and at δ = 7.00 ppm (|Δδ| < 0.03 ppm) was too small to be included in the analysis.

S4.2. NMR spectroscopic titrations with TBA nitrate

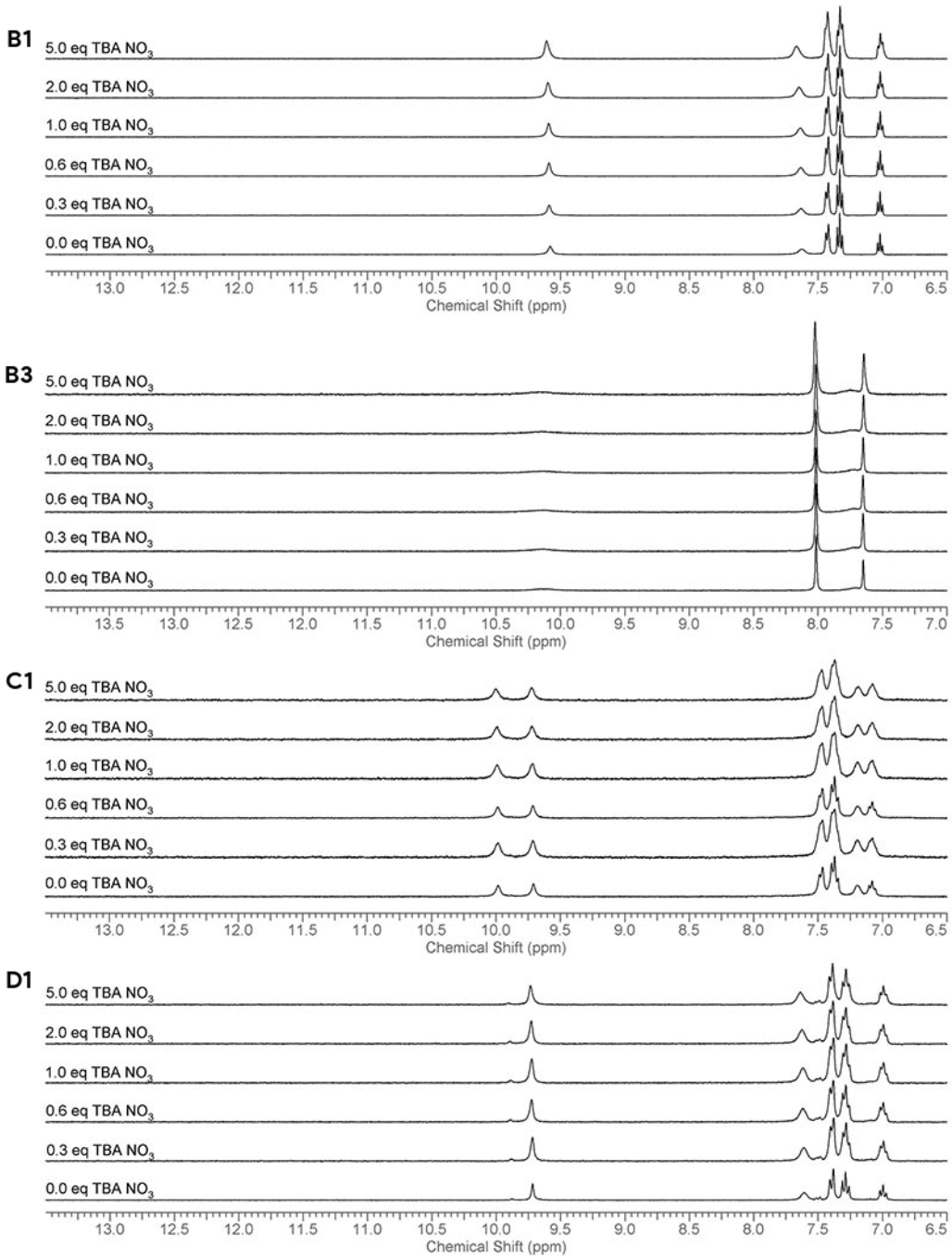

Figure S34. Stack plot of the ^{1}H NMR spectroscopic titration of B1, B3, C1 and D1 with $TBANO_3$ in DMSO-*d_6* with 0.5% water at 298 K. The change in chemical shift for all protons (**B1**: $|\Delta\delta| < 0.06$ ppm; **B3**: $|\Delta\delta| < 0.04$ ppm; **C1**: $|\Delta\delta| < 0.02$ ppm; and **D1**: $|\Delta\delta| < 0.04$ ppm) was too small to conduct any global analysis. Presumably these compounds do not bind nitrate in these conditions.

S4.3. NMR spectroscopic titrations with TEA bicarbonate

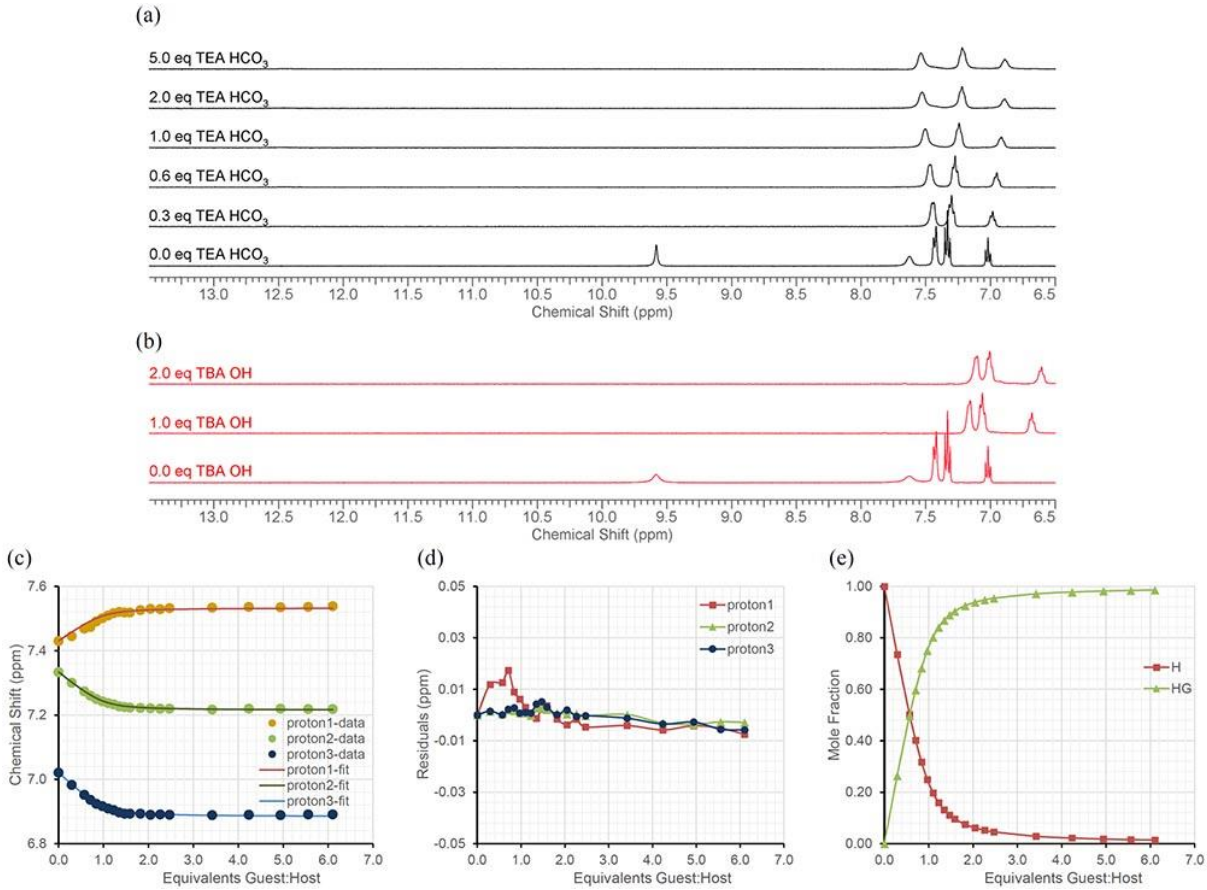

Figure S35. ^{1}H NMR spectroscopic titration of compound B1 with TEAHCO$_3$ and TBAOH in DMSO-*d*$_6$ with 0.5% water at 298 K. The CH proton at δ = 7.43 ppm moves downfield in the presence of TEA HCO_3 and upfield in the presence of TBA OH. Deprotonation of the receptor by TEA HCO_3 is therefore unlikely and anion complex formation is expected. (a) Stack plot for TEAHCO$_3$. (b) Stack plot for TBAOH. (b) Fitplot for CH protons at δ = 7.43 ppm (proton1), δ = 7.33 ppm (proton2) and δ = 7.02 ppm (proton3) using global analysis with 1:1 host:guest stoichiometry. K_a = 1355 M^{-1} (error 15%). (c) Plot of the residuals for δ = 7.43 ppm (proton1), δ = 7.33 ppm (proton2) and δ = 7.02 ppm (proton3) using global analysis. (d) Calculated mole fractions. The NH signals broadened too much to be included in the analysis.

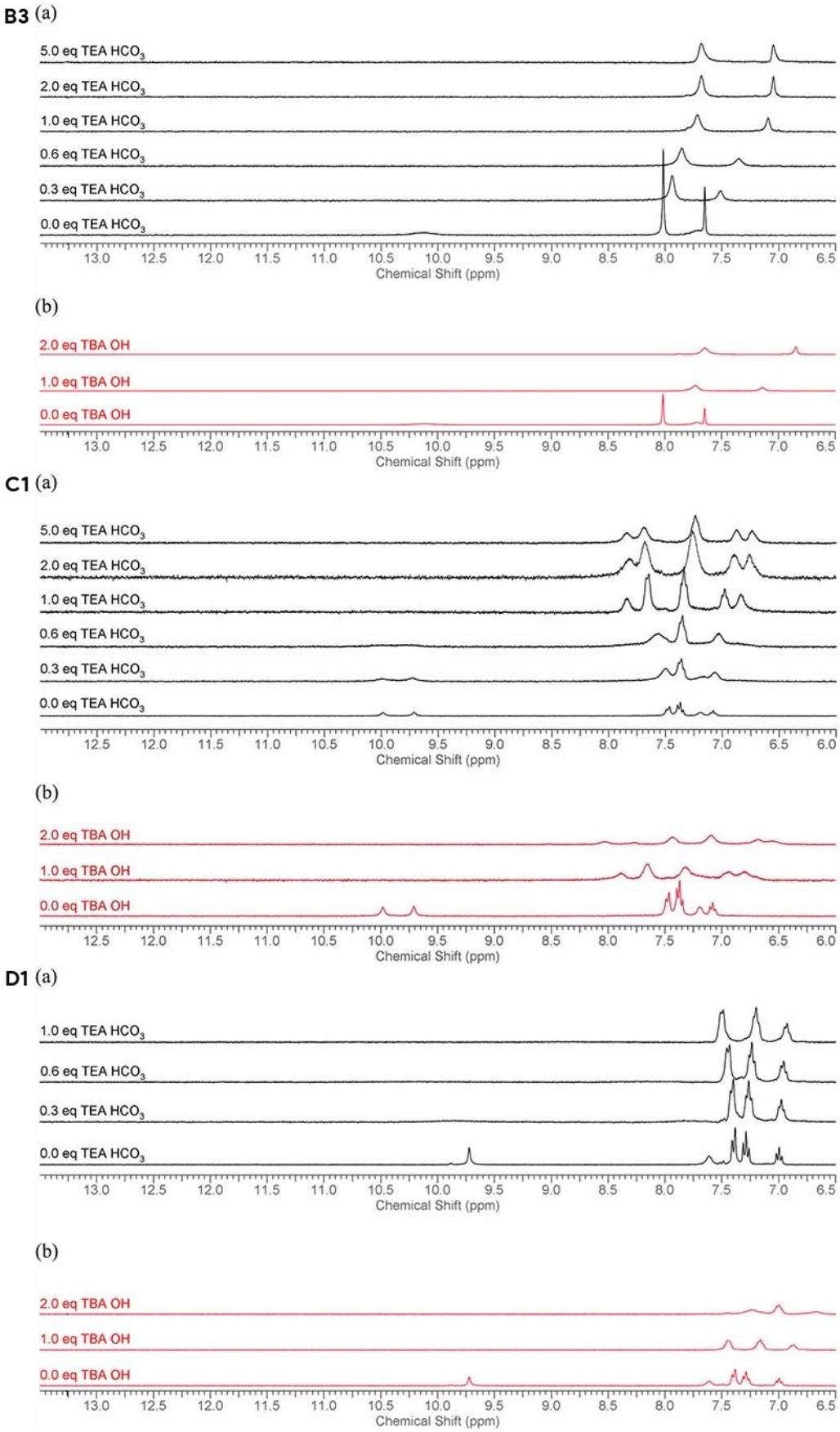

Figure S36. Comparison of the ^{1}H NMR spectroscopic titration of compound B3, C1 and D1 with $TEAHCO_3$ and TBAOH in DMSO-*d*$_6$ with 0.5% water at 298 K. Similar up/downfield shifts are seen in both titrations (up to one equivalent), suggesting deprotonation rather than complexation of bicarbonate. (a) Stack plot for $TEAHCO_3$. (b) Stack plot for TBAOH.

S4.4. NMR spectroscopic titrations with TBA phosphate

The titrations of the squaramides with $TBAH_2PO_4$ were not ideal and in many cases the titration data could not be fitted to a 1:1, 1:2 or 2:1 host:guest model. It has been observed before that strongly hydrogen bonding receptors can deprotonate bound $H_2PO_4^-$ and subsequently bind HPO_4^{2-}. [10, 18] It is likely that these deprotonation effects are the reasons for the non-ideal binding observed for the squaramides. Other explanations could be the existence of complex mixtures of stoichiometries. Similar effects were also seen for the titrations with $(TBA)_2SO_4$ (see Section S4.5.), indicating that complex stoichiometries might also play a role in the binding of the squaramides to sulfate anions.

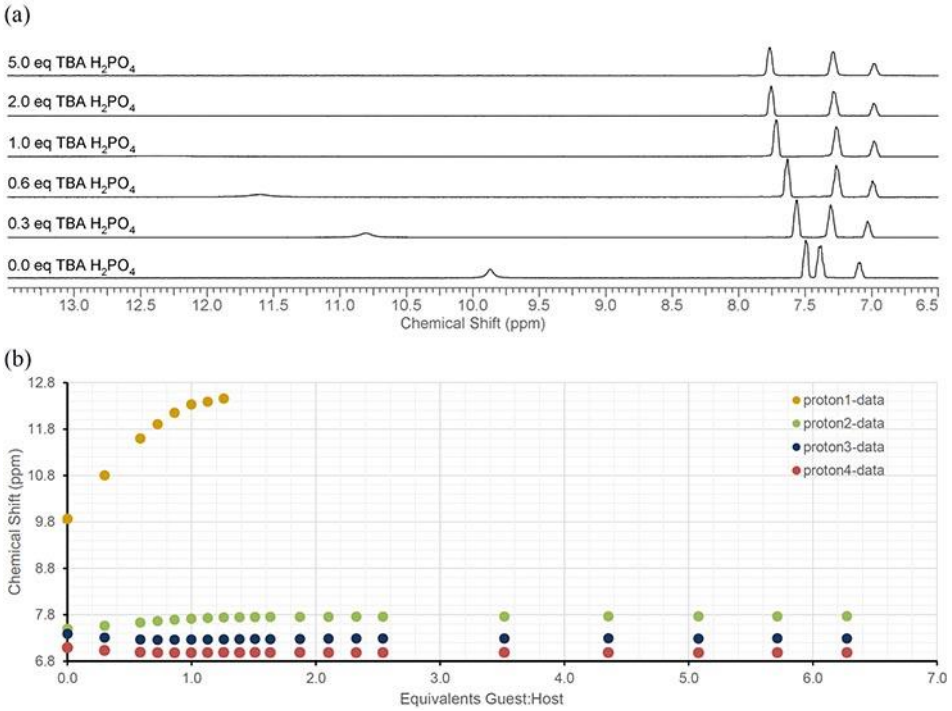

Figure S37. ^{1}H NMR spectroscopic titration of compound A1 with $TBAH_2PO_4$ in DMSO-d_6 with 0.5% water at 298 K. (a) Stack plot. (b) Change in chemical shift for NH proton at δ = 9.87 ppm (proton1), CH proton at δ = 7.50 ppm (proton2), CH proton at δ = 7.39 ppm (proton3) and CH proton at δ = 7.09 ppm (proton4). The data could not be fitted to any model. Possible deprotonation effects or complex stoichiometries might complicate the equilibria.

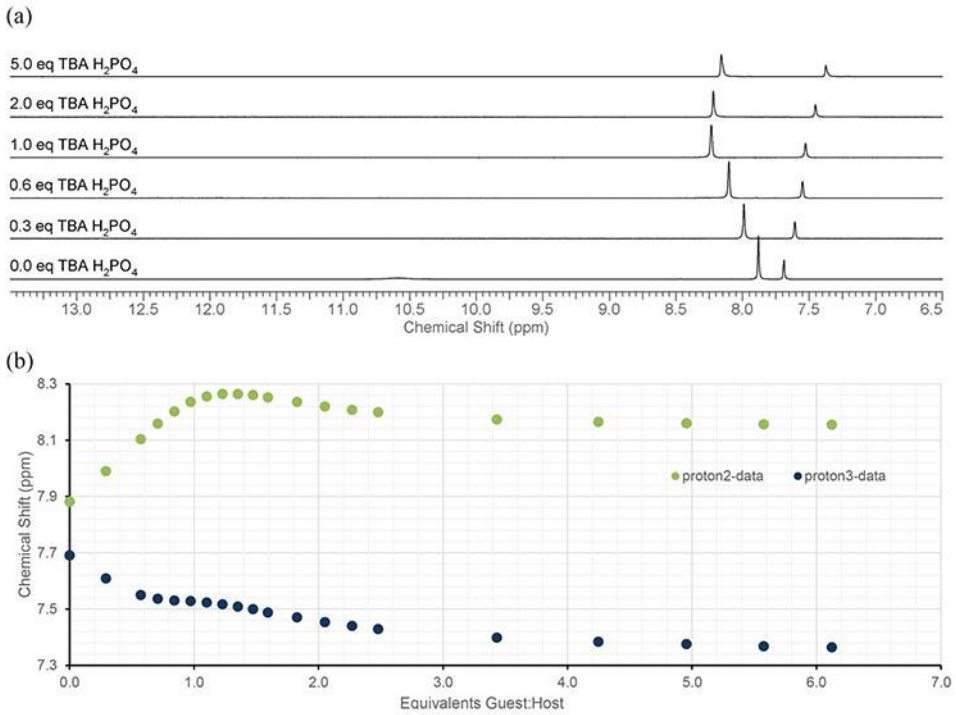

Figure S38. ^{1}H NMR spectroscopic titration of compound A3 with $TBAH_2PO_4$ in DMSO-*d*$_6$ with 0.5% water at 298 K. (a) Stack plot. (b) Change in chemical shift for CH proton at δ = 7.88 ppm (proton2) and CH proton at δ = 7.69 ppm (proton3). NH proton at δ = 10.58 ppm (proton1) broadened too much upon the addition of anion. The data could not be fitted to any model. Possible deprotonation effects or complex stoichiometries might complicate the equilibria.

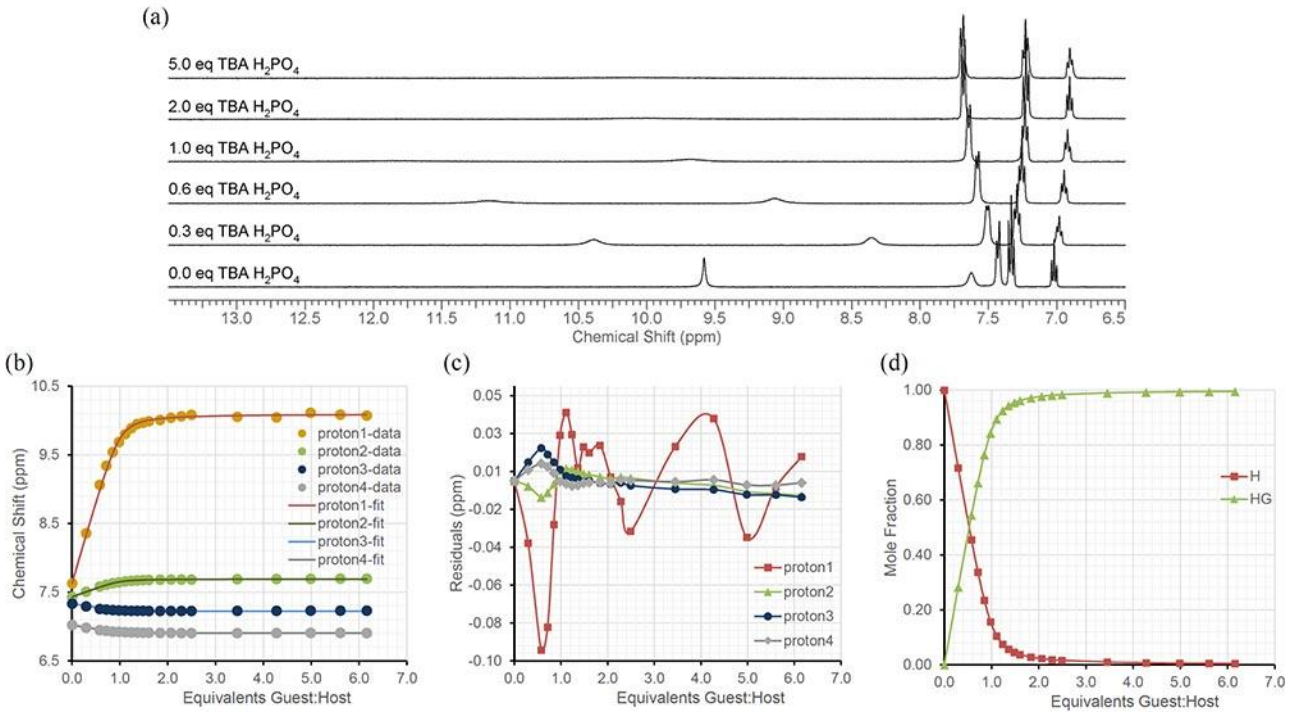

Figure S39. ^{1}H NMR spectroscopic titration of compound B1 with TBAH$_2$PO$_4$ in DMSO-*d*$_6$ with 0.5% water at 298 K. (a) Stack plot. (b) Fitplot for NH proton at δ = 7.62 ppm (proton1) and CH protons at δ = 7.43 ppm (proton2), δ = 7.33 ppm (proton3), and δ = 7.02 ppm (proton4) using global analysis with 1:1 host:guest stoichiometry. K_a = 3968 M^{-1} (error 9%). (c) Plot of the residuals for 7.62 ppm (proton1), δ = 7.43 ppm (proton2), δ = 7.33 ppm (proton3), and δ = 7.02 ppm (proton4) using global analysis. (d) Calculated mole fractions. The NH proton at δ = 9.58 ppm broadened too much for accurate analysis

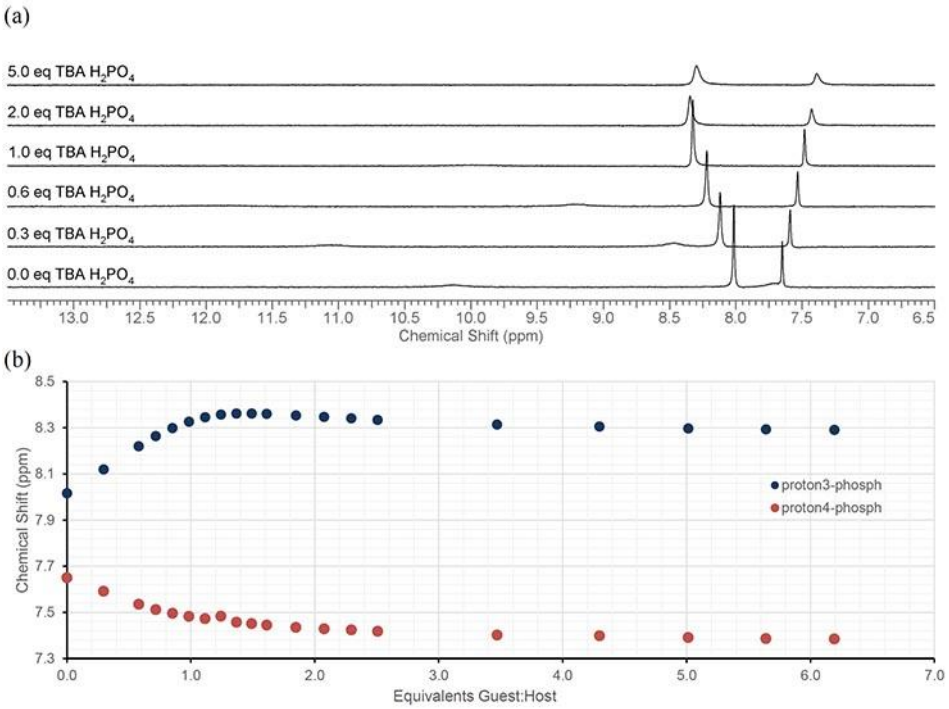

Figure S40. ^{1}H NMR spectroscopic titration of compound B3 with TBAH$_2$PO$_4$ in DMSO-*d*$_6$ with 0.5% water at 298 K. (a) Stack plot. (b) Change in chemical shift for CH proton at δ = 8.02 ppm (proton3) and CH proton at δ = 7.65 ppm (proton4). NH protons at δ = 10.13 ppm (proton1) and δ = 7.71 ppm (proton2) broadened too much upon the addition of anion. The data could not be fitted to any model. Possible deprotonation effects or complex stoichiometries might complicate the equilibria.

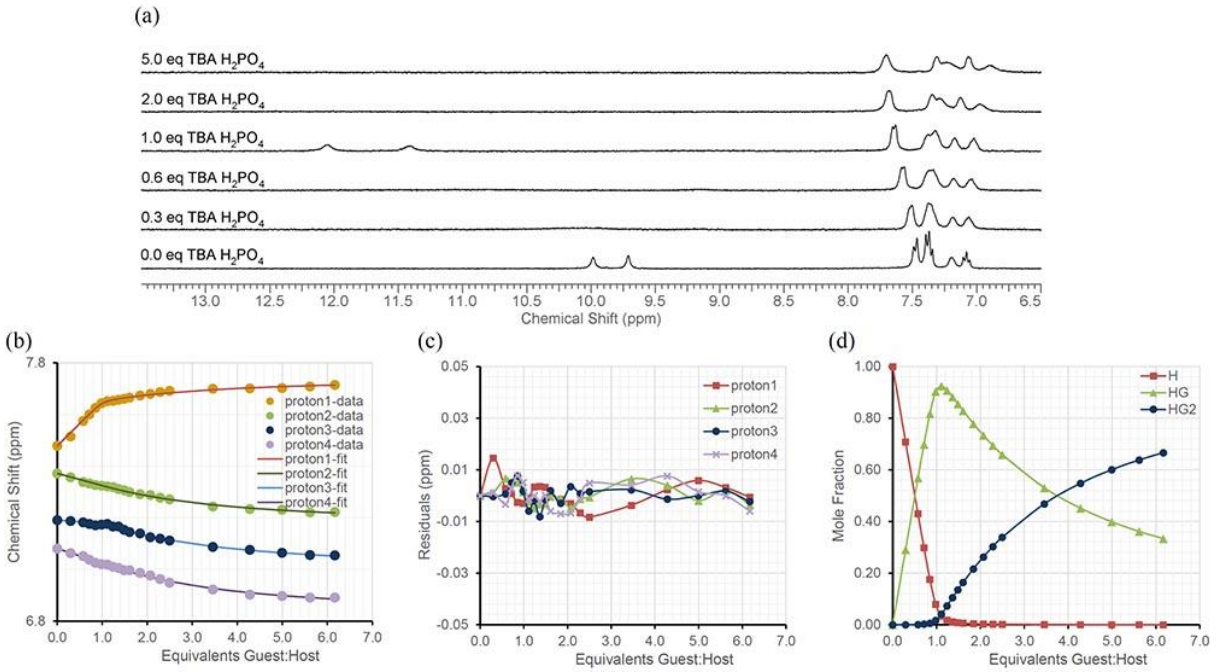

Figure S41. ^{1}H NMR spectroscopic titration of compound C1 with TBAH$_2$PO$_4$ in DMSO-*d*$_6$ with 0.5% water at 298 K. (a) Stack plot. (b) Fitplot for CH protons at δ = 7.48 ppm (proton1), δ = 7.37 ppm (proton2a), δ = 7.19 ppm (proton3), and δ = 7.08 ppm (proton4) using global analysis with 1:2 host:guest stoichiometry. $K_{11} > 10^4$ M^{-1}, $K_{12} = 43.9$ M^{-1} (error 4%). (c) Plot of the residuals for δ = 7.48 ppm (proton1), δ = 7.37 ppm (proton2a), δ = 7.19 ppm (proton3), and δ = 7.08 ppm (proton4) using global analysis. (d) Calculated mole fractions. The NH protons at δ = 9.99 ppm and δ = 9.71 ppm broadened too much for accurate analysis, while CH proton at δ = 7.37 ppm (proton2b, overlap with proton2a) did not shift enough to allow accurate analysis.

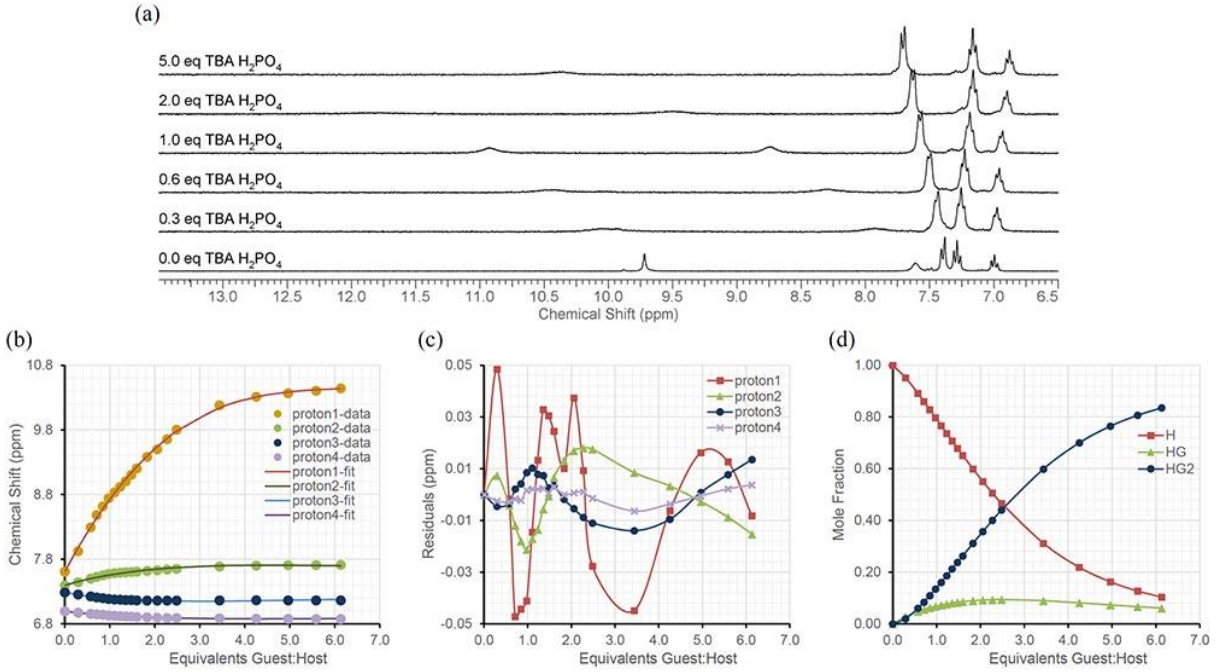

Figure S42. ^{1}H NMR spectroscopic titration of compound D1 with TBAH$_2$PO$_4$ in DMSO-*d*$_6$ with 0.5% water at 298 K. (a) Stack plot. (b) Fitplot for NH proton at δ = 7.61 ppm (proton1), and CH protons at δ = 7.40 ppm (proton2), δ = 7.29 ppm (proton3), and δ = 7.00 ppm (proton4) using global analysis with 1:2 host:guest stoichiometry. $K_{11} = 13.2$ M^{-1} (error 1.4%), $K_{12} = 307$ M^{-1} (error 9%). (c) Plot of the residuals for δ = 7.61 ppm (proton1), δ = 7.40 ppm (proton2), δ = 7.29 ppm (proton3), and δ = 7.00 ppm (proton4) using global analysis. (d) Calculated mole fractions. The NH proton at δ = 9.72 ppm broadened too much for accurate analysis.

S4.5. NMR spectroscopic titrations with TBA sulfate

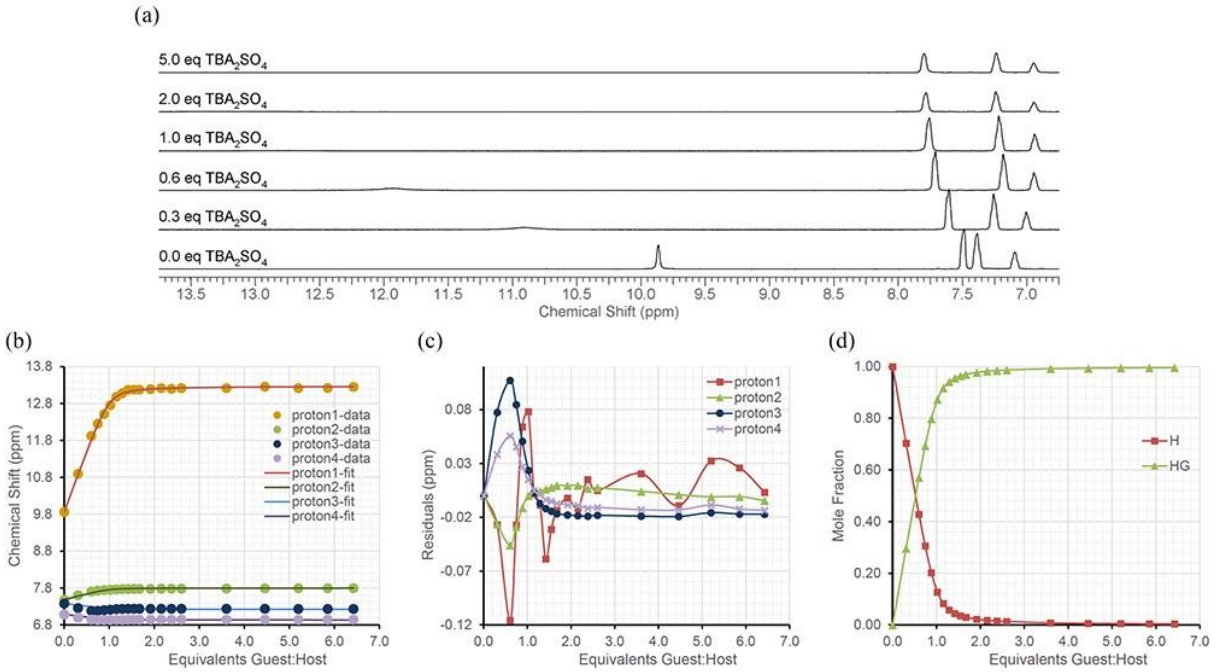

Figure S43. ^{1}H NMR spectroscopic titration of compound A1 with $(TBA)_2SO_4$ in DMSO-d_6 with 0.5% water at 298 K. (a) Stack plot. (b) Fitplot for NH proton at δ = 9.90 ppm (proton1) and CH protons at δ = 7.50 ppm (proton2), δ = 7.39 ppm (proton3) and δ = 7.09 ppm (proton4) using global analysis with 1:1 host:guest stoichiometry. K_a = 4593 M^{-1} (error 13%). (c) Plot of the residuals for δ = 9.90 ppm (proton1), δ = 7.50 ppm (proton2), δ = 7.39 ppm (proton3) and δ = 7.09 ppm (proton4) using global analysis. (d) Calculated mole fractions.

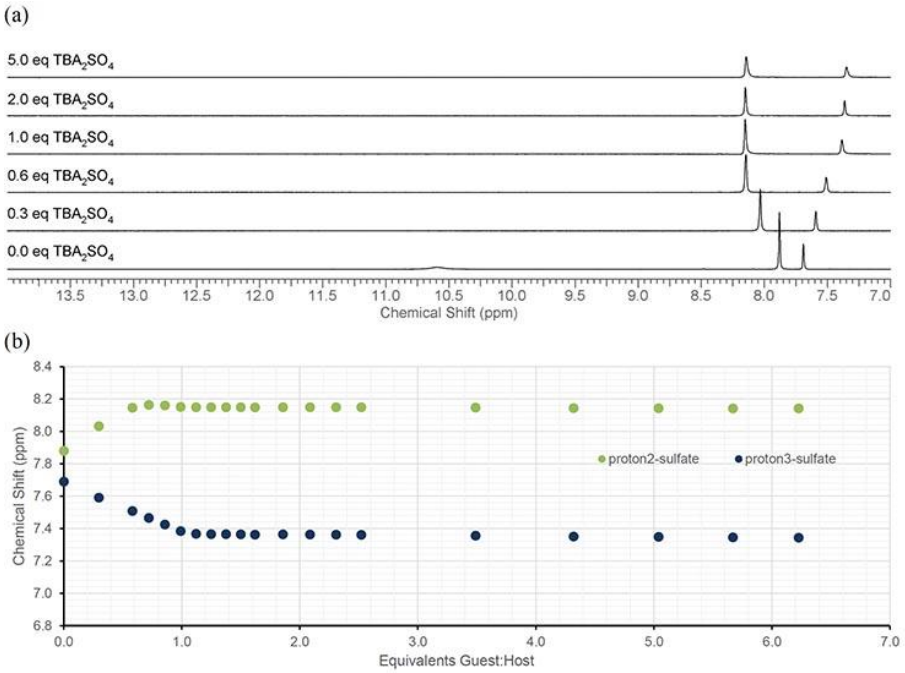

Figure S44. ^{1}H NMR spectroscopic titration of compound A3 with $(TBA)_2SO_4$ in DMSO-d_6 with 0.5% water at 298 K. (a) Stack plot. (b) Change in chemical shift for CH proton at δ = 7.88 ppm (proton2) and CH proton at δ = 7.69 ppm (proton3). NH proton at δ = 10.58 ppm (proton1) broadened too much upon the addition of anion. The data could not be fitted to any model. Possible deprotonation effects or complex stoichiometries might complicate the equilibria.

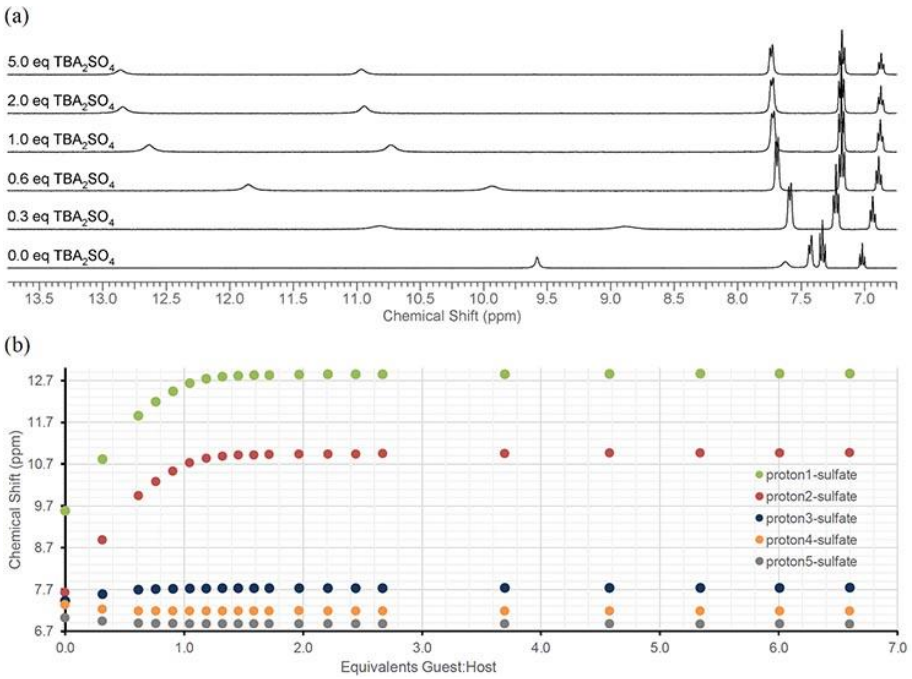

Figure S45. ^{1}H NMR spectroscopic titration of compound B1 with $(TBA)_2SO_4$ in DMSO-*d*$_6$ with 0.5% water at 298 K. (a) Stack plot. (b) Change in chemical shift for NH and CH protons at δ = 9.58 ppm (proton1), 7.63 ppm (proton2), 7.43 ppm (proton3), 7.33 ppm (proton4) and 7.02 ppm (proton5). The data could not be fitted to any model. Deprotonation by sulfate anions seems unlikely because the NH signals remain sharp. Complex stoichiometries might complicate the equilibria and hinder fitting of the data.

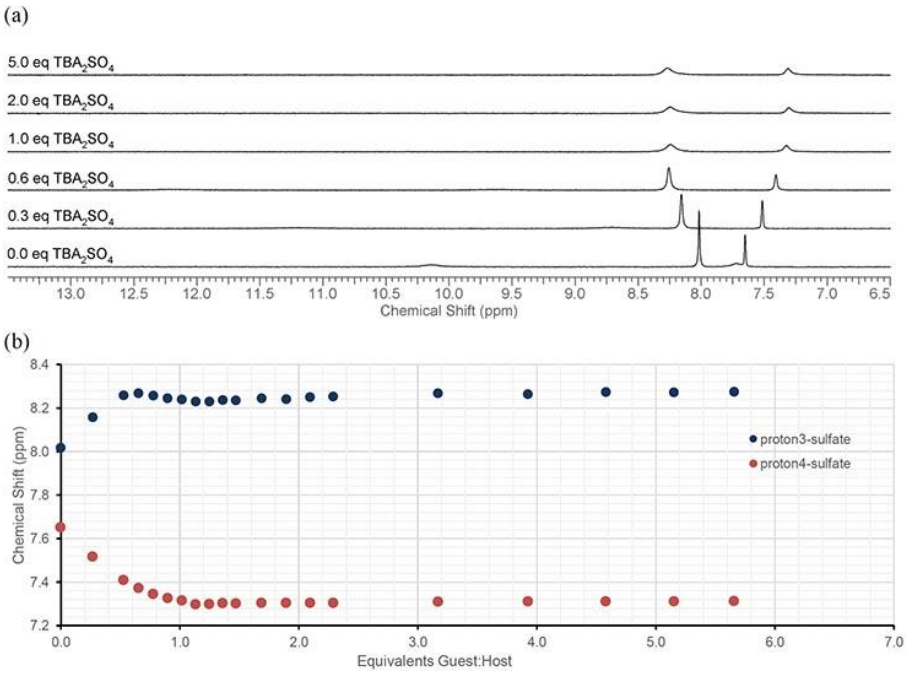

Figure S46. ^{1}H NMR spectroscopic titration of compound B3 with $(TBA)_2SO_4$ in DMSO-*d*$_6$ with 0.5% water at 298 K. (a) Stack plot. (b) Change in chemical shift for CH proton at δ = 8.02 ppm (proton3) and CH proton at δ = 7.65 ppm (proton4). The NH protons at δ = 10.14 ppm (proton1) and 7.72 ppm (proton2) broadened too much upon the addition of anion. The data could not be fitted to any model. Possible deprotonation effects or complex stoichiometries might complicate the equilibria.

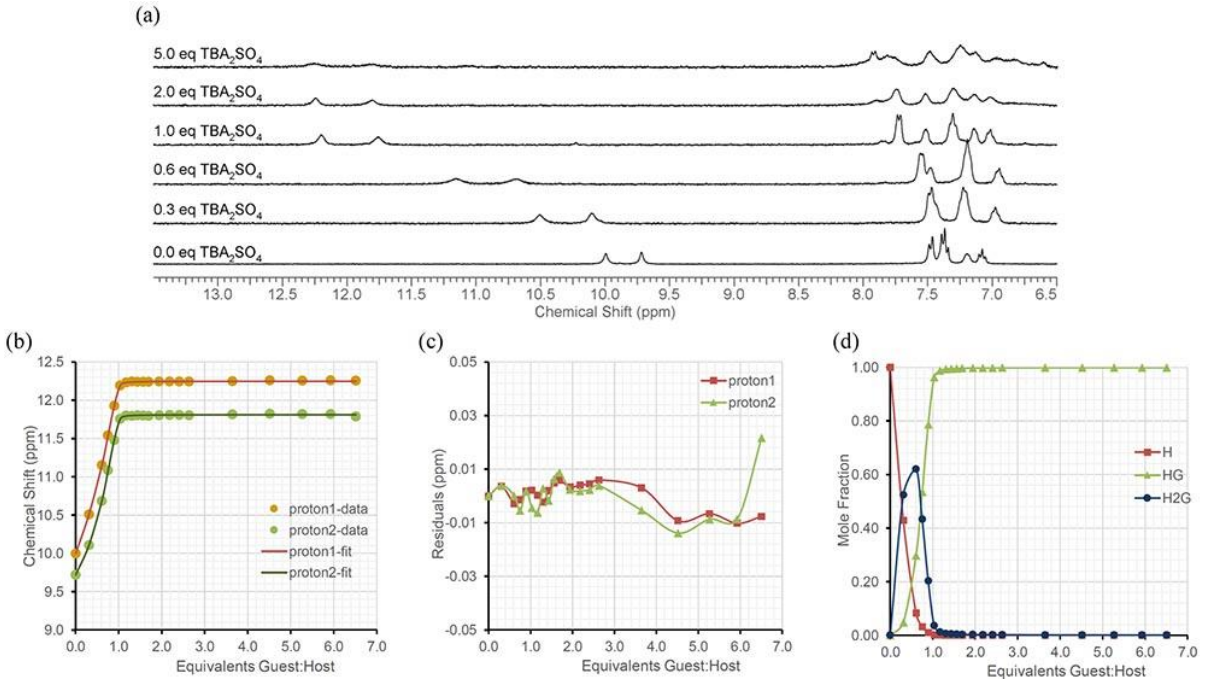

Figure S47. ^{1}H NMR spectroscopic titration of compound C1 with $(TBA)_2SO_4$ in DMSO-d_6 with 0.5% water at 298 K. (a) Stack plot. (b) Fitplot for NH protons at δ = 10.00 ppm (proton1) and 9.72ppm (proton2) using global analysis with 2:1 host:guest stoichiometry $K_{11} > 10^{-4}$ M^{-1}, $K_{21} = 1270$ M^{-1} (error 17%). (c) Plot of the residuals for δ = 10.00 ppm (proton1) and 9.72ppm (proton2) using global analysis. (d) Calculated mole fractions. The CH protons overlapped too much during the titration to allow accurate analysis.

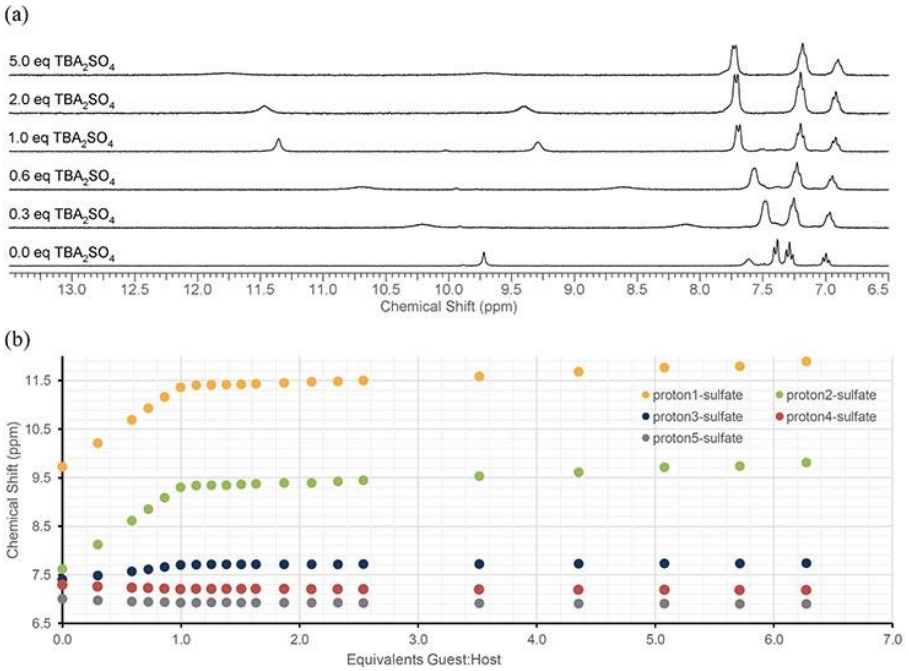

Figure S48. ^{1}H NMR spectroscopic titration of compound D1 with $(TBA)_2SO_4$ in DMSO-d_6 with 0.5% water at 298 K. (a) Stack plot. (b) Change in chemical shift for NH and CH protons at δ = 9.72 ppm (proton1), 7.61 ppm (proton2), 7.40 ppm (proton3), 7.29 ppm (proton4) and 7.00 ppm (proton5). The data could not be fitted to any model. Deprotonation by sulfate anions seems unlikely because the NH signals remain reasonably sharp. Complex stoichiometries might complicate the equilibria and hinder fitting of the data.

S5. IN VITRO STUDIES

S5.1. Materials and Methods

Cell lines and culture conditions: Human lung adenocarcinoma cell line (A549), human melanoma cell line (A375) and human prostatic carcinoma cell line (PC3) were purchased from the *American Type Culture Collection* (Rockville, MD), and were cultured in DMEM. Both media were supplemented with 10% FBS, 100 U/mL penicillin, 100 µg/mL streptomycin (all from *GIBCO BRL, Paisley, UK*), and 2 mM L-glutamine (*Sigma Chemicals Co, St Louis, MO, USA*), Cells were grown in a humidified atmosphere of air containing 5% CO_2 at 37° C.

Cell viability assay: Cell viability was determined by the MTT assay.[19] Briefly, adherent cell lines were plated in triplicate in microtiter cell culture plates 24 h before treatment at a concentration of $1x10^4$ in 100 µL of growth medium per well. For single dose experiments, cells were incubated in the absence (control cells only with drug diluent, DMSO) or in the presence of 10 µM of the 12 synthetic squaramides. A range of concentrations from 0.99 to 25 µM of the most cytotoxic squaramides, **A2** and **C3**, or a range from 5.93 to 100 µM in the case of squaramides **C1** were used for dose response experiments. After 24 hours incubation, 10 mM of MTT (3-(4,5-dimethylthiazol-2-yl)-2,5-diphenyltetrazolium bromide) diluted in 1xPBS was added to each well for an additional 4 hours. The medium was removed and 100 µL of DMSO was added to each well in order to dissolve the MTT formazan precipitate. Absorbance was measured at 570 nm on a Multiskan multiwell plate reader (*Thermo Fisher Scientific Inc., Waltham, MA, USA*). Cell viability was expressed as a percentage of control and IC_{50} represents the concentration of drug causing 50% inhibition of the increase in absorbance compared with control cells. Data are shown as the mean value ± SD of three independent experiments. The IC_{50} and IC_{75} values were calculated with *GraphPad Prism*™ 5 software (Graph Pad Software, San Diego, CA, USA).

Vital fluorescence microscopy: The living cultured cells were stained with acridine orange (AO).[20] Briefly, A375 cells ($50x10^3$) grown in a 12-well plate with cover slips for 24 h were exposed with the squaramides **A2**, **C1** and **C3** at the IC_{75} dose (9.79±0.42; 21.15±1.10 and 9.59±1.51 respectively) for 3 h or at the IC_{50} dose (8.86±0.63; 16.60±2.38; 8.03±1.19) for 1 h (DMSO was used for control cells). Afterwards cells were washed 3 times with PBS and incubated with 5 µg/mL AO solution for 30 min at room temperature. Finally, cover slips were washed three times with PSB supplemented 10% FBS and then examined with a *NIKON eclipse E800 microscope* (filter 330/380 nm) (Nikon Europe BV, Badhoevedorp, The Netherlands).

Hoechst staining: Cells were stained with the intercalating DNA dye Hoechst 33342 (*Sigma*) to reveal their nuclear morphology. A375 cells ($2x10^5$/mL) were seeded in 12-well plates, allowed to grow for 24 h and then incubated in the absence (control cells) or in the presence of 10 μM of squaramides **A2**, **C1**, and **C3** for 48 h. Afterwards cells were washed with 1xPBS and incubated with Hoechst 33342 at a final concentration of 2 μg/mL for 30 min at 37° C in the dark. Finally, cells were washed twice with 1xPBS and examined fluorometrically in a *NIKON eclipse E800 microscope* (SCT filter 330/380 nm).

Assessment of cell cycle arrest: A375 cells were synchronised maintained in normal culture condition with only 0.5% FBS for a period of 24 h before initiation of the experiment. Then cells were treated without and with the squaramides **A2** and **C3** at the IC_{50} dose for 6 h, 24 h and 48 h and fixed in 70% ethanol at -20° C overnight. Afterwards, cells were washed in PBS and the cell pellet was resuspended with 200 μL of Muse™ cell cycle reagent for 30 min at room temperature in the dark. Fluorescence was measured by flow cytometry on a *FACSCalibur* fitted with a 488 nm Ar laser, and data were analysed using *CellQuest Pro* software (Becton Dickinson, San Jose, CA) and *ModFit LT* cell cycle analysis software (Verity software, Topsham, ME).

S5.2. Results

We have previously reported the cytotoxic effects of squaramides **A2**, **B2**, **C2**, **C3**, **D2** and **D3**.[2] Compound **A2** was shown to be the most cytotoxic squaramide, with the ability to both induce apoptosis and inhibit autophagy by chloride transport processes. To reliably compare the old compounds to the new squaramides, all *in vitro* assays were repeated for all of the compounds under the same conditions and using the same cell lines. The *in vitro* cytotoxic activity of squaramides **A1-D3** was tested on a collection of different cancer cell lines from diverse origin [human lung adenocarcinoma cell line (A549), human melanoma cell line (A375) and human prostatic carcinoma cell line (PC3)]. Initially, we used a single point (10 μM) screening assay to evaluate the cytotoxicity (Figure 2, main text) of the above-mentioned compounds. The cells were counted and the MTT assay was performed in order to evaluate cell viability and proliferation by measuring the level of mitochondrial dehydrogenase activity.[19] The single point data showed that some of the squaramides showed cytotoxic effects towards the tested cell lines. Squaramides **A2** and **C3** were particularly cytotoxic with the A375 cell line being the most sensitive one (Figure 2, main text), the **B**-series squaramides had minimal cytotoxicity, while no significant effect was observed after treatment with the other squaramides at the same dose and time. Squaramide **A2** remains the most cytotoxic squaramide of the series, which is unsurprising as it is one of the most potent anion transporters of

the series (see Table S3, high initial rate of Cl^- transport, k_{ini}, and low EC_{50} values in Cl^-/NO_3^- antiport assays). The low cytotoxic effect of compounds **A3** and **C1** are more surprising, as these squaramides function as good anion transporters in the liposomal assays (see Table S3). In addition, compounds **C2** and **C3** showed weaker cytotoxic effects than previously reported.[2] However, there were solubility problems with the squaramides, especially the heavily fluorinated squaramides (**A3**, **B3**, **C3**, **D3**) and the entire **C**-series. We assume that the low cytotoxicity of these compounds is largely a consequence of the insolubility of the squaramides, and thus effective squaramide concentration during the assays was presumably lower than the desired concentration due to precipitation.

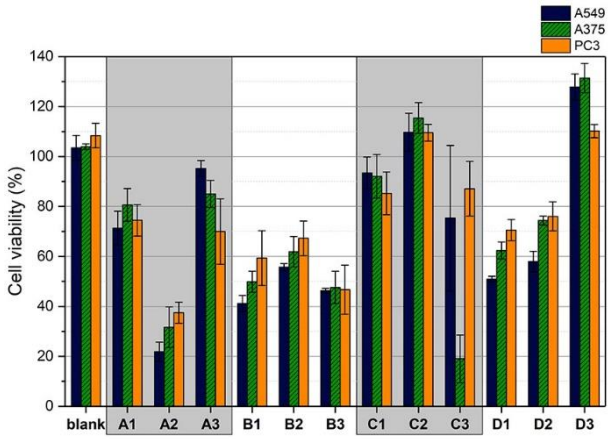

Figure S49. Cell viability after 24 h of squaramide treatment measured by MTT assay. Single-point screening of compounds **A1**-**D3** (10 µM) on a collection of different cancer cell lines (PC3, A375 and A549).

Dose–response curve experiments were performed and IC_{50} values (Inhibitory Concentration of 50% of cell population) were calculated for the most cytotoxic compounds (squaramides **A2** and **C3**) as well as for the non-cytotoxic squaramide **C1** in the 24 h viability assay in A549, A375 and PC3 cell lines (Table S7). These results corroborate the potency of these cytotoxic compounds, showing IC_{50} values less than 10 µM for squaramide **A2** in the three cell lines studied. The IC_{50} values obtained in A549 cells for compounds **A2** and **C3** are slightly different than previously reported,[2] but the relative activity remains the same (IC_{50} for **A2** is about half the IC_{50} value for **C3**). In general, the cytotoxic activity shows the trend **A2** > **C3** >> **C1**, as previously reported.[2]

Table S7. IC_{50} values (µM) of cytotoxic squaramides **A2**, **C1** and **C3** on A375, A549 and PC3 cancerous cell lines.

Squaramide	IC_{50} (µM) A375	IC_{50} (µM) A549	IC_{50} (µM) PC3
A2	8.9 ± 0.6	5.6 ± 0.8	3.0 ± 0.6
C1	16.6 ± 2.4	49 ± 4	26 ± 3
C3	8.0 ± 0.9	11.5 ± 3.1	15.9 ± 1.1

We have previously shown that **A2** can alter the lysosomal pH in HeLa cells, leading to disruption of autophagy and subsequent cell death, while compounds **C2** and **C3** did not show any ability to alter the lysosomal pH in HeLa cells.[2] To see if the same mechanism of cell death is true in the current cell lines, the *in vitro* ionophoric activity of the cytotoxic compounds was studied in A375 melanoma cells using vital staining with acridine orange (AO). This cell permeable dye accumulates in acidic compartments such as lysosomes exhibiting a characteristic orange fluorescence emission as a result of its protonation, whereas it emits green fluorescence at higher pH.[21] When A375 cells were stained with AO, granular orange fluorescence was observed in the cytoplasm (Figure S50a,b), suggesting that the orange fluorescence is due to acidified lysosomes. Cells treated with non-cytotoxic squaramide **C1** showed no changes (Figure S50e,f). Surprisingly, cells treated with the cytotoxic squaramides **A2** and **C3** also did not show a significant disappearance of orange emission when administered at their IC_{50} value, but at higher concentrations (IC_{75} values) the orange colour did disappear, indicating changes in the lysosomal pH (Figure S50c,d,g,h). These results are in agreement with our previous studies on **A2** which was shown to alter the lysosomal pH in HeLa cell.[2] However, our previous results for **C3** indicated that this compound cannot alter the lysosomal pH in HeLa cells.[2] It is possible that **C3**, which is a highly lipophilic and rather insoluble compound, has different cell permeabilities in HeLa cells and A375 cells. This implies that **C3** can cross the plasma membrane in A375 cells, and thus reach the lysosomes and alter the pH, but it cannot leave the plasma membrane of HeLa cells and therefore has no lysosomal activity in HeLa cells. Nonetheless, the fact that the lysosomal pH only changes at the higher IC_{75} concentration suggests that the cell permeability (and thus the ability to reach the lysosomes) of the squaramides is not optimal and that other processes are also responsible for the observed cytotoxicity of these compounds.

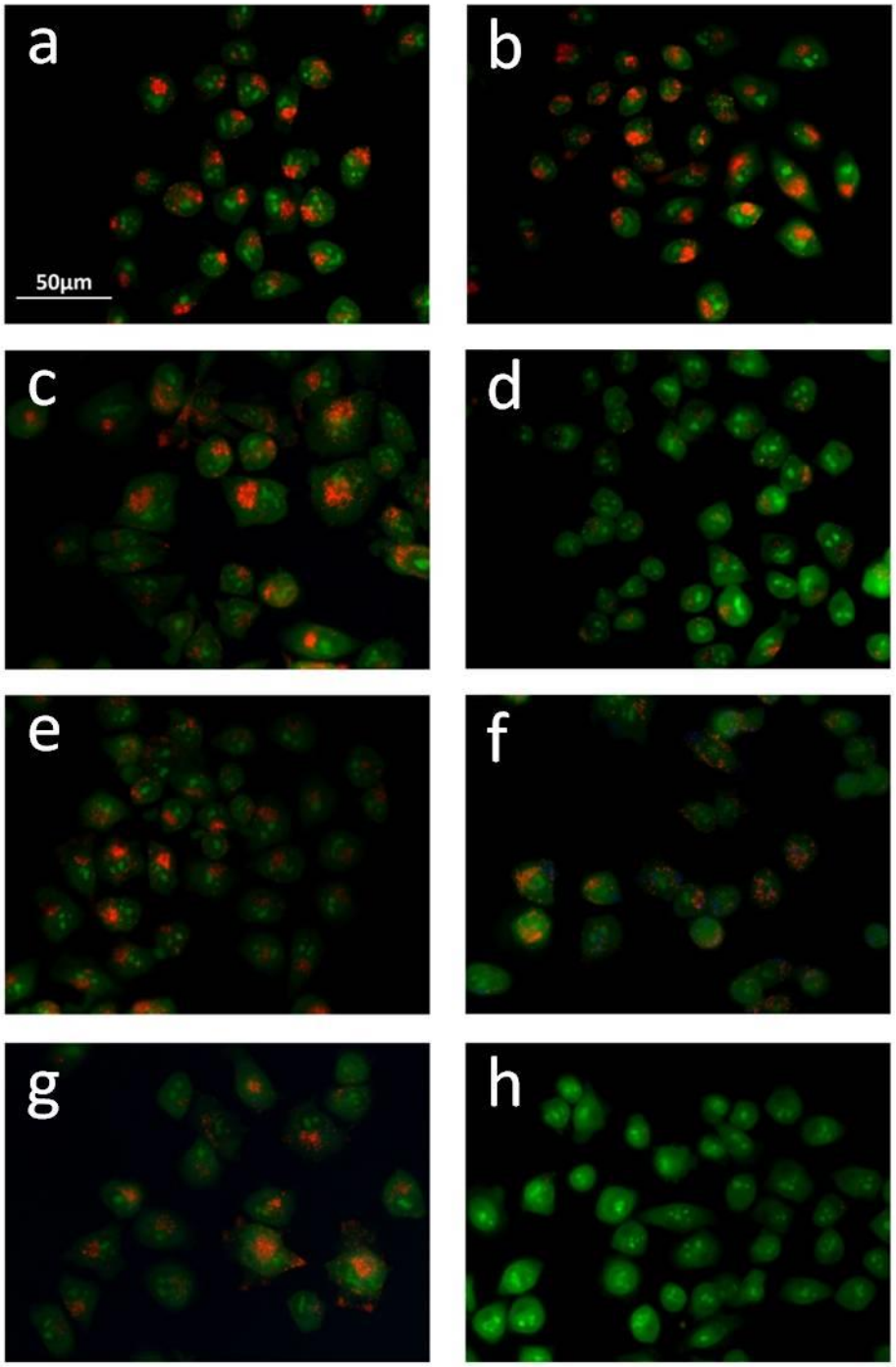

Figure S50. Acridine Orange staining of melanoma A375 cells after exposure to squaramides A2, C1 and C3 at the IC_{50} dose for 1 h or the IC_{75} for 3 h. (a, b) untreated cells, (c) **A2** at IC_{50} concentration for 1 h, (d) **A2** at IC_{75} concentration for 3 h, (e) **C1** at IC_{50} concentration for 1 h, (f) **C1** at IC_{75} concentration for 3 h, (g) **C3** at IC_{50} concentration for 1 h, (h) **C3** at IC_{75} concentration for 3 h. Cells with cytoplasmic granular orange fluorescence were observed (a, b, c, e, f and g), cells with disappearance of cytoplasmic orange fluorescence were detected in (d and h).

Our previous results indicated that squaramide **A2** displays cytotoxic effects by both disrupting autophagy through altering the lysosomal pH, and by inducing apoptosis by perturbing the cellular chloride concentrations.[2] We thus decided to investigate whether the active squaramides can also induce apoptosis in other cell lines (A375). Apoptosis is a tightly regulated form of cell death in

which cells actively participate in their own destruction. Drug-induced apoptosis is mainly initiated by either the activation of cell surface receptors or by directly targeting mitochondria.[22] Cells undergoing apoptosis by different stimuli, shrink and lose their normal intercellular contents and subsequently exhibit cytoplasmic and chromatin condensation and internucleosomal cleavage of DNA. In the final stages, cells change in nuclear morphology like nuclear condensation, fragmentation, holes in the nuclei of dead cells and appearance of apoptotic bodies identified by fluorescence microscopy.[23] All these nuclear alterations by cytotoxic compounds (squaramides **A2** and **C3**) as well as with non-cytotoxic squaramide **C1** were examined using Hoechst 33342 staining in A375 cells. Untreated A375 cells have typical rounded nuclei (Figure S51a). Following treatment with the squaramides **A2** and **C3** (10 µM for 48 hours), the cells showed nuclear condensation (Figure S51c,d) and the formation of apoptotic bodies, confirming that these compounds induce apoptotic cell death. However, with the non-cytotoxic squaramide **C1** the appearance of the nucleus was normal (Figure S51b). These results confirm that cytotoxic squaramides can induce apoptosis.

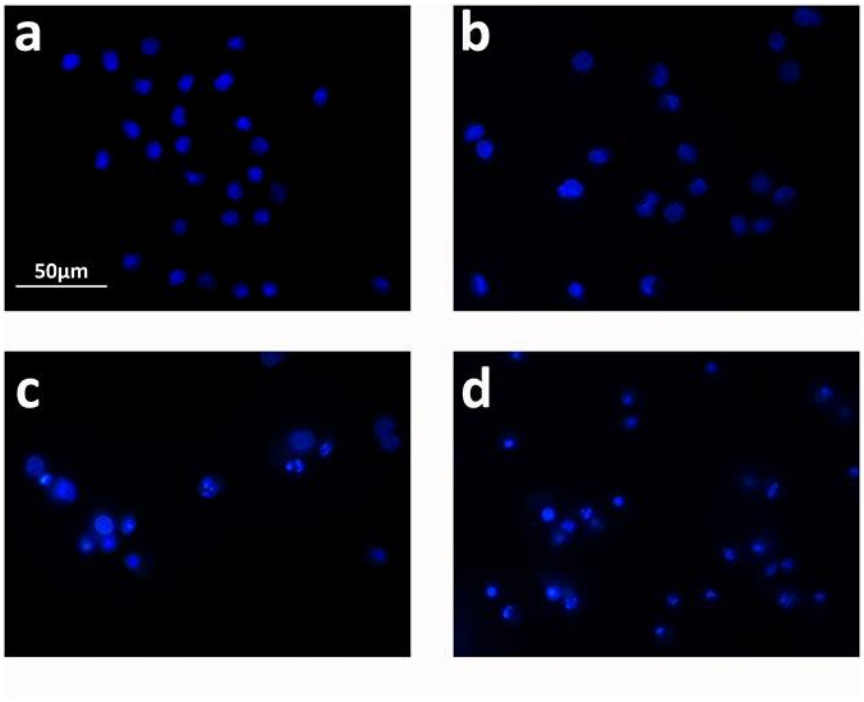

Figure S51. Hoechst 33342 staining of A375 cells after 48 h exposure of squaramides A2, C1 and C3 for 48 h (10 µM). (a) untreated cells, (b) squaramide **C1**, (c) squaramide **A2**, (d) squaramide **C3**. Cells with normal nuclear morphology were observed (a, and b), cells with nuclear condensation and apoptotic bodies were showed (c and d).

Considering the cytotoxic activity observed in the previous experiment, we further analysed the effects of squaramides **A2** and **C3** on cell cycle distribution of cultured A375 cells, determined by flow cytometry (Figure S52). After treatment of cells, we detected a slight modification in the

proportion of cells in G1 and S phases with squaramides **A2** and **C3** respectively at 24 and 48 h treatment time. However, the more significant changes were observed in the percentage of apoptotic population with an increase of 13.78% and 51.91% after 48 h of treatment with squaramides **A2** and **C3** respectively (Figure S52). These results correlate well with the viability results and Hoechst 33342 staining shown above, and with our previous results.[2] It is most likely that the apoptosis-inducing ability of these squaramides is the consequence of their ability to alter the cellular chloride (and sodium) concentrations through anion transport, as we have shown previously in detail for **A2**, **C2** and **C3** in different cell lines.[2]

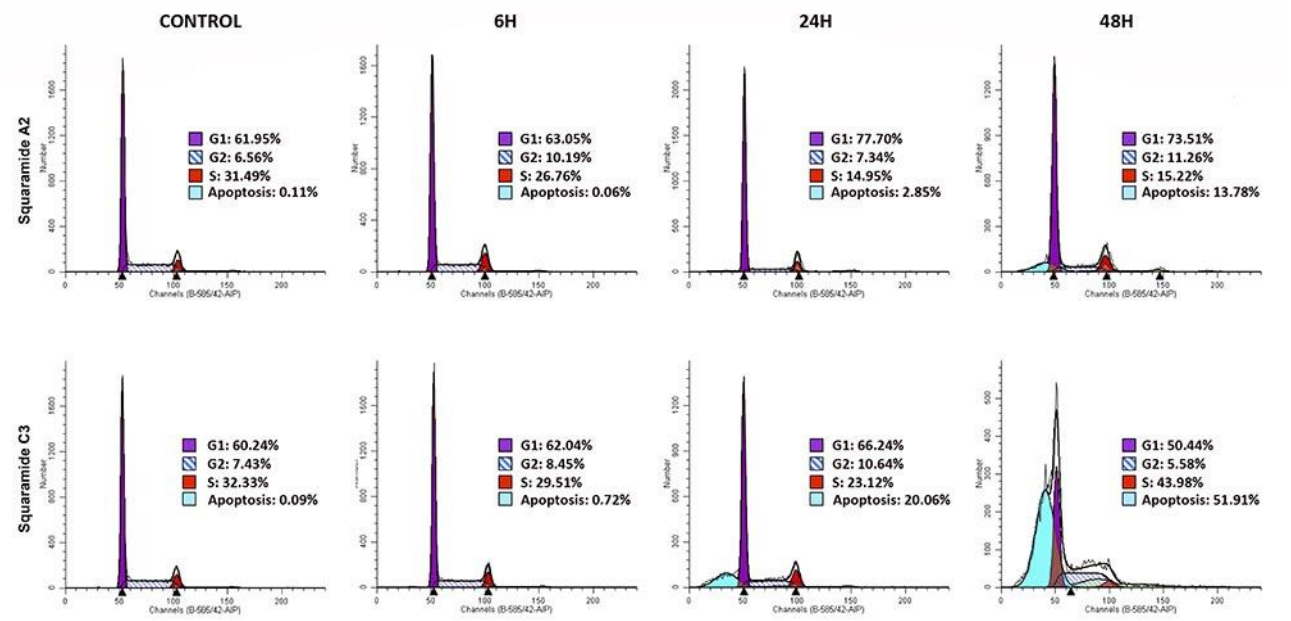

Figure S52. Flow cytometric analysis of the of A375 cells without treatment (control) or after 6 h, 24 h and 48 h squaramides A2 and C3 treatment at the IC_{50} dose. Numbers represent the percentage of cells in each cell cycle phase. Violet colour percentage of cells in G1 phase; striped bars percentage in G2/M phase; red colour percentage of cells in S phase and blue colour percentage of apoptotic cells. Data shown are representative of three independent experiments with similar results obtained in each.

S6. IN SILICO INVESTIGATIONS

S6.1. Detailed methods

Quantum Calculations

All quantum calculations reported in this paper were carried out with Gaussian 09 (Rev. A.02),[24] using different theory levels, as described along this work. These calculations include the geometry optimisations of the free squaramide derivatives and their chloride complexes, calculation of the Wiberg Bond Indices, and calculation of the distribution of electrostatic potential, as thoroughly detailed below. All optimised geometries have been characterised as minima by the absence of imaginary frequencies.

The distribution of the electrostatic potential, $V(\mathbf{r})$, on the molecular surfaces of the squaramide derivatives were computed from previously optimised structures of their chloride complexes, after removal of the anion, using the same level of theory. Subsequently, the $V(\mathbf{r})$ was evaluated on the 0.001 electrons Bohr^{-3} contour of $\rho(\mathbf{r})$, and is henceforth labelled $V_S(\mathbf{r})$. The electrostatic potential surface ranges, including the most negative and most positive values ($V_{S,min}$ and $V_{S,max}$, respectively), were ascertained using Multiwfn.[25]

The E^2 energy derived from the 2nd Order Perturbation Theory Analysis was ascertained from the DFT optimised structures of the chloride squaramide complexes, using Natural Bond Orbital (NBO) Version 6.0 program,[26-28] at the same level of theory.

Molecular Dynamics

The MD simulations were carried out with AMBER 14[29] (passive diffusion), NAMD 2.9[30] (steered molecular dynamics) or AMBER 16[31] (umbrella sampling simulations), with resort to GPU acceleration.[32-34] The LIPID14[35] force field was employed for the POPC lipids, while GAFF[36, 37] parameters and atomic RESP charges[38] were used for the squaramide derivatives, as follows.

The initial structures of **A1**, **A2**, **A3** and **D1** were obtained directly from the crystal structures deposited with the Cambridge Crystallographic Data Centre (CCDC),[39] with the Refcodes FAXBUD, FAXCEO, FAWZAG,[1] and WELXUI.[3] On the other hand, the structures of the **B**-series were obtained from the corresponding **A**-series analogues, with the replacement of the phenyl moieties by an alkyl chain. **C1** was generated by atomic manipulation of the crystal structure with the Refcode DETYAD,[40] with the inclusion of necessary phenyl moieties. The structures of C2, C3, D2 and D3, due to their complexity, were generated at a later stage (*vide infra*).

Subsequently, these structures were optimised at the HF/6-31G* level with the Gaussian 09 software.[24] The optimisation of these eight individual structures was followed by a single point calculation to generate the electrostatic potential (ESP) at the same theory level, using the Merz-

Singh-Kollman scheme with 4 concentric layers per atom and 6 density points in each layer (IOp(6/33=2, 6/41=4, 6/42=6)). The initial atomic charges of each molecule were then calculated by RESP fitting, along with the attribution of GAFF atom types, using the antechamber module, as implemented in the AMBER software suite.[41]

To obtain atomic charges less dependent of the molecular conformation or orientation, the calculation of the final RESP charges employed in all membrane MD simulations was preceded by conformational analyses on the squaramide derivatives, as follows: The initial molecular mechanics (MM) energy minimised structures, using the initial RESP charges, were heated at high temperature in the gas phase for 50 ps, followed by collection runs of 0.1 ns for the individual molecules of series **A** and **B** or 2 ns for molecules **C1** and **D1**, in agreement with the structural complexity of each subset, and using a time step of 1 fs, allowing the stochastic search of the conformational space. Frames were saved every 0.1 ps leading to trajectory files containing 1000 structures for series **A** and **B** and 20000 structures for molecules **C1** and **D1**. All these structures were further minimised by MM using a steepest descendent gradient followed by the conjugate gradient algorithm, until the convergence criterion of 0.0001 kcal·mol^{-1}·Å^{-1} was attained. Afterwards, the MM minimised structures were clustered with the UCSF Chimera software.[42] From the resulting clusters, three representative conformations with substantially different RMSD values were selected for **A1**, while for the remaining mono-squaramide derivatives four conformations were selected. Five and eight individual conformations were selected for **C1** and **D1**, respectively. The fluorinated analogous of these two subsets were obtained from **C1** and **D1**, adding the suitable number of $-CF_3$ groups. All selected conformations had the N−H binding units of the squaramide moieties adopting a *syn* configuration, but different spatial dispositions of the phenyl substituents. All these structures underwent further HF/6-31G* geometry optimisations and ESP calculations as described above. The individual ESP data were extracted from the corresponding Gaussian 09 outputs and then the ESP data of the corresponding conformations were concatenated and subsequently used to generate the input files for the two-stage RESP fitting, using identical weights for all conformations.

The structures of the chloride complexes of the individual squaramide derivatives in subsets **A**, **B** and **C**, as well as **D1**, were obtained in gas phase via conformational analyses as described above for the free receptors. However, the production runs were carried out for 5 ns, leading at the end of the quenched dynamics protocol to 50000 MM minimised structures. Moreover, for series **A** and **B** (apart **A3**, with four $-CF_3$ moieties), a 5 kcal·mol^{-1} distance restraint between the nitrogen atoms of the N−H binding units and the anion was employed. The lowest energy structure of each complex, was selected for DFT optimisation at the M06-2X/6-31+G(d,p) level of theory. The initial geometries of the chloride complexes of **D2** and **D3** were generated from **D1**, as described above. The quantum optimised structures of the squaramide chloride complexes were used in further single point quantum

calculations (such as the determination of the E^2 energy values or the distribution of the electrostatic potential, *vide infra*), as well as starting binding arrangements in MD simulations in POPC bilayer model.

The MD membrane simulations were carried out with the chloride complexes immersed in the water slab of a free membrane with Packmol,[43] affording a starting scenario W. This previously equilibrated membrane system is a POPC membrane model, with an orthorhombic shape composed of 128 phospholipids, 6500 TIP3P model water molecules,[44] 18 Cl^- and 18 Na^+ ions (*ca*. 0.15 M). The ions were described with van der Waals parameters obtained from ref. 45. Due to the insertion of the chloride complexes, an additional Na^+ counter-ion was also added to the system, to neutralise the net charge, without significant impact on the NaCl concentration.

The MD simulations were carried out as follows: the initial configuration of each system was submitted to 20000 steps of MM energy minimisation with a 500 kcal·mol^{-1}·Å^{-2} positional restraint on the chloride complex and lipid molecules, through the steepest descent algorithm for 10000 steps plus 10000 steps of the conjugated gradient algorithm, followed by the relaxation of the entire system for another 20000 steps, with the same protocol. The equilibration of the system proceeded by heating it to 303 K in an NVT ensemble for 100 ps with a 10 kcal·mol^{-1}·Å^{-2} restraint on the chloride complex and lipid molecules. The equilibration stage proceeded with a 5 ns run using an NPT ensemble with a 5 kcal·mol^{-1}·Å^{-2} restraint on the chloride complex. Then, the positional restraint was removed and the simulation continued for further 200 ns. The long-range electrostatic interactions were described with the Particle Mesh Ewald (PME) algorithm[46] using a real-space cut-off at 10 Å. The cut-off for the Lennard-Jones interactions was also set at 10 Å. The temperature of the system was maintained at 303 K, using the Langevin thermostat,[47] with a collision frequency γ of 1.0 ps^{-1}. The pressure was controlled by the Berendsen barostat[48] at 1 atm and compressibility of 44.6×10^{-6} bar^{-1}, with a relaxation time of 1.0 ps. The covalent bonds to hydrogen atoms were constrained using the SHAKE algorithm,[49] allowing the use of a 2 fs time step. The MD simulation trajectory frames were saved every 10.0 ps.

The MD simulations were also carried out with the chloride complexes inserted into the core of the bilayer, affording scenario M. In these simulations, the membrane model accounts only 4040 water molecules and a total of 11 Na^+ and 11 Cl^- ions, maintaining ionic strength. The simulation protocol was the same given for simulations of scenario W. At least two independent runs were carried out for the planar squaramides (series **A**, **B** and **C**), while for the tripodal chloride complexes two independent runs were carried out for each initial orientation of the complex, either vertically or horizontally to the membrane normal.

Moreover, for selected molecules, from the end of the equilibration period of the first MD run in both scenarios, an independent MD production run of at least 200 ns was undertaken with the chloride

complex maintained with 3.5 Å distance restraints between the nitrogen atoms of the squaramide moieties and the chloride, using harmonic restraints of 5 kcal·mol^{-1}·Å^{-2}. Table 2 in the main text summarises the number of MD runs, as well as the time lengths, for all these simulations.

The final frame of the equilibration period of the W scenario of molecules **A1**, **A2** and **A3** was used as the starting frame for the Steered Molecular Dynamics (SMD) simulations. Two approaches were employed: diffusion of the free receptor or diffusion of the anion complex of each squaramide derivative. The free receptors were dragged across the lipid bilayer normal (*viz*, *z*-dimension, the reaction coordinate) at 2.5 Å ns^{-1} in 32 ns long MD simulations, while the anion complexes were dragged at 5.0 Å ns^{-1} throughout a MD simulation with 16 ns, in the NPT ensemble. Throughout the travelled 80 Å along the membrane system, a force constant of 5.0 kcal·mol^{-1}·Å^{-2} was applied to the non−hydrogen atoms of the squaramide derivatives, while the anion complex was preserved with the use of two harmonic distance restraints between the nitrogen atoms and the chloride (*vide supra*), a feature that was only possible with the use of collective variables in NAMD 2.9.[30] In a frame from the equilibrated free membrane, a solvated chloride ion was pulled along the bilayer normal at 5.0 Å ns^{-1} in a 16 ns long MD simulation in the NPT ensemble. A force constant of 5.0 kcal mol^{-1} Å^{-2} was applied to the anion along the 80 Å of the membrane system.

From the SMD simulations of the free or anion associated **A** molecules, as well as the free chloride ion, several starting configurations were selected as starting points for independent Umbrella Sampling (US) simulations. The spacing between the centre of mass of the squaramide derivative in the US simulations is *ca*. 1 Å, with a total of 67 evenly spaced independent starting points (ranging from +33 to −33 Å along the *z*-dimension). Each one of the 67 windows was simulated for 30 ns, with the first 20 ns being discarded as equilibration period, with a positional restrain of 3.0 kcal·mol^{-1}·Å^{-2} applied only in the *z*-dimension, a feature that has only become available in AMBER16.[31] In the US simulations of the squaramide complexes, two 5.0 kcal·mol^{-1}·Å^{-2} harmonic distance restrains between the anion and the nitrogen atoms were applied. Given that the initial structures for the US windows of the squaramide complexes had been generated in NAMD, each independent window was preceded by a minimisation and heating stage, with the same distance restraints of the production run. The remaining details are as given for the passive diffusion simulations, except for the positional restrains. The production trajectory frames were saved every 10 ps, while the distance between the centre of mass of the squaramide derivative and the POPC bilayer was saved every 50 steps.

S6.2. Additional Figures

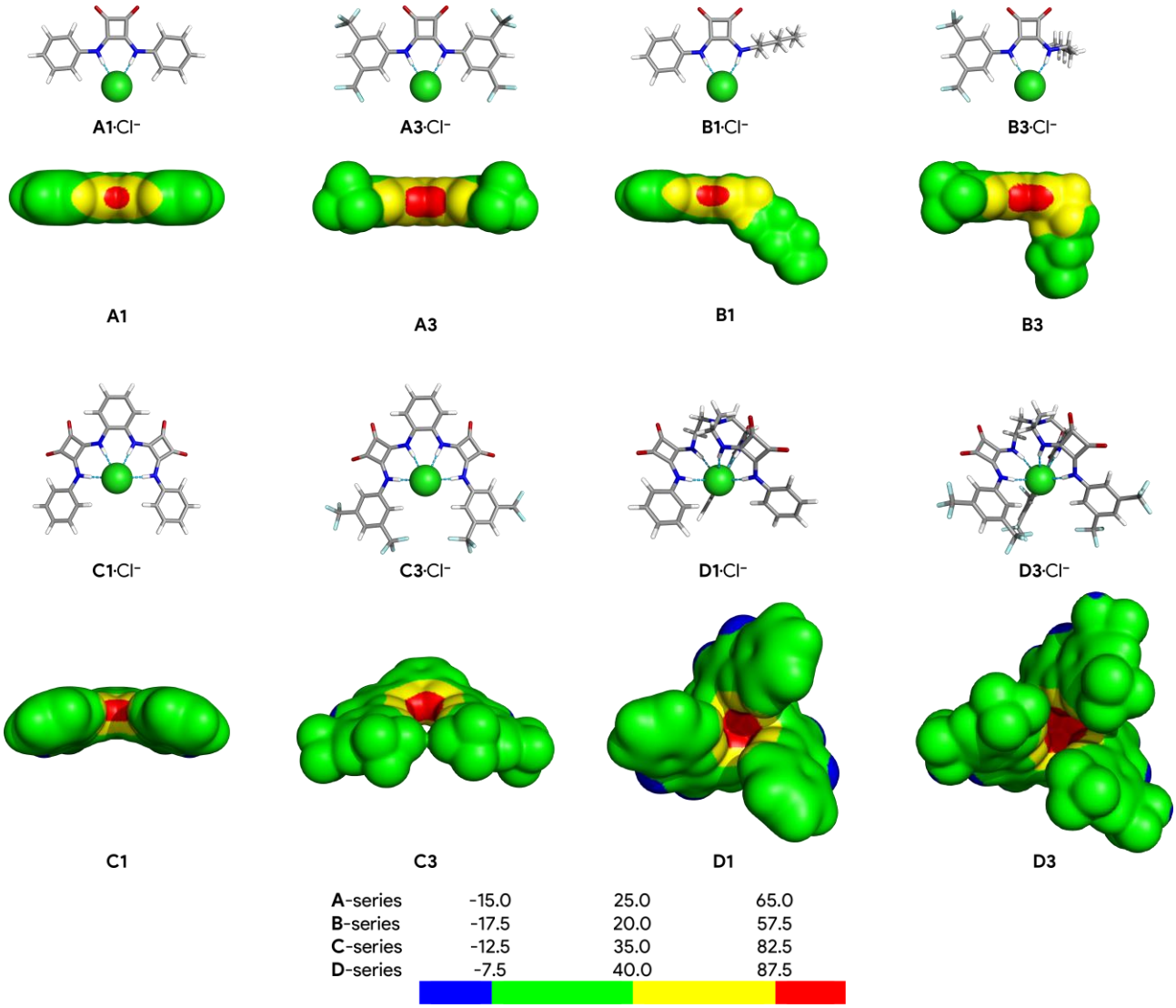

Figure S53. DFT optimised structures of squaramide chloride complexes and distribution of the electrostatic potential mapped on the 0.001 electrons Bohr^{-3} isodensity surface of the corresponding squaramide derivatives. The hydrogen, carbon, oxygen, nitrogen, fluorine atoms are shown in white, grey, red, blue and cyan sticks, respectively, while the chloride ion is shown as a green sphere. The colour scales are given in kcal mol^{-1}.

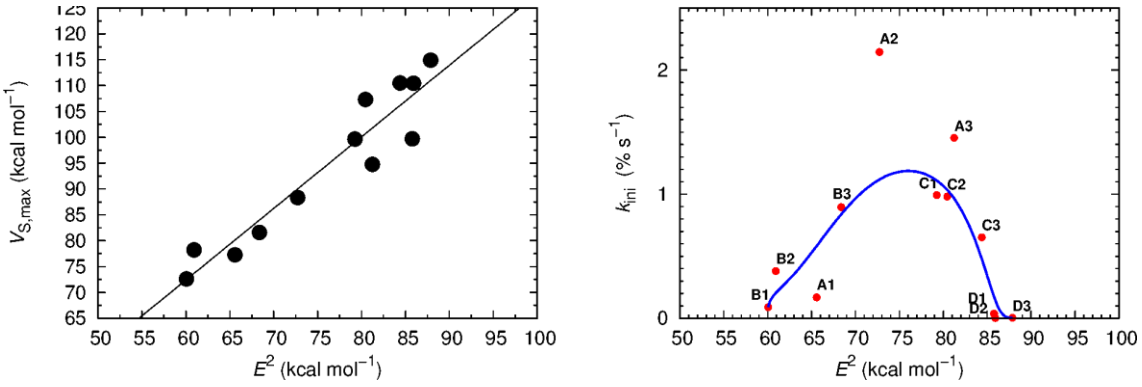

Figure S54. Structure-activity relationships. Left: $V_{S,max}$ values of the twelve squaramide derivatives plotted as a function of the E^2 energy values (R^2 = 0.90). Right: Plot of k_{ini} *vs* E^2 (red dots) and corresponding data smoothed Bézier curve (blue line).

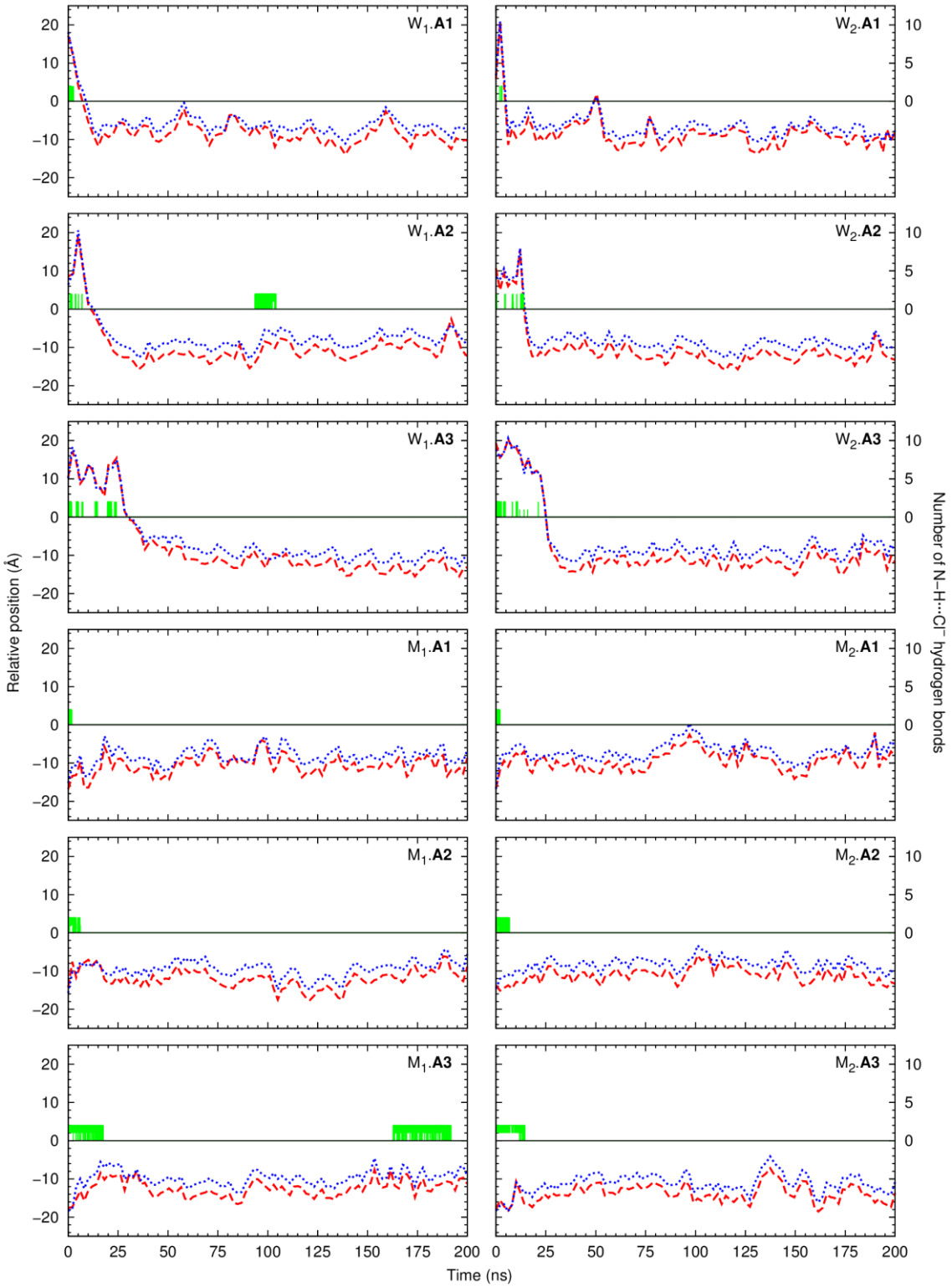

Figure S55. Evolution of the C=O$_{COM}$···P$_{int}$ (red dashed line) and N–H$_{COM}$···P$_{int}$ (blue dotted line) distances throughout 200 ns for the MD runs of the A-series chloride complexes in scenarios W and M. The evolution of the number of N−H···Cl$^-$ hydrogen bonds is also plotted as a green line. The water/lipid interface is represented as a black line at z = 0 Å. Data were smoothed using Bézier curves.

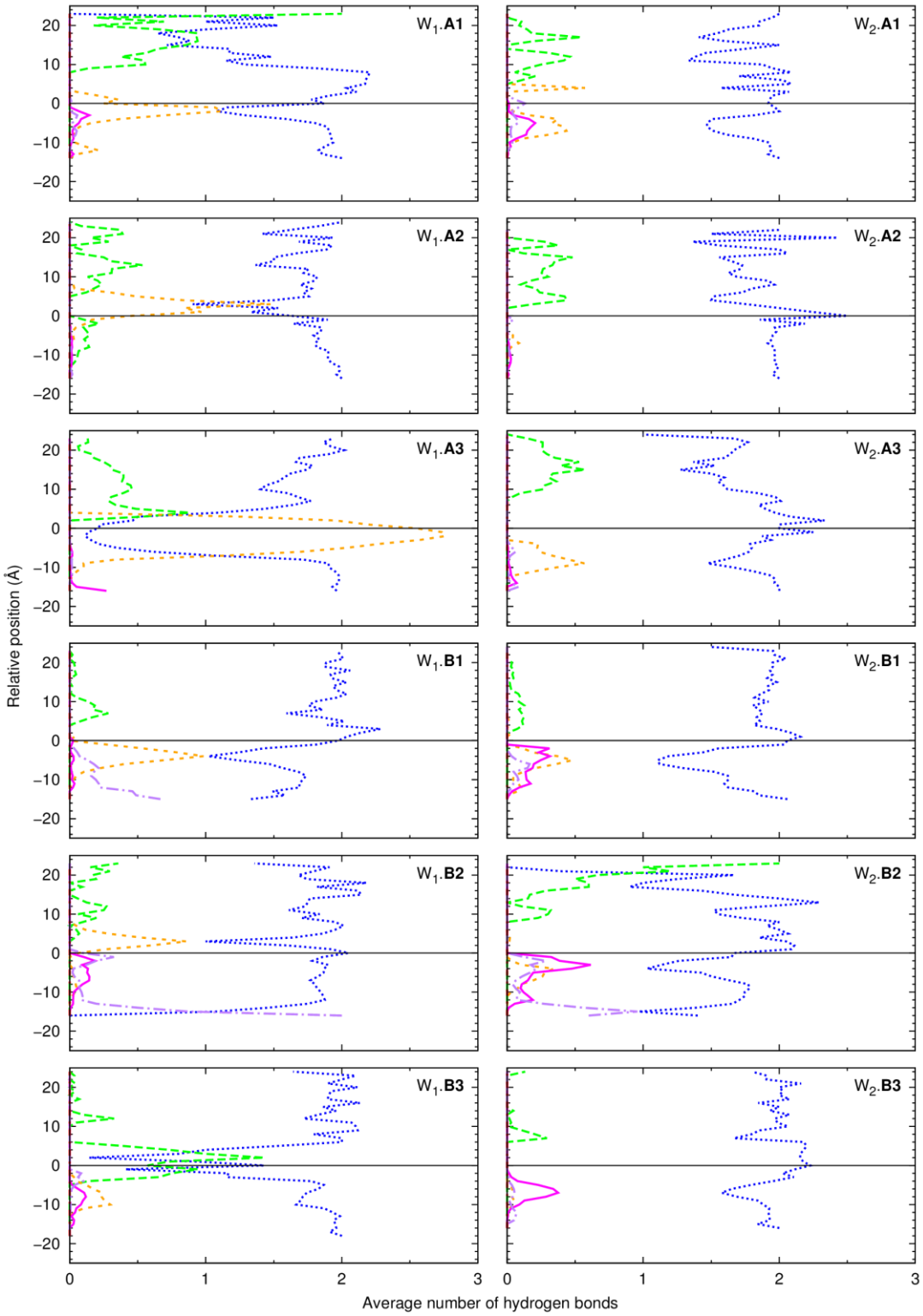

Figure S56. Average number of hydrogen bonds *vs.* the relative position of the COM of the A- and B-series molecules in the MD runs carried out in scenario W. The following colour scheme was used for the interactions between the squaramide derivative and chloride ions (green dashed line), water molecules (blue dotted line), POPC head groups (orange short dashed line), and ester groups (magenta solid line for the *sn*-1 chains and purple dot-dashed line for the *sn*-2 chains). The water/lipid interface is represented as a black line at $z = 0$ Å. Data were smoothed using Bézier curves.

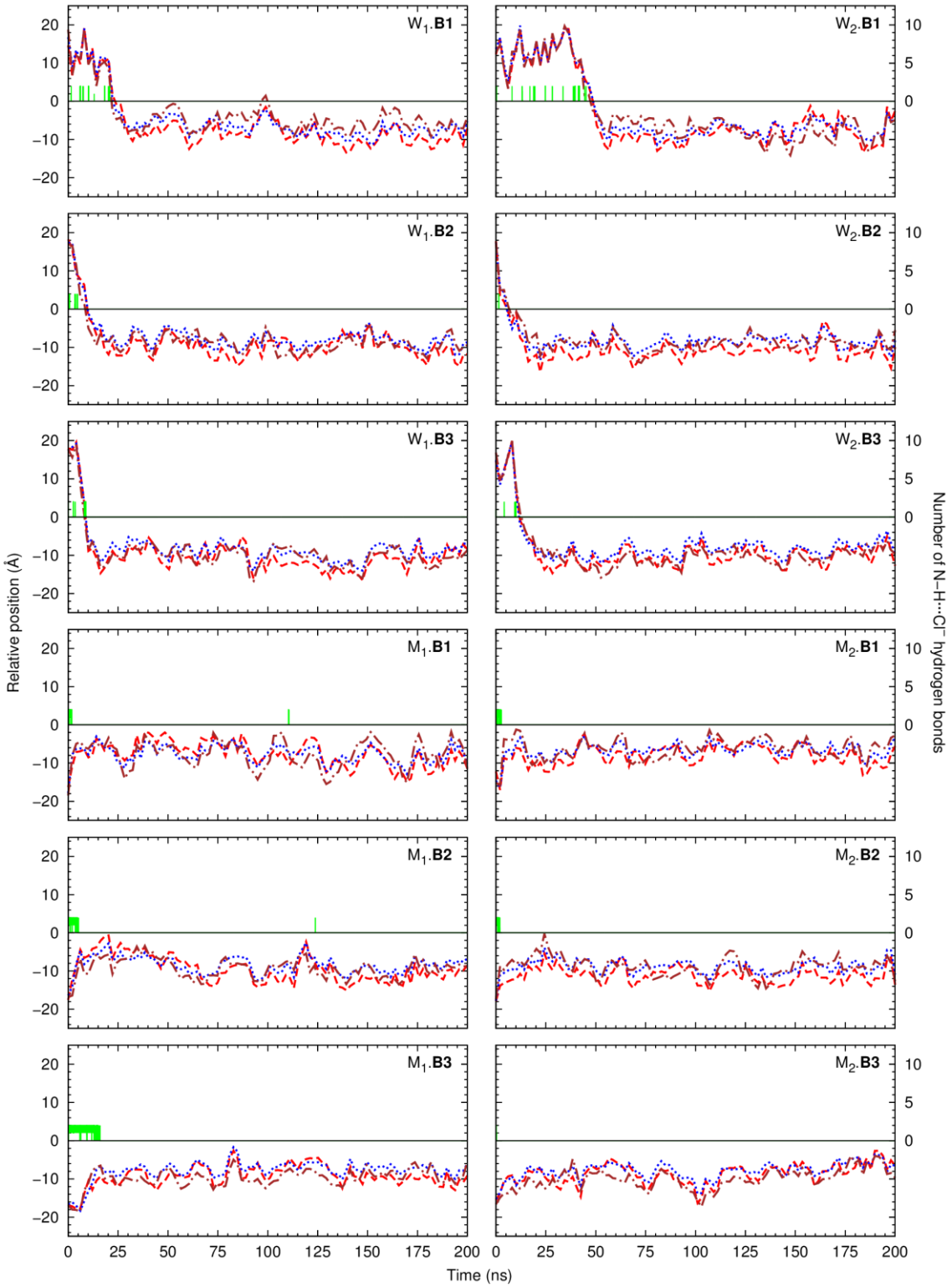

Figure S57. Evolution of the C=O$_{COM}$···P$_{int}$ (red dashed line), N–H$_{COM}$···P$_{int}$ (blue dotted line) and Ph$_{COM}$···P$_{int}$ (brown dot-dashed line) distances throughout 200 ns for the MD runs of the B-series chloride complexes in scenarios W and M. The evolution of the number of N−H···Cl$^-$ hydrogen bonds is also plotted as a green line. The water/lipid interface is represented as a black line at z = 0 Å. Data were smoothed using Bézier curves.

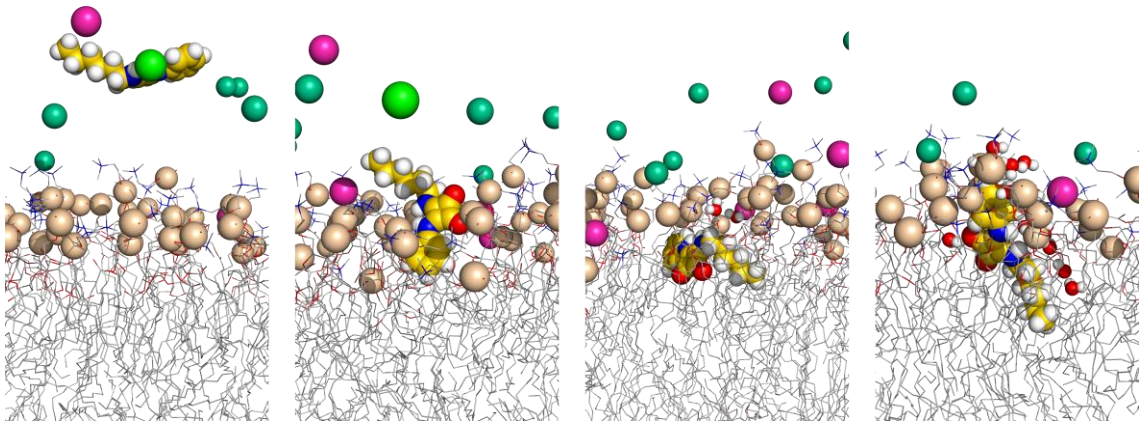

Figure S58. Consecutive snapshots depicting the diffusion of the chloride complex of B1 throughout the MD simulation W_1.B1. The squaramide derivative, sodium and chloride ions together with the phosphorus atoms are represented in spheres. The water molecules and the remaining atoms of the bilayer are shown as lines. The hydrogen atoms are shown in white, oxygen atoms in red, nitrogen atoms in blue, phosphorus atoms in wheat and carbon atoms in yellow (**B1**) or grey (phospholipids). The sodium ions are shown in pink and the chloride ions are shown in green (complex) or green marine (counter ions). The interaction of the internalised **B1** with the solvent molecules is emphasised with the depiction of water molecules within 3.5 Å from **B1** as spheres. The lipids' C–H bonds are omitted for clarity.

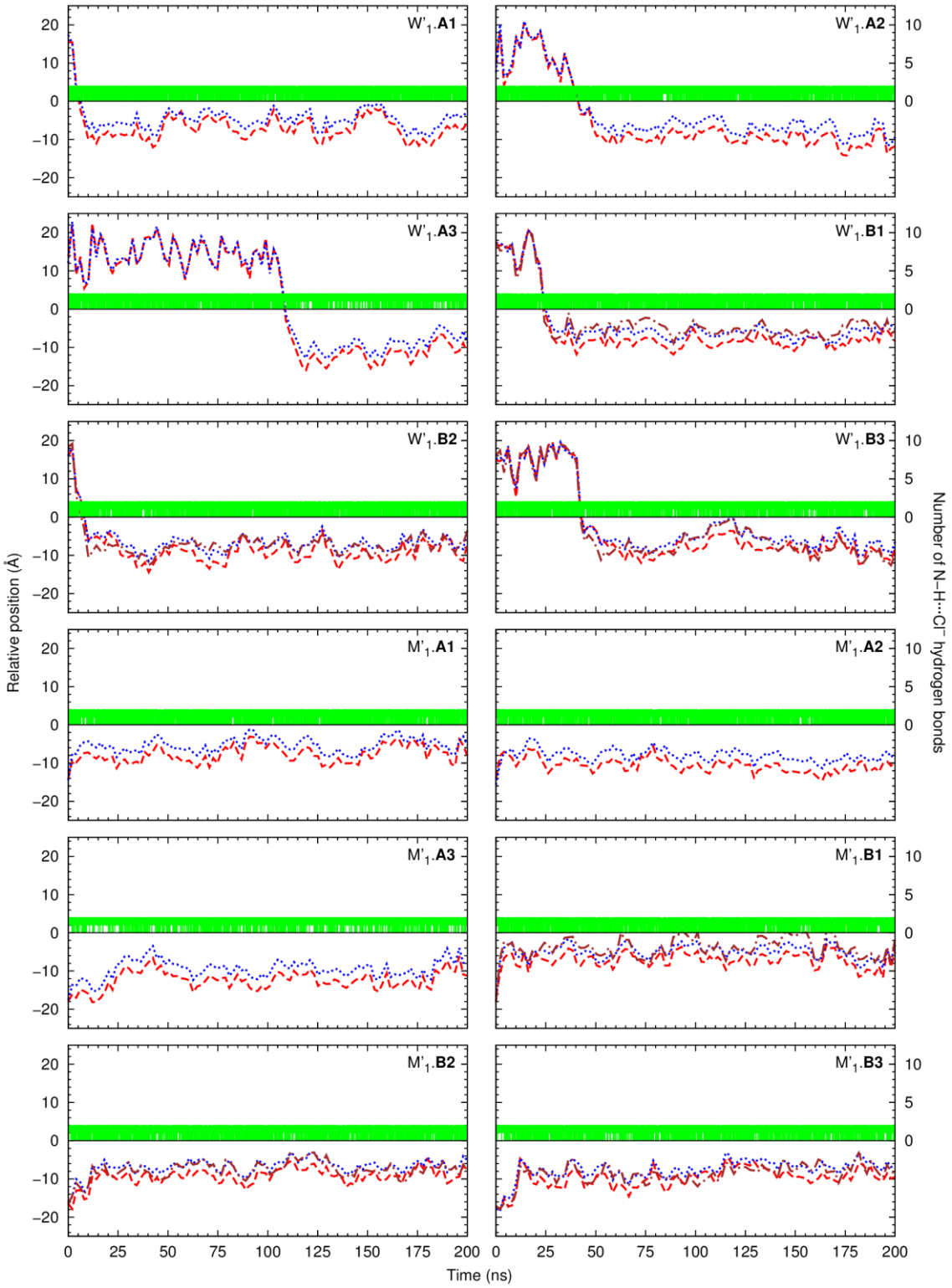

Figure S59. Evolution of the C=O$_{COM}$···P$_{int}$ (red dashed line), N–H$_{COM}$···P$_{int}$ (blue dotted line) and Ph$_{COM}$···P$_{int}$ (brown dot-dashed line) distances throughout 200 ns for the MD runs of the A- and B-series chloride complexes in scenarios W' and M'. The evolution of the number of N−H···Cl$^-$ hydrogen bonds is also plotted as a green line. The water/lipid interface is represented as a black line at z = 0 Å. Data were smoothed using Bézier curves.

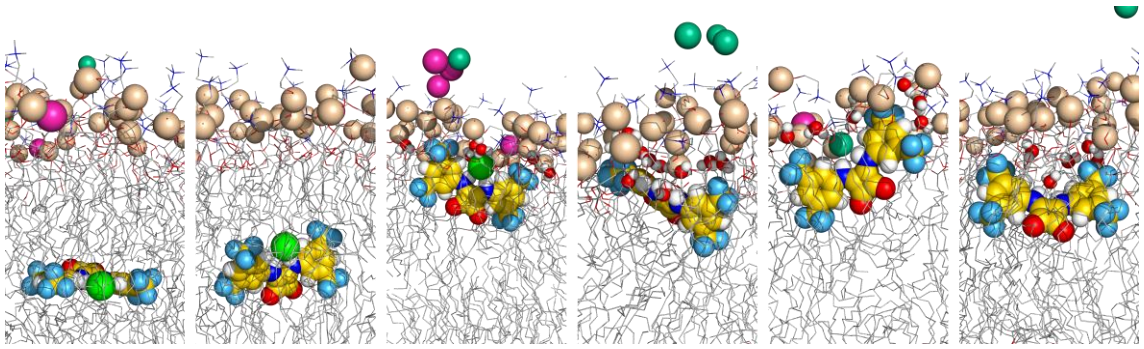

Figure S60. Consecutive snapshots depicting the diffusion of the chloride complex of A3 throughout the MD simulation M_1.A3. The squaramide derivative, sodium and chloride ions together with the phosphorus atoms are represented in spheres. The remaining atoms of the bilayer are shown as lines. The hydrogen atoms are shown in white, oxygen atoms in red, nitrogen atoms in blue, fluorine atoms in light blue, phosphorus atoms in wheat and carbon atoms in yellow (**A3**) or grey (phospholipids). The sodium ions are shown in pink and the chloride ions are shown in green (complex) or green marine (counter ions). The interaction of the internalised **A3** with the solvent molecules is emphasised with the depiction of water molecules within 3.5 Å from **A3** as spheres. Most water molecules and the lipids' C–H bonds are omitted for clarity.

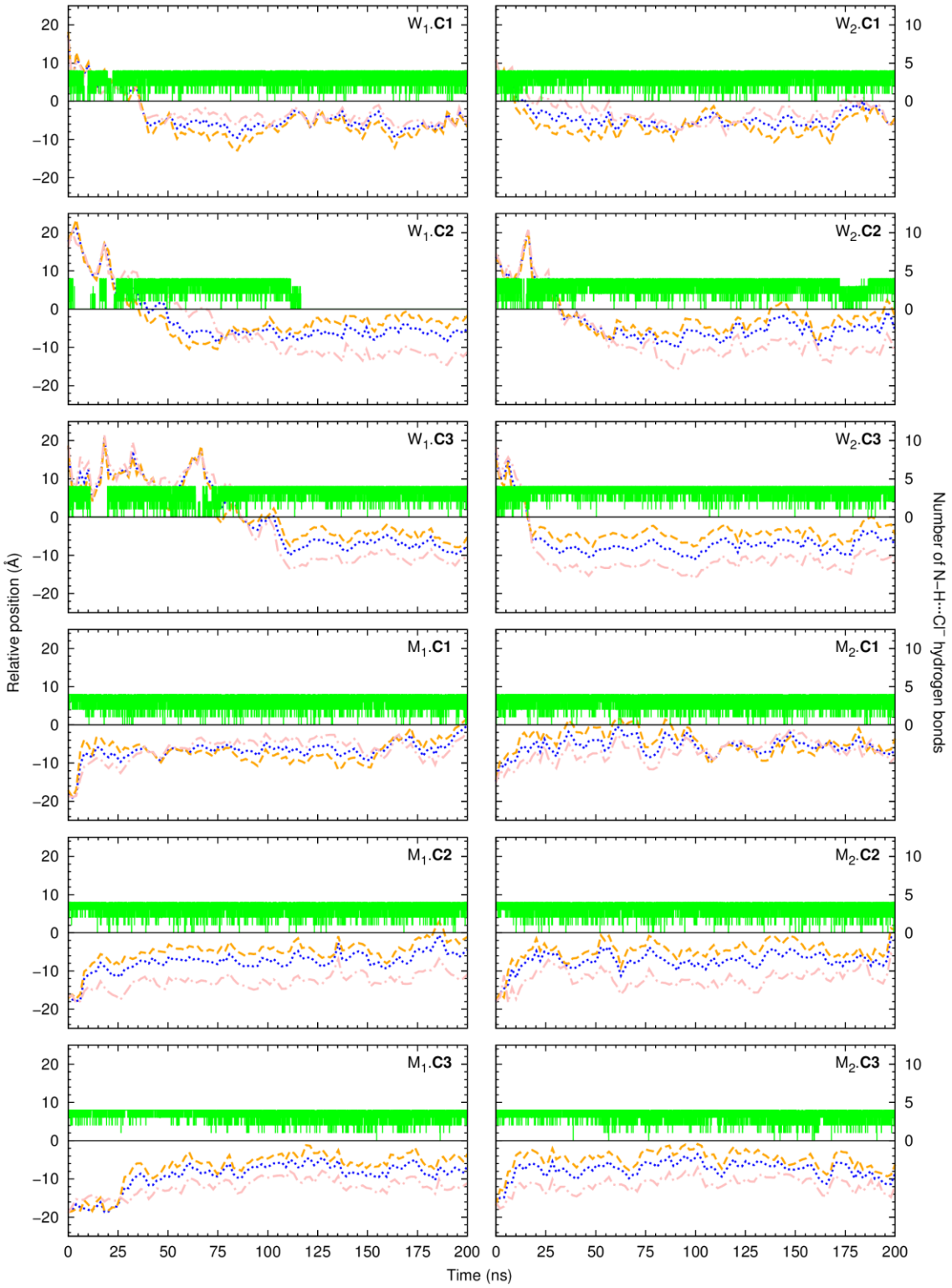

Figure S61. Evolution of the Sp$_{COM}$···P$_{int}$ (orange dashed line), N–H$_{COM}$···P$_{int}$ (blue dotted line) and Ph$_{COM}$···P$_{int}$ (pink dot-dashed line) distances throughout 200 ns for the MD runs of the C-series chloride complexes in scenarios W and M. The evolution of the number of N−H···Cl$^-$ hydrogen bonds is also plotted as a green line. The water/lipid interface is represented as a black line at z = 0 Å. Data were smoothed using Bézier curves.

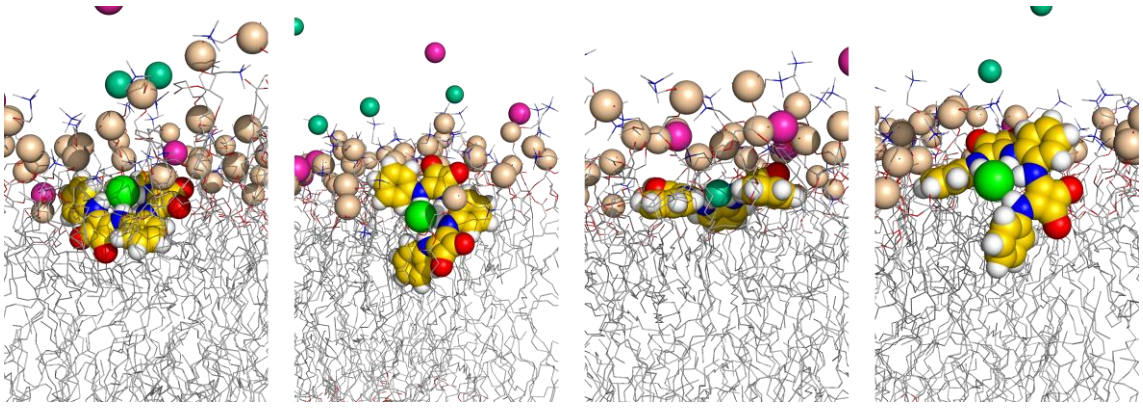

Figure S62. Illustrative snapshots depicting the orientations of the chloride complex of C1 throughout the MD simulations in scenario W. The squaramide derivative, sodium and chloride ions together with the phosphorus atoms are represented in spheres. The water molecules and the remaining atoms of the bilayer are shown as lines. The hydrogen atoms are shown in white, oxygen atoms in red, nitrogen atoms in blue, phosphorus atoms in wheat and carbon atoms in yellow (**C1**) or grey (phospholipids). The sodium ions are shown in pink and the chloride ions are shown in green (complex) or green marine (counter ions). The interaction of the internalised **C1** with the solvent molecules is emphasised with the depiction of water molecules within 3.5 Å from **C1** as spheres. The lipids' C–H bonds are omitted for clarity.

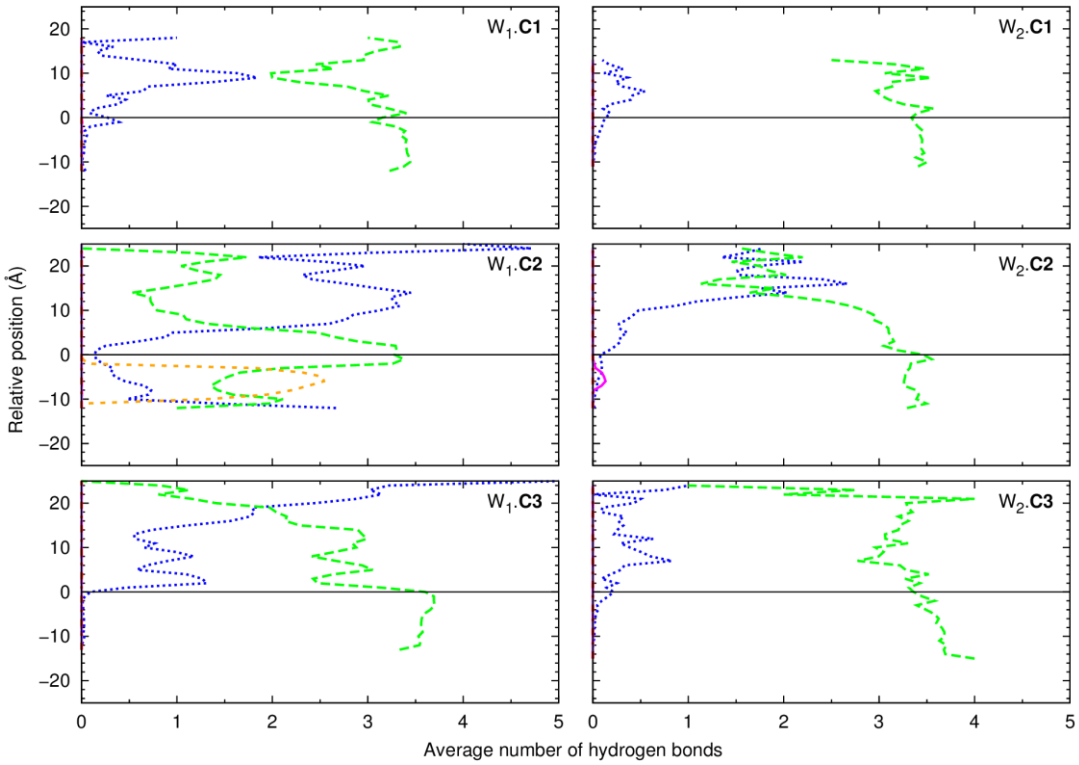

Figure S63. Average number of hydrogen bonds *vs.* the relative position of the COM of the C-series molecules in the MD runs carried out in scenario W. The following colour scheme was used for the interactions between the squaramide derivative and chloride ions (green dashed line), water molecules (blue dotted line), POPC head groups (orange short dashed line), and ester groups (magenta solid line for the *sn*-1 chains and purple dot-dashed line for the *sn*-2 chains). The water/lipid interface is represented as a black line at $z = 0$ Å. Data were smoothed using Bézier curves.

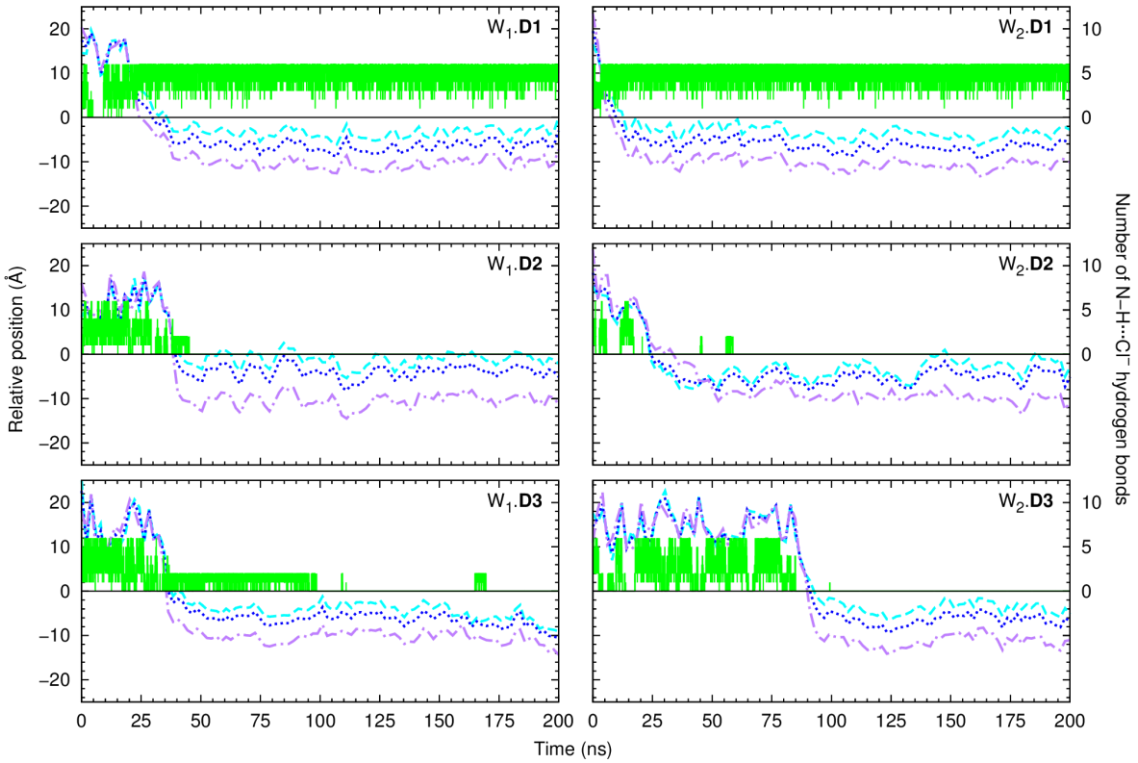

Figure S64. Evolution of the $N_{tren}\cdots P_{int}$ (cyan dashed line), $N–H_{COM}\cdots P_{int}$ (blue dotted line) and $Ph_{COM}\cdots P_{int}$ (purple dot-dashed line) distances throughout 200 ns for the MD runs of the D-series chloride complexes in scenario W. The evolution of the number of N–H···Cl^- hydrogen bonds is also plotted as a green line. The water/lipid interface is represented as a black line at z = 0 Å. Data were smoothed using Bézier curves.

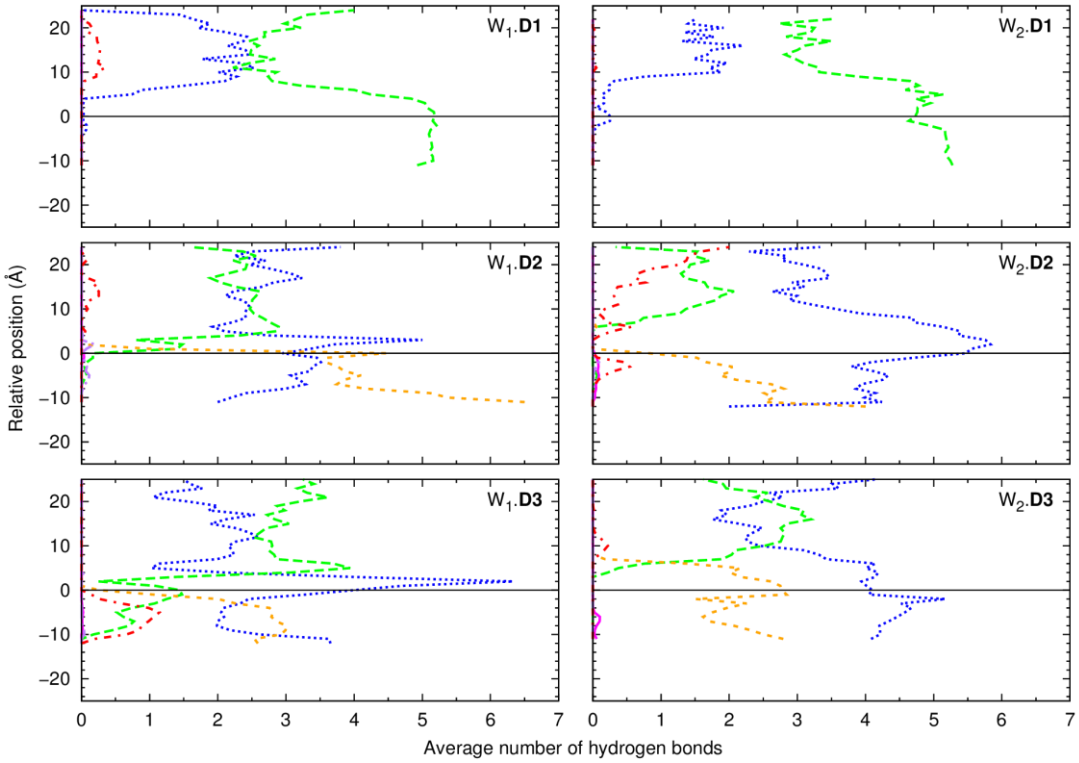

Figure S65. Average number of hydrogen bonds *vs.* the relative position of the COM of the D-series molecules in the MD runs carried out in scenario W. The following colour scheme was used for the interactions between the squaramide derivative and chloride ions (green dashed line), water molecules (blue dotted line), POPC head groups (orange short dashed line), and ester groups (magenta solid line for the *sn*-1 chains and purple dot-dashed line for the *sn*-2 chains). The water/lipid interface is represented as a black line at z = 0 Å. Data were smoothed using Bézier curves.

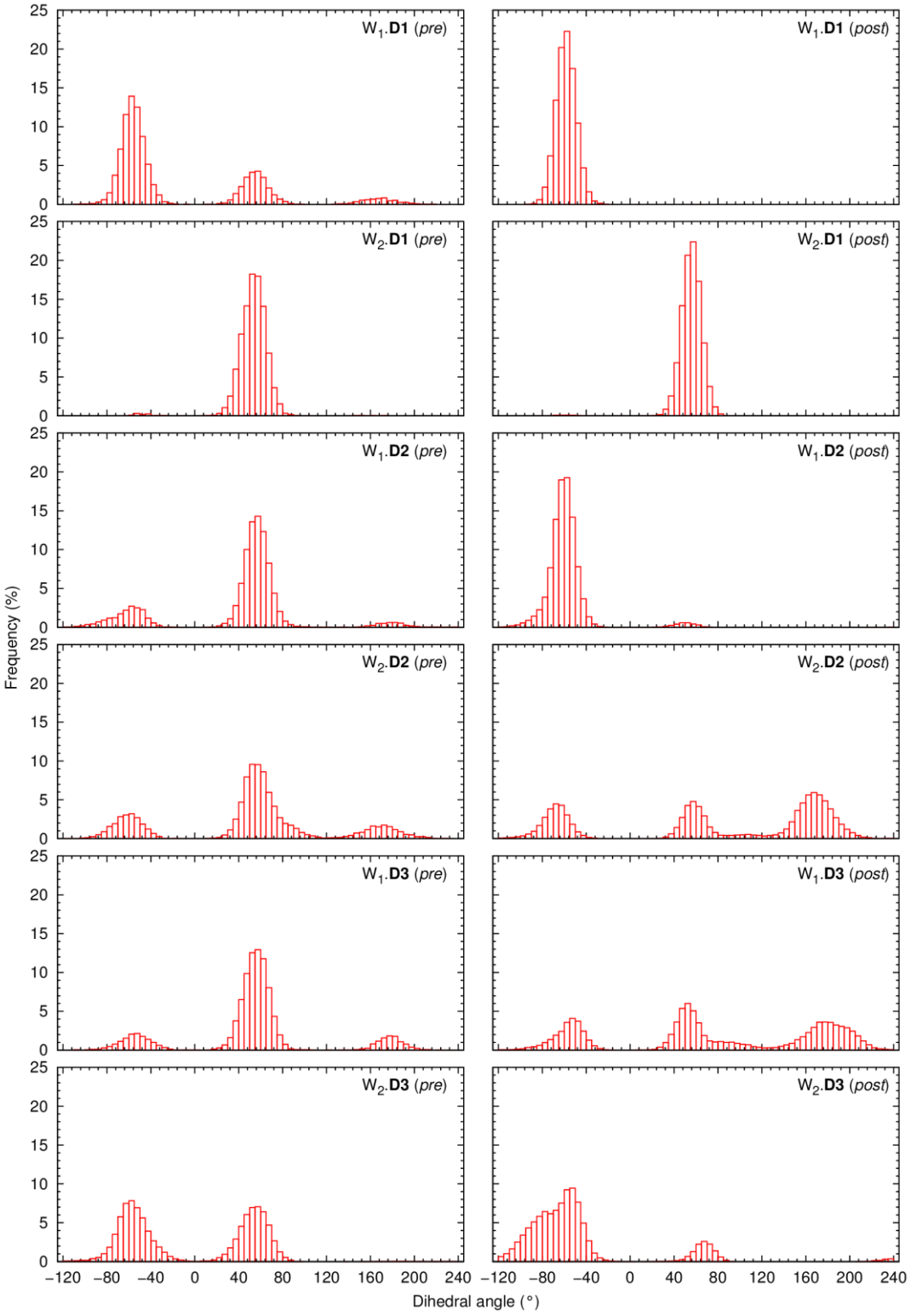

Figure S66. Frequency histograms showing the distribution of the three N-C-C-N torsion angles values of the D-series molecules in the MD simulations carried out in scenario W, before the interaction with the interface (*pre*) and after (*post*).

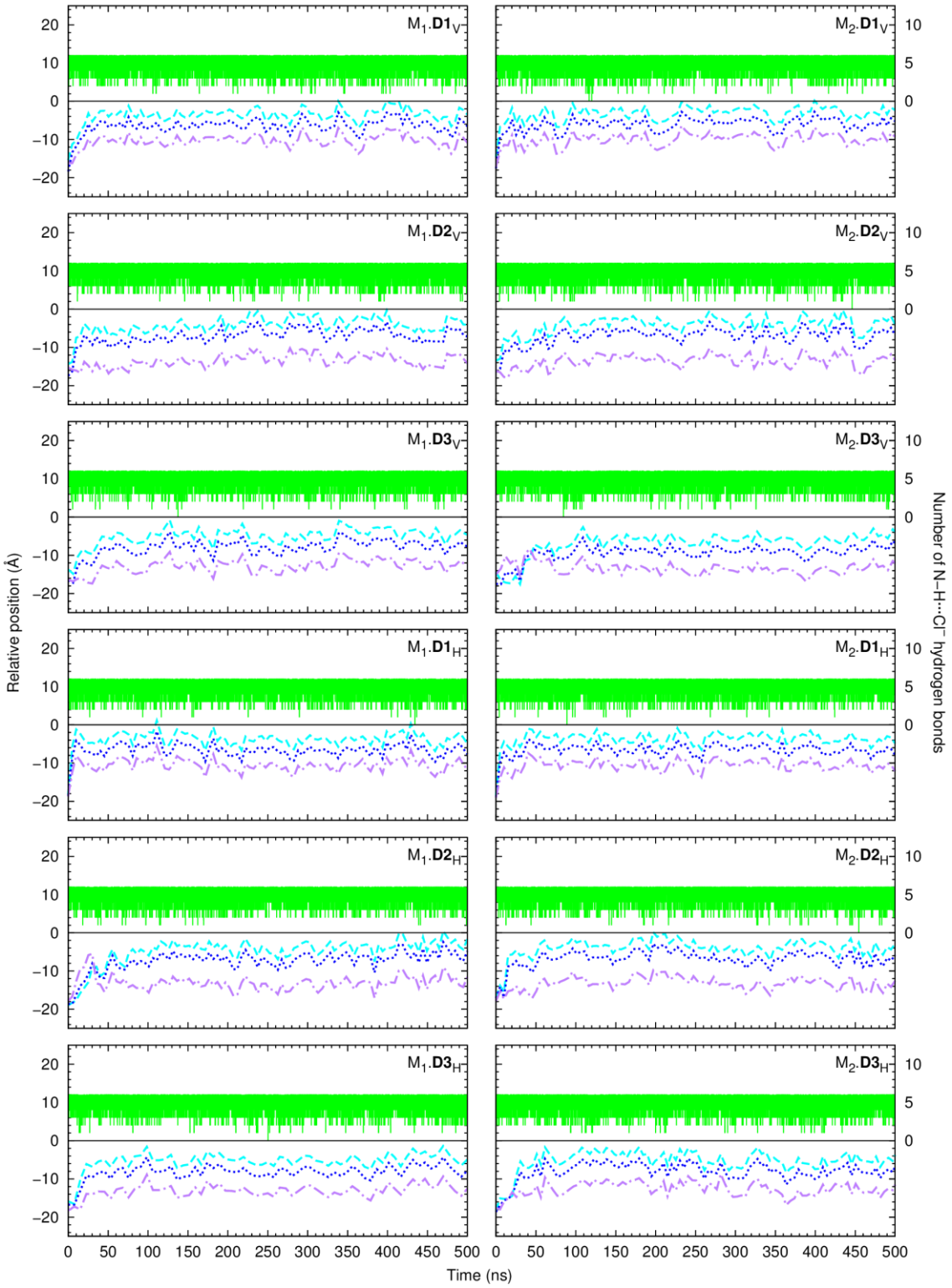

Figure S67. Evolution of the $N_{tren}\cdots P_{int}$ (cyan dashed line), $N\text{–}H_{COM}\cdots P_{int}$ (blue dotted line) and $Ph_{COM}\cdots P_{int}$ (purple dot-dashed line) distances throughout 500 ns for the MD runs of the D-series chloride complexes in scenario M in vertical or horizontal orientations. The evolution of the number of N−H···Cl^- hydrogen bonds is also plotted as a green line. The water/lipid interface is represented as a black line at z = 0 Å. Data were smoothed using Bézier curves.

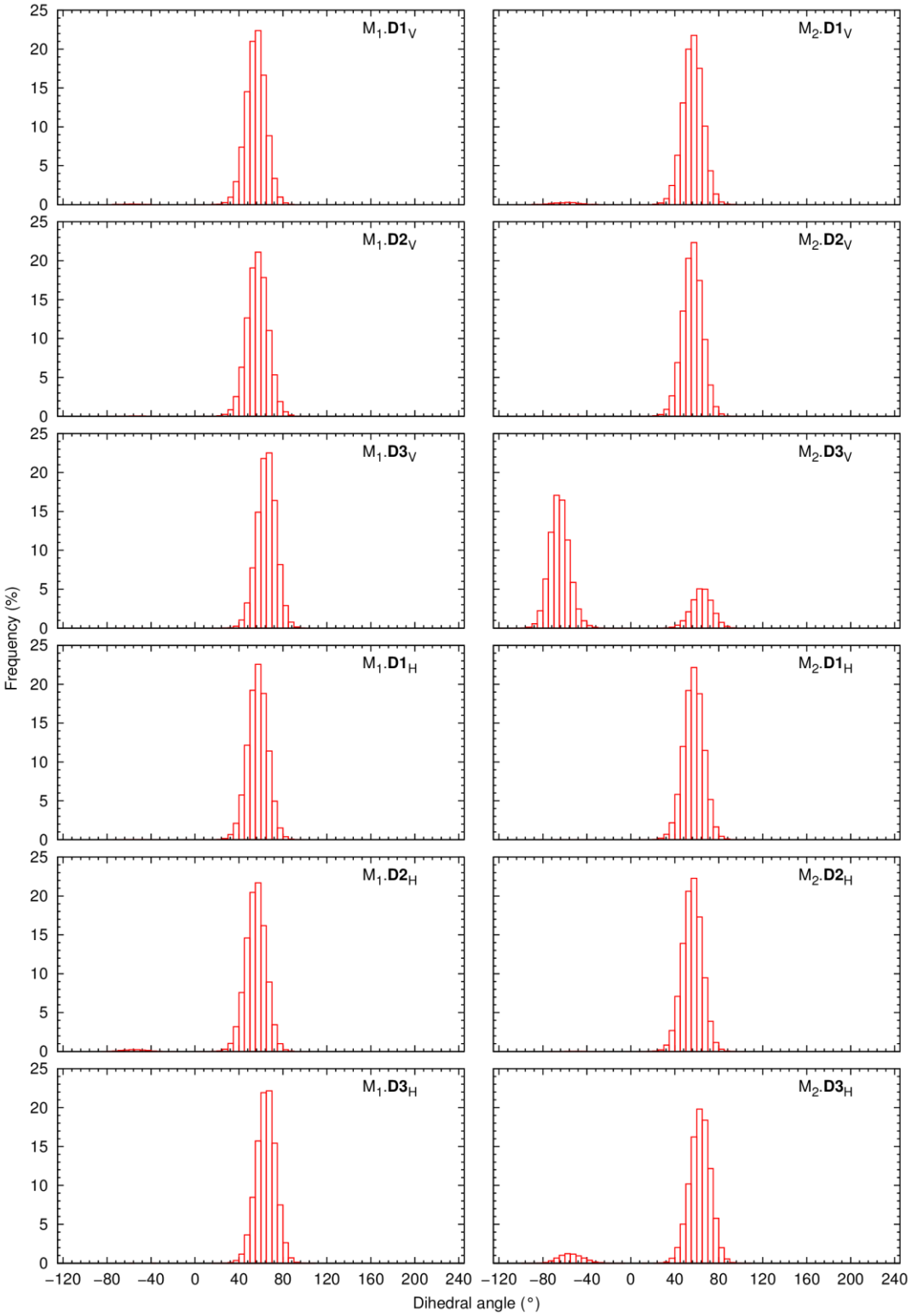

Figure S68. Frequency histograms showing the distribution of the three N-C-C-N torsion angles values of the D-series molecules in the MD simulations carried out in scenario M in vertical or horizontal orientation.

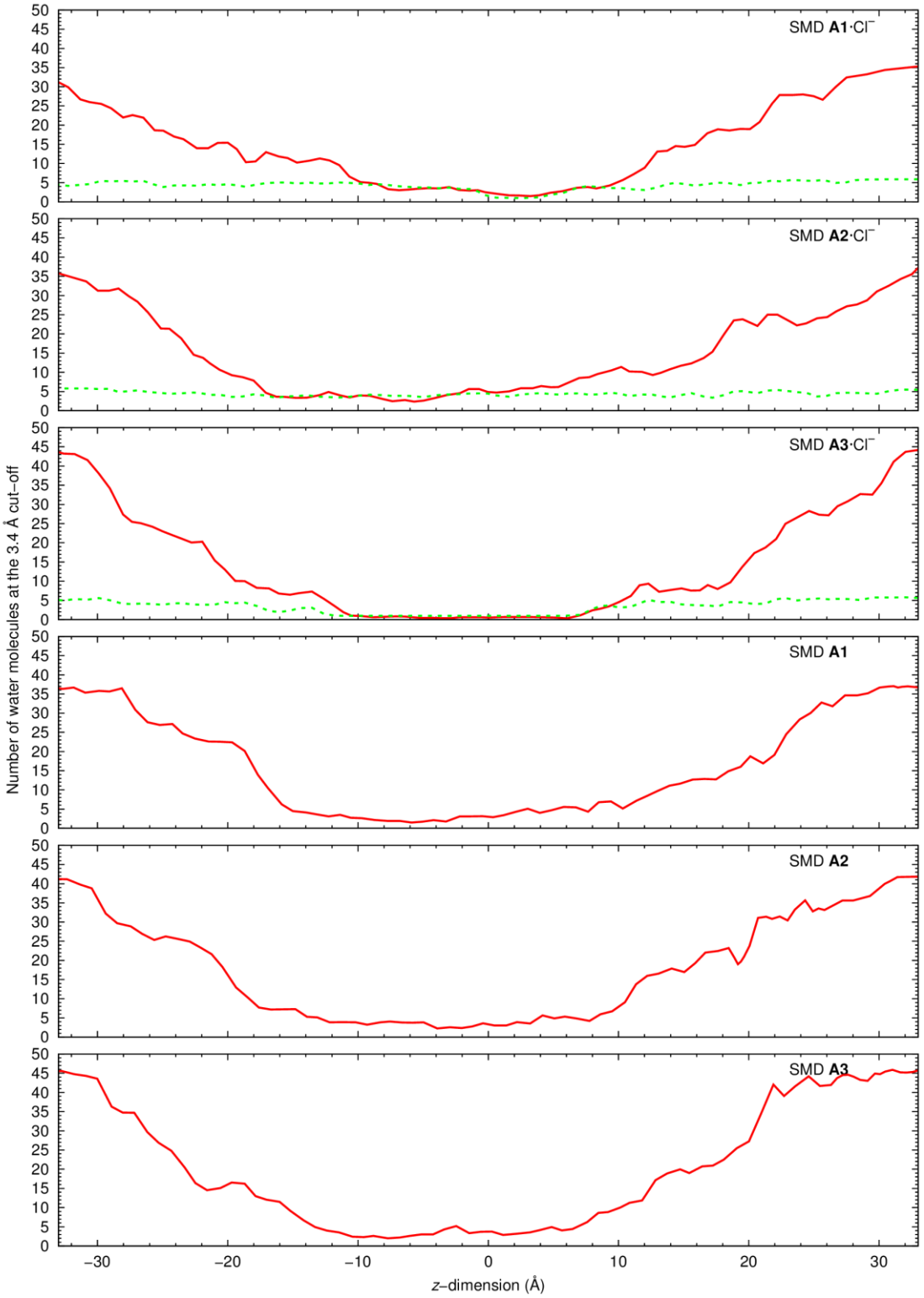

Figure S69. Variation of the number of water molecules within the solvation shell defined by a cut-off of 3.4 Å from the **A-series** molecules (red solid line) and their complexed chloride (green dashed line), in the SMD simulations of the the free or chloride complexed squaramides from one side of the POPC to the opposite side. Data were smoothed using Bézier curves.

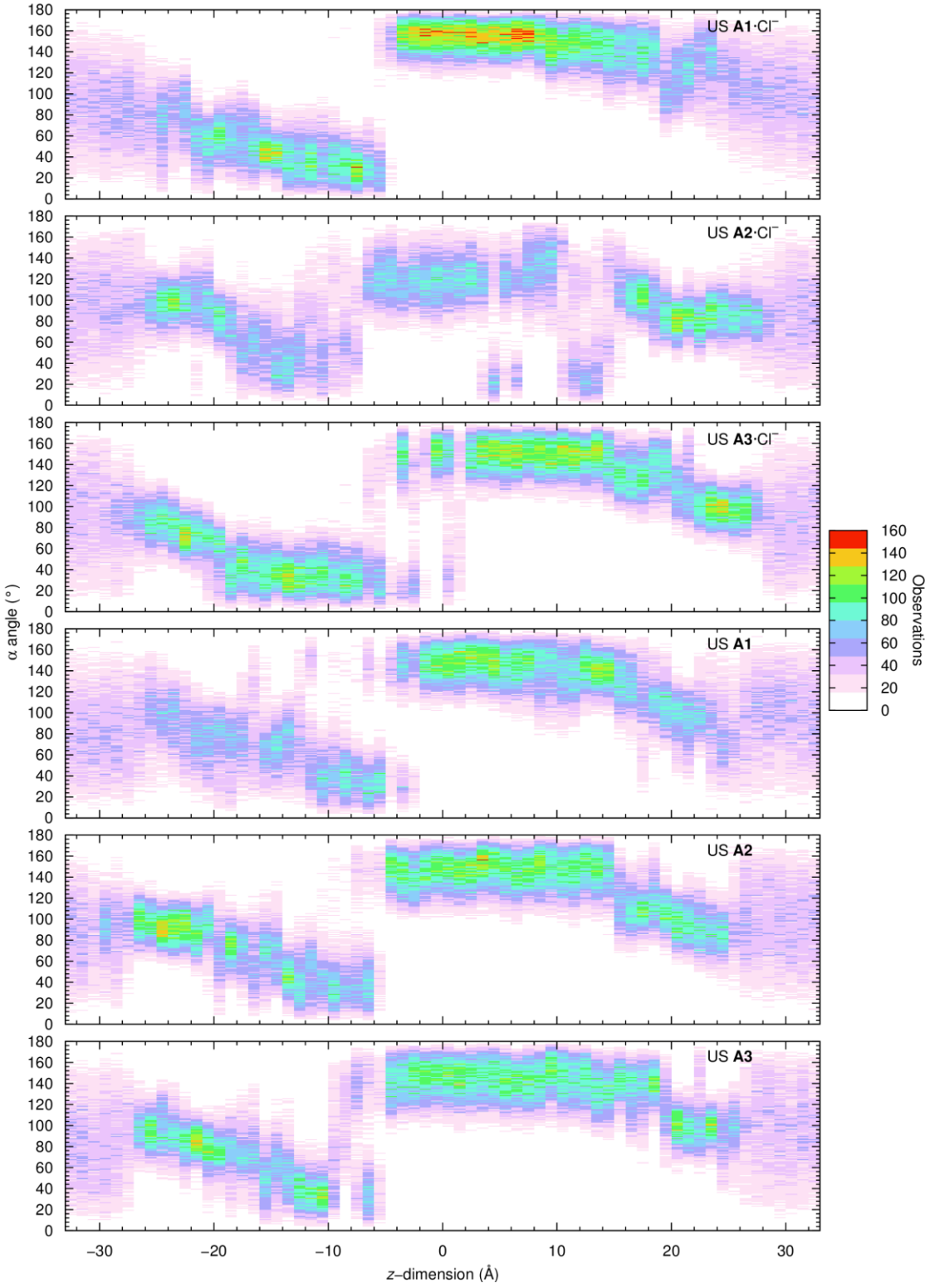

Figure S70. 2D histograms created from the α angle values monitored along the *z*-dimension positions of the chloride complexed or free A-series squaramides throughout the 67 independent US windows. The colour ranges from white (no occurrence) to red (several occurrences).

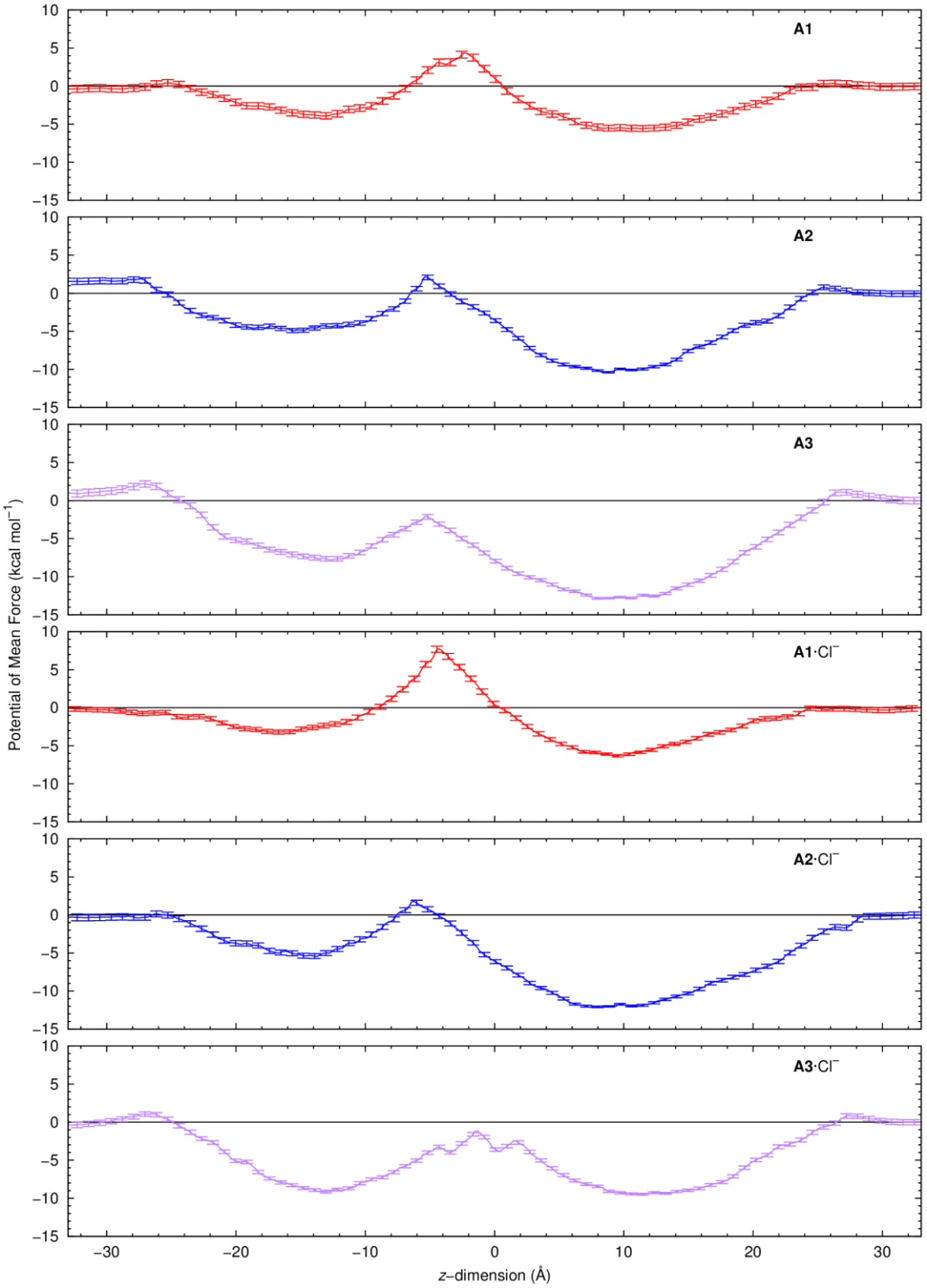

Figure S71. PMF as a function of the A-series free squaramides' distance to the membrane COM (z = 0 Å). The error bars correspond to the bootstrap errors calculated from 1000 Monte Carlo trials and are upscaled 20 times.

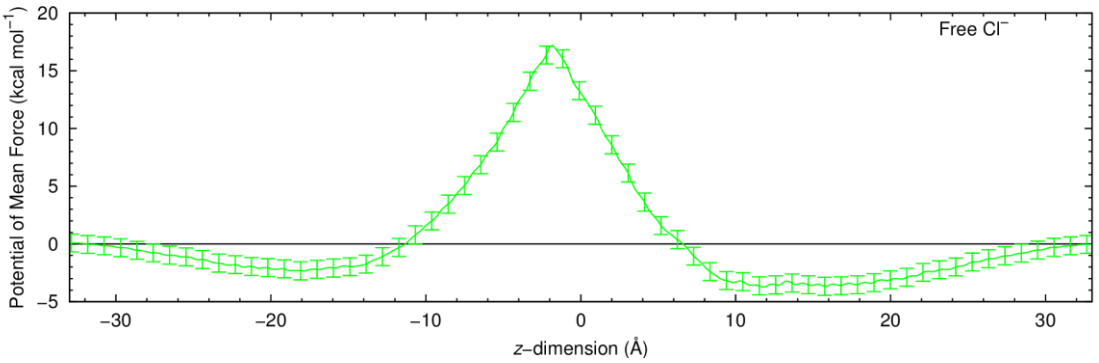

Figure S72. PMF as a function of the free chloride distance to the membrane COM (z = 0 Å). The error bars correspond to the bootstrap errors calculated from 1000 Monte Carlo trials.

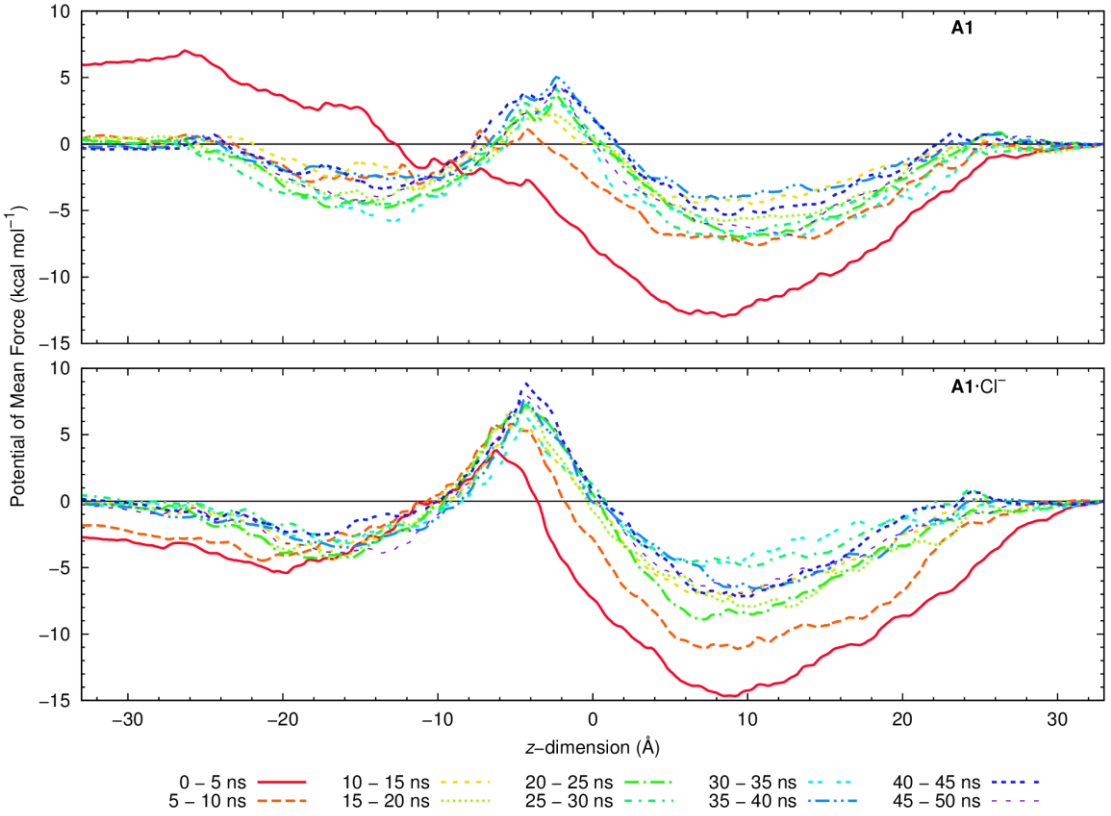

Figure S73. The equilibration and convergence of the umbrella sampling simulation windows were assessed in 5 ns intervals (coloured according to time period), taken through the trajectory and used to calculate the PMF of A1 and A1·Cl⁻. The PMF curves for **A1** and **A1**·Cl⁻ converged within the initial 30 ns.

S6.3. Additional Tables

Table S8. Hydrogen bond dimensions in the DFT optimised chloride complexes of the squaramide series, along with the N_{tren}–C–C–N torsion angles of the **D** subset.

Squaramide	N···Cl^- distance (Å)	N–H···Cl^- angle (°)	N_{tren}–C–C–N torsion angle (°)
A1	3.147 ; 3.147	175.2 ; 175.2	–
A2	3.120 ; 3.120	174.9 ; 174.9	–
A3	3.091 ; 3.091	174.4 ; 174.4	–
B1	3.168 ; 3.155	164.9 ; 172.9	–
B2	3.185 ; 3.130	163.9 ; 173.7	–
B3	3.173 ; 3.088	163.2 ; 173.3	–
C1	3.264 ; 3.257	177.0 ; 175.9	–
	3.264 ; 3.257	177.1 ; 175.9	–
C2	3.262 ; 3.249	176.1 ; 175.9	–
	3.262 ; 3.249	176.1 ; 175.9	–
C3	3.319 ; 3.199	169.2 ; 177.7	–
	3.235 ; 3.211	166.8 ; 175.1	–
D1	3.367 ; 3.297	163.9 ; 170.4	64.5
	3.359 ; 3.294	163.7 ; 170.6	64.9
	3.372 ; 3.300	163.2 ; 171.2	64.8
D2	3.376 ; 3.288	162.9 ; 170.3	64.3
	3.372 ; 3.285	162.6 ; 170.3	64.1
	3.368 ; 3.289	162.5 ; 170.6	64.5
D3	3.376 ; 3.262	161.7 ; 167.9	64.1
	3.381 ; 3.262	161.6 ; 169.2	64.0
	3.382 ; 3.264	160.7 ; 168.9	64.3

Table S9. Summary of the chloride binding (k_{ass}) and anion transport (k_{ini} and EC_{50}) properties of the twelve squaramide derivatives studied.

Squaramide	k_{ass} (M^{-1})[a]	k_{ini} (% s^{-1})[b]	EC_{50} (mol%)[b]
A1	240	0.1680	1.379
A2	433	2.1450	0.062
A3	602	1.4540	0.010
B1	119	0.0890	-
B2	729	0.3800	0.209
B3	776	0.8950	0.120
C1	871	0.9930	0.357
C2	4742	0.9800	0.085
C3	2259	0.6520	0.164
D1	821	0.0380	-
D2	8021	0.0021	-
D3	1627	0.0038	-

[a] Values from Table S6, only the association due to 1:1 squaramide:chloride complex formation is used (K_{11}), actual stoichiometry is more complex; [b] Values from Table S3, see description above.

Table S10. Average number of water molecules solvating the squaramide chloride complexes within the first solvation shell (cut-off = 3.4 Å).[a]

MD run	Squaramide derivative		Carbonyl groups[b]		Complexed chloride		N
	Avg ± SD	Range	Avg ± SD	Range	Avg ± SD	Range	
W'$_1$.**A1**	9.2 ± 3.6	[1.0 ; 23.0]	0.4 ± 0.8	[0.0 ; 8.0]	3.7 ± 1.0	[0.0 ; 8.0]	10000
W'$_1$.**A2**	7.2 ± 2.5	[1.0 ; 20.0]	0.2 ± 0.5	[0.0 ; 7.0]	3.9 ± 0.9	[1.0 ; 8.0]	10000
W'$_1$.**A3**	9.7 ± 10.4	[0.0 ; 56.0]	0.6 ± 1.9	[0.0 ; 14.0]	3.7 ± 1.1	[1.0 ; 8.0]	10000
W'$_1$.**B1**	8.3 ± 3.0	[1.0 ; 23.0]	0.5 ± 0.8	[0.0 ; 6.0]	3.5 ± 1.2	[1.0 ; 8.0]	10000
W'$_1$.**B2**	8.1 ± 3.1	[1.0 ; 29.0]	0.3 ± 0.7	[0.0 ; 6.0]	4.1 ± 1.1	[0.0 ; 9.0]	10000
W'$_1$.**B3**	10.1 ± 3.6	[1.0 ; 23.0]	0.4 ± 0.7	[0.0 ; 7.0]	3.8 ± 0.9	[1.0 ; 8.0]	10000
M'$_1$.**A1**	8.8 ± 3.0	[0.0 ; 22.0]	0.4 ± 0.8	[0.0 ; 6.0]	3.8 ± 1.0	[0.0 ; 7.0]	10000
M'$_1$.**A2**	6.6 ± 2.6	[0.0 ; 17.0]	0.1 ± 0.5	[0.0 ; 5.0]	3.5 ± 1.3	[0.0 ; 8.0]	10000
M'$_1$.**A3**	6.0 ± 2.7	[0.0 ; 19.0]	0.0 ± 0.3	[0.0 ; 5.0]	3.3 ± 1.0	[0.0 ; 7.0]	10000
M'$_1$.**B1**	10.0 ± 3.2	[0.0 ; 25.0]	0.5 ± 0.8	[0.0 ; 6.0]	4.2 ± 1.0	[1.0 ; 9.0]	10000
M'$_1$.**B2**	9.3 ± 2.7	[1.0 ; 21.0]	0.6 ± 0.8	[0.0 ; 6.0]	4.1 ± 0.9	[1.0 ; 8.0]	10000
M'$_1$.**B3**	8.9 ± 3.0	[1.0 ; 21.0]	0.4 ± 0.6	[0.0 ; 5.0]	3.9 ± 1.0	[1.0 ; 8.0]	10000
M$_1$.**C1**	11.0 ± 3.0	[1.0 ; 26.0]	1.6 ± 1.7	[0.0 ; 11.0]	2.7 ± 0.8	[0.0 ; 8.0]	10000
M$_2$.**C1**	10.3 ± 3.3	[1.0 ; 25.0]	1.4 ± 1.4	[0.0 ; 10.0]	2.5 ± 0.9	[0.0 ; 6.0]	10000
M$_1$.**C2**	9.5 ± 3.5	[0.0 ; 25.0]	2.5 ± 1.9	[0.0 ; 14.0]	2.2 ± 0.9	[0.0 ; 6.0]	10000
M$_2$.**C2**	10.0 ± 2.8	[2.0 ; 22.0]	2.0 ± 1.6	[0.0 ; 11.0]	2.5 ± 0.9	[0.0 ; 6.0]	10000
M$_1$.**C3**	8.3 ± 2.9	[0.0 ; 20.0]	1.7 ± 1.3	[0.0 ; 10.0]	2.1 ± 0.9	[0.0 ; 5.0]	10000
M$_2$.**C3**	10.3 ± 3.2	[1.0 ; 24.0]	2.6 ± 1.8	[0.0 ; 11.0]	2.1 ± 0.8	[0.0 ; 7.0]	10000
M$_1$.**D1$_H$**	8.6 ± 2.9	[1.0 ; 23.0]	4.4 ± 2.2	[0.0 ; 16.0]	0.1 ± 0.3	[0.0 ; 2.0]	40000
M$_2$.**D1$_H$**	8.8 ± 2.9	[1.0 ; 23.0]	4.2 ± 2.2	[0.0 ; 16.0]	0.0 ± 0.1	[0.0 ; 1.0]	40000
M$_1$.**D1$_V$**	10.0 ± 3.4	[2.0 ; 28.0]	4.6 ± 2.4	[0.0 ; 19.0]	0.2 ± 0.4	[0.0 ; 3.0]	40000
M$_2$.**D1$_V$**	10.7 ± 3.0	[2.0 ; 25.0]	4.9 ± 2.4	[0.0 ; 17.0]	0.1 ± 0.3	[0.0 ; 3.0]	40000
M$_1$.**D2$_H$**,	8.8 ± 3.0	[1.0 ; 26.0]	4.0 ± 2.1	[0.0 ; 15.0]	0.0 ± 0.1	[0.0 ; 2.0]	40000
M$_2$.**D2$_H$**	9.9 ± 2.8	[1.0 ; 23.0]	4.3 ± 2.1	[0.0 ; 17.0]	0.0 ± 0.2	[0.0 ; 2.0]	40000
M$_1$.**D2$_V$**	10.1 ± 2.7	[2.0 ; 24.0]	4.4 ± 2.1	[0.0 ; 16.0]	0.1 ± 0.3	[0.0 ; 2.0]	40000
M$_2$.**D2$_V$**	9.2 ± 2.8	[1.0 ; 25.0]	3.9 ± 2.1	[0.0 ; 19.0]	0.0 ± 0.2	[0.0 ; 2.0]	40000
M$_1$.**D3$_H$**	9.1 ± 3.4	[0.0 ; 27.0]	4.1 ± 2.2	[0.0 ; 17.0]	0.2 ± 0.4	[0.0 ; 2.0]	40000
M$_2$.**D3$_H$**	10.1 ± 3.1	[1.0 ; 28.0]	4.6 ± 2.4	[0.0 ; 17.0]	0.0 ± 0.1	[0.0 ; 2.0]	40000
M$_1$.**D3$_V$**	8.6 ± 3.7	[0.0 ; 25.0]	4.2 ± 2.3	[0.0 ; 17.0]	0.1 ± 0.3	[0.0 ; 2.0]	40000
M$_2$.**D3$_V$**	8.5 ± 3.1	[1.0 ; 26.0]	3.7 ± 2.1	[0.0 ; 16.0]	0.0 ± 0.1	[0.0 ; 1.0]	40000

[a] These parameters were evaluated throughout the last 100 ns of simulation time for the **A**-, **B**- and **C**-series, and throughout the last 400 ns for the **D**-series; [b] Sum of the number of water molecules around the independent C=O groups.

S6.4. Extended discussion

Quantum Calculations

The **A**-series chloride complexes exhibit symmetric structures, with equal distance N–H···Cl^- hydrogen bonding dimensions, which are similar to those found in the crystal structures of these complexes.[1] On the other hand, the C–C covalent bond lengths within the squaramide motif are in close agreement with the crystallographic ones, apart from the C–C distance between the carbonyl groups, which is 0.031 Å longer in the DFT optimised structures. A detailed crystal packing analysis of these three chloride complexes shows the existence of intermolecular C−H···O=C bonding contacts which can induce slight distortions on the bond lengths and angles within the squaramide motif (see section S6.6).[1]

For the **B**-series, due to its asymmetric structure, the lengths of the N–H···Cl^- hydrogen bonds are slightly different, with the N–H unit closer to the phenyl substituent establishing the stronger interaction, as it always has the shorter length and the more linear angle. Concerning the **C**-series with the bis-squaramide units, the two N−H binding units adjacent to the peripheral aromatic substituents have shorter N···Cl^- distances than the ones near the central bridging 1,2-phenylene moiety. In the optimised structures of the **D** tripodal complexes, the chloride ion is surrounded by the three-squaramide moieties, establishing six hydrogen bonds, with the three N···Cl^- distances adjacent to the phenyl substituents being systematically shorter than the remaining ones. Moreover, the three N_{tren}–C–C–N torsion angles, with values of *ca.* 64.4°, are consistent with a tripodal *ggg* conformation.[50]

Molecular Dynamics simulations with chloride complexes of tripodal squaramides D

To evaluate the conformational changes that the **D** tripodal molecules experience during the passive diffusion process, the evolution of the three N_{tren}–C–C–N torsion angles was monitored throughout the 200 ns MD simulations. When the three individual torsion angles assume values of *ca.* ±60° the squaramide derivative adopts a typical tripodal shape (a *ggg* conformation – *vide supra*). Moreover, if any N_{tren}–C–C–N torsion angle has a value closer to ±180°, the tripodal shape is lost and three non-tripodal conformations are possible: *ggt*, *gtt* and *ttt*, regardless of the torsion angle position and the angle value. The N_{tren}–C–C–N torsion angles for the MD simulations with the tripodal molecules were histogrammed before (*pre*) and after (*post*) internalisation and are plotted in Figure S66. These parameters can be related with hydrogen bonds established between the N−H binding units and the surrounding water molecules, phosphate head groups or carbonyl moieties as follows:

The *pre* internalisation histogram of W_1.**D1** exhibits three well defined peaks (centred at −60, 60 and 180°), consistent with the existence of a dominant *ggg* conformation, followed by a transitory

ggt one, resulting from the replacement of the complexed chloride ion by water molecules. In contrast, the post internalisation histogram only shows a single peak (centred at −60°), undoubtedly corresponding to **D1** in tripodal *ggg* shape complexed with chloride. In the second MD run with **D1**, the anion complex is preserved throughout the whole simulation as well as the *ggg* conformation (see Figure S65 and Figure S66).

Likewise the simulation W_1.**D1**, the internalisation of **D2** in simulation W_1.**D2** is preceded by the replacement of the complexed anion by water molecules with the occurrence of *ggg* and *ggt* conformations. However, after internalisation, the binding pocket room is shared by water molecules and a phosphate head group, as shown in Figure S65. Moreover, when the number of hydrogen bonds to the water molecules increases, the interactions with the phosphate head groups decrease and *vice-versa*, although the *ggg* conformation is maintained until the end of the simulation, as indicated by the *post* histogram in Figure S66, with a major peak at −60° and a smaller one at 60°. In the second MD run, **D2** presents a more intriguing conformational behaviour. Indeed, after the definitive anion departure, the water molecules, carbonyl moieties and phosphate groups occupy the binding units as the squaramide derivative penetrates the bilayer, resulting in a new *gtt* conformation for a substantial simulation length (see Figure S65 and Figure S66). Afterwards, this conformation is definitively converted into *ggt*, with the N−H binding units interacting only with water molecules and phosphate head groups.

After anion release, **D3** presents different conformational behaviours along the simulation length of the two runs (see Figure S66). Remarkably, in the first MD run, both before and after the internalisation, **D3** assumes mainly a *ggt* conformation followed by a *ggg*. During the passive diffusion, the number of hydrogen bonds to the chloride ions decreases as the receptor binds water molecules and POPC head groups. Concomitantly, the carbonyl moieties of the squaramide motifs are hydrogen bonded by the N−H of adjacent binding units. Noteworthy, in the second MD replicate, the number of hydrogen bonding interactions indicates that **D3** recognises chloride ions and water molecules, with the maintenance of the *ggg* conformation (see Figure S65 and Figure S66). With the internalisation of **D3**, the anion complex is definitely disrupted, with the binding sites recognising water molecules as well as phosphate head groups, maintaining the *ggg* conformation.

S6.5. Supplementary Movies' captions

Movie S1. Diffusion of the chloride complex of **A2** throughout the MD simulation W_1.**A2**, between the 91st and 110th ns. The squaramide derivative, sodium and chloride ions together with the phosphorus atoms are represented in spheres. The remaining atoms of the bilayer are shown as lines. The hydrogen at-oms are shown in white, oxygen atoms in red, nitrogen atoms in blue, fluorine atoms in light blue, phosphorus atoms in wheat and carbon atoms in yellow (**A2**) or grey (phospholipids). The sodium ions are shown in pink and the chloride ions are shown in green (complex) or green

marine (counter ions). The interaction of the internalised **A2** with the solvent molecules is emphasised with the depiction of water molecules within 3.5 Å from **A2** as spheres. Most water molecules and the lipids' C–H bonds are omitted for clarity.

Movie S2. Diffusion of the chloride complex of **A3** throughout the MD simulation M_1.**A3**, between the 151st and 200th ns. Remaining details as given in Movie S1.

Movie S3. Diffusion of the chloride complex of **A3** throughout the MD simulation M_1.**A3**. Remaining details as given in Movie S1.

Movie S4. Diffusion of the chloride complex of **D3** throughout the MD simulation M_1.$\mathbf{D3}_H$, between the 1st and 200th ns. Remaining details as given in Movie S1.

Movie S5. Spatial dispositions assumed by the chloride complex of **A2** throughout the 67 US windows (7 frames/window, extracted during the sampling period). Remaining details as given in Movie S1.

S6.6. Force field parameterisation of the squaramide core

The preliminary gas phase MM optimisation of the twelve squaramide derivatives with GAFF default force field parameters and atom types, as given in Scheme S1 and Table S11, led to shorter cc-cd distances than in the crystal structures, while the c-c distances were longer. Furthermore, these structures were also optimised at the B3LYP/6-31G* level (in agreement with the GAFF current development), leading to bond lengths like those obtained *via* MM optimisations with default GAFF parameters. On the other hand, the analysis of the crystal structures revealed that most of these molecules are self-assembled, typically *via* N-H···O=C hydrogen bonding interactions, or interacting with solvent molecules or anion guests. These intermolecular interactions have a structural impact on the cc-cd and c-c distances discussed above. In these circumstances, given that the MD simulations take place in condensed phase (a membrane system composed of POPC lipids and water molecules), we decided to parameterise the squaramide core. The equilibrium bond lengths (r_{eq}) and equilibrium bond angles (θ_{eq}) were taken from the average distances and angles, respectively, assessed from 48 X-ray single crystal structures deposited with CCDC,[39] and three unpublished X-ray single crystal structures. In these 51 single crystal structures, there are 60 independent molecules, with 62 squaramide binding motifs that were used in this parameterisation effort.

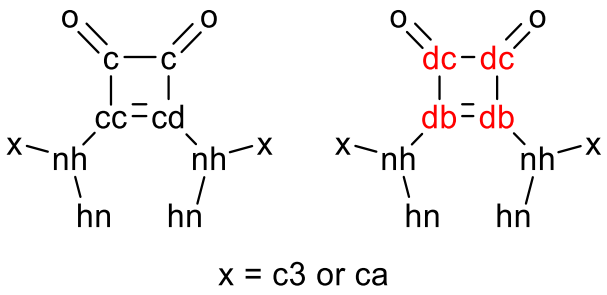

Scheme S1. Schematic representation of the squaramide moiety with the atom types: left – default GAFF atom types; right – new atom types (in red) created for this specific parameterisation.

New atom types, as identified in Scheme S1, were created, with non-bonded and torsion angles parameters of the GAFF atom types cc/cd and c, but with bond lengths and bond angles force constants calculated in agreement with GAFF,[36, 37] from the crystallographic data. The newly determined equilibrium bond lengths and bond angles are listed in Table S11, along with the corresponding force constants (K_r and K_θ, respectively). Concerning the C-C bonds on the squaramide motif, the new bond length parameters assessed from the crystal structures are much closer to each other than the corresponding GAFF default parameters (1.408, 1.496 and 1.470 Å *vs* 1.371, 1.550 and 1.462 Å). Moreover, the X-ray derived bond angles of the squaramide core are closer to the 90° of a right angle then the GAFF ones, which are much more obtuse (88.26 and 91.70° *vs* 111.67 and 121.42°).

Table S11. Force field parameters for the squaramide moiety: default GAFF parameters and X-ray derived parameters.

GAFF default parameters			X-ray derived parameters		
Bond lengths					
Parameter	r_{eq} (Å)	K_r (kcal·mol^{-1}·Å^{-2})	*Parameter*	r_{eq} (Å)	K_r (kcal·mol^{-1}·Å^{-2})
cc-cd	1.371	504.00	db-db	1.408	447.30
c -c	1.550	290.10	dc-dc	1.496	340.50
cc-c cd-c	1.462	377.40	db-dc	1.470	368.46
c -o	1.214	648.00	dc-o	1.224	624.81
cc-nh cd-nh	1.364	449.00	db-nh	1.334	496.30
nh-hn	1.014	401.20	nh-hn[a]	1.014	401.20
ca-nh	1.364	449.00	ca-nh[a]	1.364	449.00
c3-nh	1.458	332.70	c3-nh[a]	1.458	332.70
Bond angles					
Parameter	θ_{eq} (°)	K_θ (kcal·mol^{-1}·rad^{-2})	*Parameter*	θ_{eq} (°)	K_θ (kcal·mol^{-1}·rad^{-2})
c -c -cc c -c -cd	111.67	64.02	dc-dc-db	88.26	73.24
c -cc-cd c -cd-cc	121.42	65.25	dc-db-db	91.70	73.99
cd-cc-nh cc-cd-nh	123.89	68.69	db-db-nh	132.04	66.27
c -cc-nh c -cd-nh	118.57	67.80	dc-db-nh	136.21	63.60
o -c -c	120.99	67.16	o -dc-dc	135.36	65.15
o -c -cc o -c -cd	125.71	68.91	o -dc-db	136.35	65.75
cc-nh-hn cd-nh-hn	117.16	48.86	db-nh-hn[b]	117.16	49.79
cc-nh-ca cd-nh-ca	129.77	63.77	db-nh-ca[b]	129.77	64.46
cc-nh-c3 cd-nh-c3	119.23	64.17	db-nh-c3[b]	119.23	64.75

[a] Parameters taken directly from GAFF; [b] Bond angle and nh-hn, nh-ca and nh-c3 bond lengths taken directly from GAFF.

To further validate this parameterisation effort, both GAFF default and the newly developed parameters were used to undertake gas phase MM optimisations on the 60 independent molecules

obtained from the 51 single crystal structures used to derive the X-ray parameters. At the time that parameterisation took place, the crystal structures of **C1** were yet not available. The Root-Mean-Square Deviation (RMSD) values listed in Table S12 were calculated between the X-ray crystal structures and the MM minimised structures, with either set of parameters and standard RESP atomic charges calculated in agreement with GAFF development.[36, 37]

Table S12. RMSD values calculated between X-ray crystal and MM optimised structures with RESP atomic charges and two force fields for the squaramide core.

CCDC RefCODE	Reference	GAFF default parameters		X-ray derived parameters	
		Whole Molecule[a]	Squaramide core[b]	Whole Molecule[a]	Squaramide core[b]
AKOFIQ[c]	51	0.571	0.073	0.549	0.056
		0.588	0.047	0.568	0.036
AKOFOW	51	0.619	0.031	0.608	0.027
AKOGAJ	51	0.237	0.042	0.218	0.033
AKOGEN[c]	51	0.400	0.030	0.381	0.015
		1.209	0.039	1.196	0.044
CIBQIN	52	0.162	0.058	0.199	0.052
CIPYIL	53	1.306	0.050	0.467	0.037
CIPYOR	53	0.873	0.049	0.366	0.022
CIPYUX	53	0.846	0.062	0.468	0.041
CIPZAE	53	1.070	0.047	0.439	0.018
CIPZEI[c]	53	1.020	0.047	0.628	0.043
		1.027	0.043	0.668	0.031
DICQIQ	54	0.059	0.044	0.047	0.039
EWOCAV	55	0.236	0.066	0.353	0.062
EWOCAV01	55	0.238	0.069	0.355	0.064
FATSUP	56	0.307	0.038	0.171	0.063
FAWZAG	1	0.892	0.061	0.740	0.031
FAWZUA	1	0.366	0.067	0.294	0.041
FAXBEN	1	0.649	0.128	0.730	0.124
FAXBUD	1	0.309	0.062	0.245	0.029
FAXCAK	1	0.482	0.062	0.422	0.032
FAXCEO	1	0.328	0.061	0.283	0.031
FAXCIS[c]	1	0.812	0.060	1.012	0.073
		0.812	0.077	0.979	0.081
GAHMEH	57	0.177	0.060	0.272	0.055
GAQFAH	58	0.571	0.039	0.539	0.043
LANVOM	59	0.732	0.051	0.709	0.033

CCDC RefCODE	Reference	GAFF default parameters		X-ray derived parameters	
		Whole Molecule[a]	Squaramide core[b]	Whole Molecule[a]	Squaramide core[b]
MUYYIP	60	0.470	0.066	0.386	0.038
MUYYOV[c]	60	0.429	0.104	0.351	0.085
		0.552	0.068	0.351	0.031
NANQUO	61	0.247	0.048	0.310	0.063
NANQUO02[c]	62	0.190	0.042	0.258	0.063
		0.244	0.050	0.311	0.078
NIZXIE	63	1.155	0.100	1.124	0.031
NIZXOK	63	0.140	0.048	0.187	0.045
NOLRIQ	64	1.930	0.075	1.942	0.067
OMUKAJ	65	0.656	0.072	0.592	0.047
OMUKEN	65	0.322	0.040	0.477	0.033
QORQIY	66	0.693	0.047	0.725	0.067
RAKZAG	67	0.622	0.043	0.602	0.028
REPGIE	68	0.474	0.088	0.840	0.069
SEWFAD	69	0.308	0.074	0.385	0.080
UBABAC	70	0.985	0.053	2.118	0.052
UBABAC01	70	0.675	0.040	0.823	0.057
UBADUY	71	0.321	0.034	0.336	0.047
VARDOJ	72	0.282	0.042	0.270	0.043
WECCAK	73	0.040	0.034	0.067	0.039
WECCEO	73	0.058	0.053	0.054	0.049
WECCIS	73	0.055	0.038	0.035	0.035
WELXUI[d]	3		0.052		0.048
		0.281	0.030	0.452	0.031
			0.035		0.032
XOPWEF	74	0.247	0.039	0.272	0.040
XOPWEF01	74	0.231	0.040	0.310	0.047
XUFMER[e]	75	0.581	0.065	0.636	0.060
		0.750	0.047	0.798	0.033
		0.770	0.044	0.736	0.028
Entry 49	[f]	0.788	0.043	1.033	0.038
Entry 50[c]	[f]	0.151	0.051	0.136	0.021
		0.151	0.054	0.130	0.024
Entry 51	[f]	0.292	0.049	0.277	0.032
Mean ± SD		0.533 ± 0.366	0.054 ± 0.018	0.520 ± 0.391	0.046 ± 0.019

[a] Only the non-hydrogen atoms were considered; [b] "Squaramide core" stands for the four carbon atoms, the two oxygen atoms and the two nitrogen atoms identified in Scheme S1; [c] The asymmetric unit contains two independent molecules; [d] This molecule contains three squaramide binding units; [e] The asymmetric unit contains three independent molecules; [f] Unpublished.

S7. REFERENCES

1. N. Busschaert, I. L. Kirby, S. Young, S. J. Coles, P. N. Horton, M. E. Light and P. A. Gale, *Angew. Chem. Int. Ed. Engl.*, 2012, **51**, 4426-4430.
2. N. Busschaert, S. H. Park, K. H. Baek, Y. P. Choi, J. Park, E. N. W. Howe, J. R. Hiscock, L. E. Karagiannidis, I. Marques, V. Felix, W. Namkung, J. L. Sessler, P. A. Gale and I. Shin, *Nat. Chem.*, 2017, **9**, 667-675.
3. C. Jin, M. Zhang, L. Wu, Y. Guan, Y. Pan, J. Jiang, C. Lin and L. Wang, *Chem. Commun.*, 2013, **49**, 2025-2027.
4. Y. Liu, Y. Qin and D. Jiang, *Analyst*, 2015, **140**, 5317-5323.
5. C. Jin, M. Zhang, C. Deng, Y. F. Guan, J. Gong, D. R. Zhu, Y. Pan, J. L. Jiang and L. Y. Wang, *Tetrahedron Lett.*, 2013, **54**, 796-801.
6. G. M. Sheldrick, *Acta Crystallogr. A*, 2008, **64**, 112-122.
7. N. Busschaert, R. B. Elmes, D. D. Czech, X. Wu, I. L. Kirby, E. M. Peck, K. D. Hendzel, S. K. Shaw, B. Chan, B. D. Smith, K. A. Jolliffe and P. A. Gale, *Chem Sci*, 2014, **5**, 3617-3626.
8. A. V. Koulov, T. N. Lambert, R. Shukla, M. Jain, J. M. Boon, B. D. Smith, H. Li, D. N. Sheppard, J. B. Joos, J. P. Clare and A. P. Davis, *Angew. Chem. Int. Ed. Engl.*, 2003, **42**, 4931-4933.
9. F. G. Riddell and M. K. Hayer, *Biochim. Biophys. Acta*, 1985, **817**, 313-317.
10. N. Busschaert, M. Wenzel, M. E. Light, P. Iglesias-Hernandez, R. Perez-Tomas and P. A. Gale, *J. Am. Chem. Soc.*, 2011, **133**, 14136-14148.
11. N. Busschaert, L. E. Karagiannidis, M. Wenzel, C. J. E. Haynes, N. J. Wells, P. G. Young, D. Makuc, J. Plavec, K. A. Jolliffe and P. A. Gale, *Chem. Sci.*, 2014, **5**, 1118-1127.
12. X. Wu, L. W. Judd, E. N. W. Howe, A. M. Withecombe, V. Soto-Cerrato, H. Li, N. Busschaert, H. Valkenier, R. Perez-Tomas, D. N. Sheppard, Y. B. Jiang, A. P. Davis and P. A. Gale, *Chem*, 2016, **1**, 127-146.
13. T. M. Allen and L. G. Cleland, *Biochim. Biophys. Acta*, 1980, **597**, 418-426.
14. T. P. W. McMullen, R. N. A. H. Lewis and R. N. McElhaney, *Current Opinion in Colloid & Interface Science*, 2004, **8**, 459-468.
15. W. F. Bennett, J. L. MacCallum, M. J. Hinner, S. J. Marrink and D. P. Tieleman, *J. Am. Chem. Soc.*, 2009, **131**, 12714-12720.
16. N. Busschaert and P. A. Gale, *Angew. Chem. Int. Ed. Engl.*, 2013, **52**, 1374-1382.
17. P. Thordarson, *Chem. Soc. Rev.*, 2011, **40**, 1305-1323.
18. P. A. Gale, J. R. Hiscock, S. J. Moore, C. Caltagirone, M. B. Hursthouse and M. E. Light, *Chem Asian J*, 2010, **5**, 555-561.
19. M. B. Hansen, S. E. Nielsen and K. Berg, *J. Immunol. Methods*, 1989, **119**, 203-210.
20. E. Holtzman, *Lysosomes*, Plenum Press, United States, 1989.
21. A. C. Allison and M. R. Young, *Lysosomes in Biology and Pathology*, North-Holland Publishing Co., Amsterdam, 1969.
22. D. R. Green, *Cell*, 1998, **94**, 695-698.
23. A. De Milito, E. Iessi, M. Logozzi, F. Lozupone, M. Spada, M. L. Marino, C. Federici, M. Perdicchio, P. Matarrese, L. Lugini, A. Nilsson and S. Fais, *Cancer Res.*, 2007, **67**, 5408-5417.
24. M. J. Frisch, G. W. Trucks, H. B. Schlegel, G. E. Scuseria, M. A. Robb, J. R. Cheeseman, G. Scalmani, V. Barone, B. Mennucci, G. A. Petersson, H. Nakatsuji, M. Caricato, X. Li, H. P. Hratchian, A. F. Izmaylov, J. Bloino, G. Zheng, J. L. Sonnenberg, M. Hada, M. Ehara, K. Toyota, R. Fukuda, J. Hasegawa, M. Ishida, T. Nakajima, Y. Honda, O. Kitao, H. Nakai, T. Vreven, J. A. Montgomery, Jr, J. E. Peralta, F. Ogliaro, M. Bearpark, J. J. Heyd, E. Brothers, K. N. Kudin, V. N. Staroverov, R. Kobayashi, J. Normand, K. Raghavachari, A. Rendell, J. C. Burant, S. S. Iyengar, J. Tomasi, M. Cossi, N. Rega, J. M. Millam, M. Klene, J. E. Knox, J. B. Cross, V. Bakken, C. Adamo, J. Jaramillo, R. Gomperts, R. E. Stratmann, O. Yazyev, A. J. Austin, R. Cammi, C. Pomelli, J. W. Ochterski, R. L. Martin, K. Morokuma, V. G. Zakrzewski, G. A. Voth, P. Salvador, J. J. Dannenberg, S. Dapprich, A. D. Daniels, Ö. Farkas, J. B. Foresman, J. V. Ortiz, J. Cioslowski and D. J. Fox, *Gaussian 09, Revision A.02*, Gaussian, Inc., Wallingford, CT, 2009.
25. T. Lu and F. Chen, *J. Comput. Chem.*, 2012, **33**, 580-592.
26. E. D. Glendening, C. R. Landis and F. Weinhold, *J. Comput. Chem.*, 2013, **34**, 1429-1437.
27. E. D. Glendening, J. K. Badenhoop, A. E. Reed, J. E. Carpenter, J. A. Bohmann, C. M. Morales, C. R. Landis and F. Weinhold, *Journal*, 2013.
28. E. D. Glendening, C. R. Landis and F. Weinhold, *J. Comput. Chem.*, 2013, **34**, 2134-2134.
29. D. Case, J. T. Berryman, D. S. S. R. M. Betz, T. E. Cheatham, T. A. Darden, R. E. Duke, T. J. Giese, H. Gohlke, A. W. Goetz, N. Homeyer, S. Izadi, P. Janowski, J. Kaus, A. Kovalenko, T. S. Lee, S. LeGrand, P. Li, R. Luo, B. Madej, K. M. Merz, G. Monard, P. Needham, H. Nguyen, H. T. Nguyen, I. Omelyan, A. Onufriev, D. R. Roe, A. Roitberg, R. Salomon-Ferrer, C. L. Simmerling, W. Smith, J. Swails, R. C. Walker, J. Wang, R. M. Wolf, X. Wu, D. M. York and P. A. Kollman, *AMBER 14*, University of California, San Francisco, 2014.
30. J. C. Phillips, R. Braun, W. Wang, J. Gumbart, E. Tajkhorshid, E. Villa, C. Chipot, R. D. Skeel, L. Kale and K. Schulten, *J. Comput. Chem.*, 2005, **26**, 1781-1802.

31. D. A. Case, R. M. Betz, D. S. Cerutti, T. E. Cheatham, III, T. A. Darden, R. E. Duke, T. J. Giese, H. Gohlke, A. W. Goetz, N. Homeyer, S. Izadi, P. Janowski, J. Kaus, A. Kovalenko, T. S. Lee, S. LeGrand, P. Li, C. Lin, T. Luchko, R. Luo, B. Madej, D. Mermelstein, K. M. Merz, G. Monard, H. Nguyen, H. T. Nguyen, I. Omelyan, A. Onufriev, D. R. Roe, A. Roitberg, C. Sagui, C. L. Simmerling, W. M. Botello-Smith, J. Swails, R. C. Walker, J. Wang, R. M. Wolf, X. Wu, L. Xiao and P. A. Kollman, *AMBER 2016*, University of California, San Francisco, 2016.
32. A. W. Gotz, M. J. Williamson, D. Xu, D. Poole, S. Le Grand and R. C. Walker, *J. Chem. Theory Comput.*, 2012, **8**, 1542-1555.
33. R. Salomon-Ferrer, A. W. Gotz, D. Poole, S. Le Grand and R. C. Walker, *J. Chem. Theory Comput.*, 2013, **9**, 3878-3888.
34. S. Le Grand, A. W. Götz and R. C. Walker, *Comput. Phys. Commun.*, 2013, **184**, 374-380.
35. C. J. Dickson, B. D. Madej, A. A. Skjevik, R. M. Betz, K. Teigen, I. R. Gould and R. C. Walker, *J. Chem. Theory Comput.*, 2014, **10**, 865-879.
36. J. Wang, R. M. Wolf, J. W. Caldwell, P. A. Kollman and D. A. Case, *J. Comput. Chem.*, 2004, **25**, 1157-1174.
37. J. Wang, R. M. Wolf, J. W. Caldwell, P. A. Kollman and D. A. Case, *J. Comput. Chem.*, 2005, **26**, 114-114.
38. C. I. Bayly, P. Cieplak, W. D. Cornell and P. A. Kollman, *J. Phys. Chem.*, 1993, **97**, 10269-10280.
39. F. H. Allen, *Acta crystallographica. Section B, Structural science*, 2002, **58**, 380-388.
40. G. Ambrosi, M. Formica, V. Fusi, L. Giorgi, A. Guerri, M. Micheloni, P. Paoli, R. Pontellini and P. Rossi, *Chem. Eur. J.*, 2007, **13**, 702-712.
41. J. Wang, W. Wang, P. A. Kollman and D. A. Case, *J. Mol. Graph. Model.*, 2006, **25**, 247-260.
42. E. F. Pettersen, T. D. Goddard, C. C. Huang, G. S. Couch, D. M. Greenblatt, E. C. Meng and T. E. Ferrin, *J. Comput. Chem.*, 2004, **25**, 1605-1612.
43. L. Martinez, R. Andrade, E. G. Birgin and J. M. Martinez, *J. Comput. Chem.*, 2009, **30**, 2157-2164.
44. W. L. Jorgensen, J. Chandrasekhar, J. D. Madura, R. W. Impey and M. L. Klein, *J. Chem. Phys.*, 1983, **79**, 926-935.
45. P. Li, L. F. Song and K. M. Merz, Jr., *J. Chem. Theory Comput.*, 2015, **11**, 1645-1657.
46. T. Darden, D. York and L. Pedersen, *J. Chem. Phys.*, 1993, **98**, 10089-10092.
47. R. J. Loncharich, B. R. Brooks and R. W. Pastor, *Biopolymers*, 1992, **32**, 523-535.
48. H. J. C. Berendsen, J. P. M. Postma, W. F. Vangunsteren, A. Dinola and J. R. Haak, *J. Chem. Phys.*, 1984, **81**, 3684-3690.
49. J.-P. Ryckaert, G. Ciccotti and H. J. C. Berendsen, *J. Comput. Phys.*, 1977, **23**, 327-341.
50. I. Marques, A. R. Colaco, P. J. Costa, N. Busschaert, P. A. Gale and V. Felix, *Soft Matter*, 2014, **10**, 3608-3621.
51. X. Q. Jin, Q. Q. Min, Y. F. Zheng, P. C. Wang, J. Zhu and H. B. Zhou, *Arkivoc*, 2010, DOI: 10.3998/ark.5550190.0011.b25, 322-335.
52. A. P. Davis, S. M. Draper, G. Dunne and P. Ashton, *Chem. Commun.*, 1999, DOI: 10.1039/a907179b, 2265-2266.
53. R. B. Elmes, P. Turner and K. A. Jolliffe, *Org. Lett.*, 2013, **15**, 5638-5641.
54. N. Fu, A. D. Allen, S. Kobayashi, T. T. Tidwell, S. Vukovic, S. Arumugam, V. V. Popik and M. Mishima, *J. Org. Chem.*, 2007, **72**, 1951-1956.
55. C. E. Silva, H. F. Dos Santos, N. L. Speziali, R. Diniz and L. F. de Oliveira, *J. Phys. Chem. A*, 2010, **114**, 10097-10109.
56. R. S. Muthyala, G. Subramaniam and L. Todaro, *Org. Lett.*, 2004, **6**, 4663-4665.
57. R. Mattes, G. Johann and C. Pieper, *Monatshefte für Chemie Chemical Monthly*, 1987, **118**, 105-113.
58. A. Lemmerer and S. A. Bourne, *Acta crystallographica. Section E, Structure reports online*, 2012, **68**, o384.
59. A. Frontera, M. Orell, C. Garau, D. Quinonero, E. Molins, I. Mata and J. Morey, *Org. Lett.*, 2005, **7**, 1437-1440.
60. V. Amendola, G. Bergamaschi, M. Boiocchi, L. Fabbrizzi and M. Milani, *Chem. Eur. J.*, 2010, **16**, 4368-4380.
61. B. Lunelli, P. Roversi, E. Ortoleva and R. Destro, *J Chem Soc Faraday T*, 1996, **92**, 3611-3623.
62. C. Gatti, E. May, R. Destro and F. Cargnoni, *J. Phys. Chem. A*, 2002, **106**, 2707-2720.
63. C. Rotger, B. Soberats, D. Quinonero, A. Frontera, P. Ballester, J. Benet-Buchholz, P. M. Deya and A. Costa, *Eur. J. Org. Chem.*, 2008, **2008**, 1864-1868.
64. J. P. Malerich, K. Hagihara and V. H. Rawal, *J. Am. Chem. Soc.*, 2008, **130**, 14416-14417.
65. A. Rostami, A. Colin, X. Y. Li, M. G. Chudzinski, A. J. Lough and M. S. Taylor, *J. Org. Chem.*, 2010, **75**, 3983-3992.
66. T. Kolev, R. W. Seidel, H. Mayer-Figge, M. Spiteller, W. S. Sheldrick and B. B. Koleva, *Spectrochim. Acta. A Mol. Biomol. Spectrosc.*, 2009, **72**, 502-509.
67. J. S. Oh, K. I. Kim and C. E. Song, *Org Biomol Chem*, 2011, **9**, 7983-7985.
68. M. Porel, V. Ramalingam, M. E. Domaradzki, V. G. Young, V. Ramamurthy and R. S. Muthyala, *Chem. Commun.*, 2013, **49**, 1633-1635.
69. Z. Dong, G. F. Qiu, H. B. Zhou and C. N. Dong, *Tetrahedron-Asymmetr*, 2012, **23**, 1550-1556.
70. R. Prohens, A. Portell, C. Puigjaner, S. Tomas, K. Fujii, K. D. M. Harris, X. Alcobe, M. Font-Bardia and R. Barbas, *Crystal Growth & Design*, 2011, **11**, 3725-3730.
71. L. Dai, H. Yang and F. Chen, *Eur. J. Org. Chem.*, 2011, **2011**, 5071-5076.

72. N. Suleymanoglu, R. Ustabas, Y. B. Alpaslan, F. Eyduran, C. Ozyurek and N. O. Iskeleli, *Spectrochim. Acta. A Mol. Biomol. Spectrosc.*, 2011, **83**, 472-477.
73. R. Prohens, A. Portell, C. Puigjaner, R. Barbas, X. Alcobe, M. Font-Bardia and S. Tomas, *Crystengcomm*, 2012, **14**, 5745-5748.
74. A. Portell, R. Barbas, D. Braga, M. Polito, C. Puigjaner and R. Prohens, *Crystengcomm*, 2009, **11**, 52-54.
75. C. Estarellas, M. C. Rotger, M. Capo, D. Quinonero, A. Frontera, A. Costa and P. M. Deya, *Org. Lett.*, 2009, **11**, 1987-1990.